

ELECTRONIC AND MAGNETIC PROPERTIES OF QUANTUM SPIN SYSTEMS

A THESIS SUBMITTED FOR
THE DEGREE OF DOCTOR OF PHILOSOPHY (SCIENCE)
OF THE UNIVERSITY OF JADAVPUR

BADIUR RAHAMAN

S. N. Bose National Centre for Basic Sciences
Block-JD, Sector-III, Salt Lake
Kolkata-700 098, India
March 2008

CERTIFICATE FROM THE SUPERVISOR

This is to certify that the thesis entitled “**Electronic and Magnetic Properties of Quantum Spin Systems**” submitted by **Badiur Rahaman**, who got his name registered on **November 20, 2006** for the award of **Ph.D. (Science)** degree of **Jadavpur University**, is absolutely based upon his own work under the supervision of **Dr. Tanusri Saha-Dasgupta** at **S. N. Bose National Centre For Basic Sciences, Kolkata, India** and that neither this thesis nor any part of its has been submitted for any degree/diploma or any other academic award anywhere before.

Date:

Tanusri Saha-Dasgupta

Reader

S. N. Bose National Centre for Basic Sciences
Block-JD, Sector-III, Salt Lake, Kolkata - 700098, India

Acknowledgements

First, I would like to thank my supervisor, Tanusri Saha-Dasgupta, for her continuous support in the Ph.D program. She was always there to listen and to give advice. Interactions with her were always so friendly that it gave me ample opportunity to ask questions and express my ideas. She showed me the different ways to approach a research problem and always insisted on staying focused and working hard. It has really been a wonderful experience working with her.

I would like to thank my collaborators, Roser Valenti, L Andrea Salguero and Harald O Jeschke. Also I would like to thank Shasab Derakhshan.

As for other members of our group, I would like to thank Molly De Roychaudhury, Soumendu Datta, Swarup Saha, Hena Das, Swastika Chatterjee and Soumyajit Sarkar. I have always shared a brotherly relationship with them. Their vibrancy and wonderful attitude always kept me going and academic discussions with them are also acknowledged. Kartick, Mosh-iour, Tuhin, Harun, Sourav and Roby always brought with them a breath of fresh air and interacting with them was fun. They provided the much needed boost in the final year of my Ph.D and helped a lot while I was writing my thesis.

My heartiest thanks goes to my friends, seniors and juniors who made my stay at S.N. Bose Centre colorful and enjoyable. Life here would not have been the same without them. I relish the memories of the interactions that I had with them during my Ph.D program and it would be fair enough to say that their support and cooperation helped me immensely to complete my research work. I wish to thank the staff members of this centre for their sincere cooperation and help.

Last, but not the least, I thank my family for unconditional support and encouragement to pursue my interests.

List of Publications

Articles in journals/unpublished eprints:

- [1] **Badiur Rahaman**, Harald O. Jeschke, Roser Valení and T. Saha-Dasgupta, *Microscopic model for the frustrated Cu II-spin tetrahedron-based $Cu_4Te_5O_{12}X_4$ ($X=Cl, Br$) systems*, **Phys. Rev. B** **75**, 024404 (2007).
- [2] **Badiur Rahaman** and T. Saha-Dasgupta, *Electronic structure and microscopic model of $V_2GeO_4F_2$ —a quantum spin system with $S = 1$* , **J. Phys.: Condens. Matter** **19**, 296206 (2007).
- [3] Shahab Derakhshan, Heather L. Cuthbert, John E. Greedan, **Badiur Rahaman** and Tanusri Saha-Dasgupta, *Electronic structures and low-dimensional magnetic properties of the ordered rocksalt oxides $Na_3Cu_2SbO_6$ and $Na_2Cu_2TeO_6$* , **Phys. Rev. B** **76**, 104403 (2007).
- [4] L. Andrea Salguero, Harald O. Jeschke, **Badiur Rahaman**, Tanusri Saha-Dasgupta, Christian Buchsbaum, Martin U. Schmidt and Roser Valentí, *Cu-based metalorganic systems: an ab initio study of the electronic structure*, **New Journal of Physics** **9**, 26 (2007).
- [5] Harald O. Jeschke, L. Andrea Salguero, **Badiur Rahaman**, Christian Buchsbaum, Volodymyr Pashchenko, Martin U. Schmidt, Tanusri Saha-Dasgupta and Roser Valentí, *Microscopic modeling of a spin crossover transition*, **New Journal of Physics** **9**, 448 (2007).
- [6] A. Brühl, B. Wolf, V. Pashchenko, M. Anton, C. Gross, W. Assmus, R. Valenti, S. Glocke, A. Klümper, T. Saha-Dasgupta, **Badiur Rahaman** and M. Lang, *Effects of two energy scales in weakly dimerized antiferromagnetic quantum spin chains*, **Phys. Rev. Lett.** **99**, 057204 (2007).
- [7] R. Valentí, T. Saha-Dasgupta, H. O. Jeschke, **Badiur Rahaman**, H. Rosner, P. Lemmens, R. Takagi, M. Johnsson, *Comparative investigation of the coupled-tetrahedra quantum spin systems $Cu_2Te_2O_5X_2$, $X = Cl, Br$ and $Cu_4Te_5O_{12}Cl_4$* , **Physica C** **460**, 462 (2007).

-
- [8] Y. Tsui, A. Brühl, K. Removic-Langer, V. Pashchenko, B. Wolf, G. Donath, A. Pikul, T. Kretz, H.-W. Lerner, M. Wagner, A. Salguero, T. Saha-Dasgupta, **Badiur Rahaman**, R. Valentí and M. Lang, *Field-induced phase transition in a metalorganic spin-dimer system—a potential model system to study Bose-Einstein condensation of magnons*, **Journal of Magnetism and Magnetic Materials** **310**, 1319 (2007).
- [9] Bernd Wolf, Andreas Brühl, Volodymyr Pashchenko, Katharina Removic-Langer, Tonia Kretz, Jan W. Bats, H.-Wolfram Lerner, Matthias Wagner, Andrea Salguero, Tanusri Saha-Dasgupta, **Badiur Rahaman**, Roser Valentí and Michael Lang, *Modified 1,4-hydroquinone ligands bridging Cu^{II} ions—Building blocks for a new class of quantum magnets*, **C. R. Chimie** **10**, 109 (2007).
- [10] **Badiur Rahaman**, L. A. Salguero, H. O. Jeschke, T. Saha-Dasgupta and R. Valentí, *Electronic structure and magnetic properties of $K_2V_3O_8$* , (under preparation).

Abstract

The behavior of low-dimensional quantum spin systems is dominated by zero-point spin fluctuation. As a consequence, they show a variety of interesting magnetic properties which are not present in their classical counterparts. Interest in quantum spin systems has been driven by the importance for understanding the mechanism of high- T_c superconductivity and in recent years by its probable application in the field of quantum computation.

Quantum fluctuations prevent true long-range antiferromagnetic (AF) order for homogeneous 1-D spin systems. In these systems, spin-spin correlation decays slowly to zero as power law. In 2-D spin systems, the Heisenberg model has a ground state with long-range AF order. Neither system has a spin gap. The quantum fluctuation brings a dramatic effect in behavior of compounds intermediate between 1-D and 2-D, i.e., quasi 1-D spin systems. These systems may have a finite energy gap between singlet ground state ($S=0$) to triplet excited state ($S=1$) like even-leg ladder compounds. In addition 1-D alternating chain compounds, dimer compounds, spin-Peierls systems also show gap in their spin excitation spectrum.

In the field of quantum spin systems, it is an usual practice to derive the theoretical models by fitting the experimental results like susceptibility data. However, often such fitting procedure which requires solution of the assumed spin Hamiltonian leads to ambiguity in deciding the representative model. $(VO)_2P_2O_7$ forms a classic example in this regard which turned out to be an alternating chain compound while it was originally considered to be an example of ladder compound. Therefore microscopic understanding is required for the sake of uniqueness.

These compounds are often transition metal based systems like cuprates, vanadates, tellurides etc. (both inorganic and organic systems). While density functional theory (DFT) based local density approximation (LDA) calculations have been immensely successful in providing the ground state properties of many of the systems, it is not possible to describe the electronic structure and related properties of strongly correlated systems. Strong interactions preclude the possibility of any effective single-particle description. The transitional metal based quantum spin systems that we are interested in precisely falls in this category of strongly correlated electron system. Hubbard, t - J or Heisenberg models play an important role in understanding many of the interesting physics in correlated electrons. However, it must be noted that depending on parameter values they can show vastly different properties.

A model is therefore compound specific.

In this thesis, we aim on deriving model Hamiltonians out of full LDA-DFT calculations considering a variety of systems belonging to the category of low-dimensional quantum spin systems.

Contents

Acknowledgements	v
List of Publications	vii
Abstract	ix
1 Introduction	5
1.1 Background	5
1.2 Different classes of low-dimensional QSS	6
1.2.1 Dimer Compounds:	6
1.2.2 Alternating Chain Compounds:	8
1.2.3 Ladder Compounds:	9
1.2.4 Spin-Peierls Systems:	12
1.3 Motivation of the present work	13
References	17
2 Methodology	21
2.1 Density functional theory and local density approximation	21
2.2 Basis sets	24
2.2.1 Linear Muffin-Tin Orbital (LMTO) method:	24
2.2.2 NMTO method:	27
References	31
3 Microscopic model for the frustrated <i>Cu II</i>-spin tetrahedron-based $Cu_4Te_5O_{12}X_4$ ($X = Cl, Br$) systems*	33
3.1 Introduction	33
3.2 Structure	35
3.3 Bandstructure	36
3.4 Downfolding and effective model	38
3.5 Interaction pathways	40

3.6	<i>Br</i> System	43
3.7	Summary	46
References		49
4	Electronic structure and microscopic model of $V_2GeO_4F_2$—a quantum spin system with $S = 1^*$	51
4.1	Introduction	51
4.2	Crystal structure	51
4.3	LDA Electronic structure	52
4.4	NMTO-downfolding and the hopping interactions	55
4.5	Magnetic exchange interactions and the microscopic model	58
4.6	Conclusion	59
References		61
5	Electronic structures and low-dimensional magnetic properties of the ordered rocksalt oxides $Na_3Cu_2SbO_6$ and $Na_2Cu_2TeO_6^*$	63
5.1	Introduction	63
5.2	Structural comparisons	65
5.3	Results	66
5.3.1	Tight-binding, magnetic dimer model:	66
5.3.2	Local density approximation calculation:	67
5.3.3	Magnetic susceptibility:	72
5.4	Summary and Conclusions	73
References		75
6	<i>Cu</i>-based metalorganic systems: an <i>ab initio</i> study of the electronic structure*	77
6.1	Introduction	77
6.2	Method	79
6.2.1	Determination of crystal structure:	79
6.2.2	Electronic structure calculations:	80
6.3	Results	81
6.3.1	Crystal structure:	81
6.3.2	Electronic structure and effective Cu–Cu interactions:	84
6.4	Summary	91
6.5	Appendix	94
References		97

7	Microscopic modeling of a spin crossover transition*	99
7.1	Introduction	99
7.2	Crystal structure	100
7.3	Energy scales	103
7.4	Electronic structure	105
7.5	Exchange interaction and magnetic properties	107
7.6	Discussion	110
	References	113

1 Introduction

1.1 Background

The low-dimensional quantum spin systems (QSS) are structurally three dimensional. However due to the anisotropy in the interaction between magnetic ions, the interaction in particular direction is very strong compared to the other directions. Effectively these spin systems form a chain or layer structure. Therefore according to interaction these systems may be effectively one dimensional (1-D) or two dimensional (2-D) or in between one and two i.e., quasi one dimensional. Considering antiferromagnetic Heisenberg model, strict antiferromagnetic alignment gains energy only from the Ising (or z-z) part of the Heisenberg interaction (the energy value is $-JS^2$, where J is the coupling strength and S is the spin). In order to get the true ground state, one needs to let the spin z-components fluctuate so that the system can gain energy also from spin flip (or x-y) terms (the extra energy lowering is $-JS$). In contrast to the ferromagnetic ground state, the ground state of the antiferromagnetic Heisenberg model shows quantum fluctuations. This can be measured by the ratio of the quantum correction to the (classical) z-z energy: $(-JS)/(-JS^2)=1/S$. For two-site case, quantum effects are of the order $\sim 1/S$. Going over to the lattice case, it can be concluded that the relevant parameter is more like $1/(zS)$, where z is the coordination number. Therefore quantum fluctuations are expected to be stronger for small spin and low dimensional systems. As a result the behavior of low-dimensional QSS is dominated by zero-point spin fluctuations. This gives rise to variety of interesting magnetic properties which are not present in their classical counterparts.

The interest in QSS has been driven by the importance for understanding the mechanism of high- T_C superconductivity as well as for their potential applications in the field of quantum computers. Synthesis of materials appropriate to various class within these systems has made this field very attractive and site of many activities. It has been suggested that spin ladders may exhibit superconductivity under doping [1]. Alternating Heisenberg antiferromagnetic chains may exhibit a novel bound two magnon mode [2]. The wide variety of behavior arises from very simple conceptual pictures, but is often driven by the quantum nature of the interaction. In recent years, a great amount of effort, both theoretically and experimentally, has been dedicated to the study of these quantum spin systems.

Bethe [3] showed that the quantum fluctuations prevent true long-range antiferromagnetic (AFM) order for homogeneous 1-D spin systems. In these systems the spin-spin correlation as a function of distance decays slowly to zero as power law. For 2-D spin systems, the Heisenberg model has a ground state with long-range AFM order only at $T=0$ K. Neither system has a spin gap, i.e., there is no cost in energy to create an excitation with $S=1$. The quantum fluctuation brings a dramatic effect in behavior of compounds intermediate between 1-D and 2-D, i.e., quasi 1-D spin systems. These systems may have a finite energy gap between singlet ground state ($S=0$) and triplet excited state ($S=1$). The even-leg ladders [1], alternating Heisenberg antiferromagnetic chains [4], dimer systems [5], spin-Peierls systems [6] show gap in their spin excitation spectrum. Haldane [4] conjectured that a simple one dimensional magnetic chain would have a spin gap for all integer spins, but would be gapless for half-integer spins, a conjecture that has been backed up with considerable experimental evidence [7]. An analogous situation has been found to exist in the quasi-one dimensional spin ladder configuration, in which ladders with an even number of legs would exhibit an energy gap, but ladders with an odd number of legs would not [8].

1.2 Different classes of low-dimensional QSS

In the following we give example of different class of low dimensional QSS:

1.2.1 Dimer Compounds:

The dimer system is one in which only two sites are magnetically coupled, and are magnetically isolated from rest of the sites. More complex systems can often be built up starting with dimers, especially if the inter-dimer coupling is weak compared to the intra-dimer coupling. A schematic diagram of spin dimer system is shown in Figure 1.1.

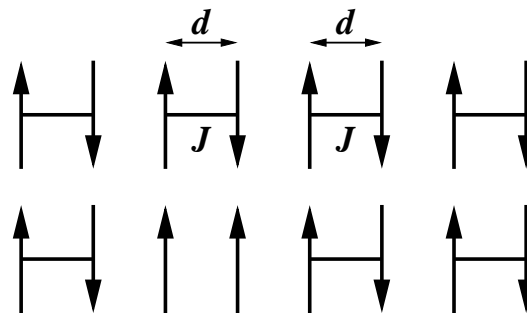


FIGURE 1.1: A dimer system consists of two spins of equal magnitude but opposite direction separated by a distance d . The interaction strength is J .

The Heisenberg Hamiltonian corresponding to antiferromagnetically coupled isotropic dimer is given by

$$H = J(\vec{S}_1 \cdot \vec{S}_2) \quad (1.1)$$

where $J > 0$ is the coupling strength and \vec{S}_1 and \vec{S}_2 are the spins of the two coupled ions. With $J > 0$, the system has minimum energy when \vec{S}_1 and \vec{S}_2 are aligned in opposite directions.

On the other hand the Hamiltonian corresponding to anisotropic dimer can be represented by

$$H = J[S_1^z S_2^z + \frac{\alpha}{2}(S_1^+ S_2^- + S_1^- S_2^+)] \quad (1.2)$$

Here, again, $J > 0$ is the coupling strength, and \vec{S}_1 and \vec{S}_2 are the spins. S^z is the z component of the spin, and S^+ and S^- are the spin raising and lowering operators respectively. α is the spin anisotropy, where $\alpha=1$ is identical with the isotropic case presented in equation (1.1).

A quantum phase transition from a gapless critical state into a gaped state (disorder spin liquid) is induced by dimerization [2]. With dimerization the spinons are confined into massive triplet excitations. An excitation of strong dimerization corresponds to the breaking of one dimer (see lower panel of Figure 1.1). The energy related to this process is the singlet-triplet gap.

An example of the dimer system can be $\text{CaCuGe}_2\text{O}_6$. Susceptibility measurements on $\text{CaCuGe}_2\text{O}_6$ show the existence of a spin-singlet ground state with finite energy gap [5]. The spin gap in $\text{CaCuGe}_2\text{O}_6$ is intrinsic. Inelastic neutron scattering (INS) measurements were carried out on $\text{CaCuGe}_2\text{O}_6$ powder and the existence of a finite spin gap was confirmed [9]. The structure of this material shows an obvious zigzag one-dimensional chain of spin-1/2 Cu^{+2} ions along c axis. Nevertheless, the magnetization and susceptibility data of Sasago *et al.* [5] are in disagreement with a spin-1/2 Heisenberg chain model. The analysis of the electronic structure of $\text{CaCuGe}_2\text{O}_6$ by first-principle calculations as well as the examination of susceptibility and magnetization data by the Quantum Monte Carlo (QMC) method leads to a unique description of this material as a system of dimers formed by third-nearest-neighbor copper pairs [10].

Another example of spin dimer system with metal ions and organic ligands may be vanadyl glycolate. The solvothermal reaction, at 200 °C, of vanadium pentoxide and lithium hydroxide in acetic acid or ethylene glycol leads to the formation of vanadyl acetate and vanadyl glycolate respectively. The structure of the acetate contains vanadium in octahedral coordination whereas the glycolate contains VO_5 square pyramids. The VO_6 octahedra in the acetate, $\text{VO}(\text{CH}_3\text{COO})_2$, are joined through the vanadyl groups, giving a rather $\text{V}=\text{O}$ bond of 1.684(7) Å and a *trans* $\text{V}-\text{O}$ bond of 2.131(7) Å, and by bridging acetate groups. The vanadium atoms interact along the $\dots\text{V}=\text{O}\dots\text{V}=\text{O}\dots$ chain giving one-dimensional

antiferromagnetic behavior. In contrast in the glycolate, the apical V=O bond is shorter, 1.58(1) Å, and the square pyramids share edges in a two up two down fashion to give chains of formula VO(OCH₂CH₂O). Magnetic susceptibility of vanadyl glycolate is consistent with an isolated spin dimers model [11].

1.2.2 Alternating Chain Compounds:

The alternating chain is an infinite chain of dimers connected together, but the connection between the dimers is not the same as the connection within the dimer. The intra-dimer exchange and inter-dimer exchange constants, J_1 and $J_2 < J_1$ alternate from bond to bond along the chain. A schematic representation of an alternating Heisenberg antiferromagnetic chain is shown in Figure 1.2. The system is represented by the Hamiltonian

$$H = \sum_i [J_1 \vec{S}_1(i) \cdot \vec{S}_2(i) + J_2 \vec{S}_2(i) \cdot \vec{S}_1(i+1)] \quad (1.3)$$

where i is the position of a dimer. $J_1, J_2 > 0$ for AFM coupling.

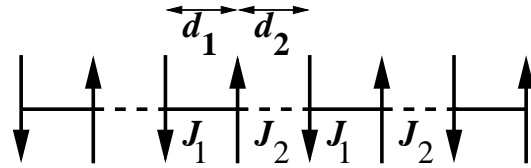


FIGURE 1.2: An alternating chain consists of pairs of spins separated by distance d_1 and interacting with strength J_1 , which are coupled with an identical pair a distance d_2 away with a strength J_2 .

If $J_1=J_2$, the system can be considered as a uniform AFM Heisenberg chain, the ground state of which has been solved exactly. While the uniform Heisenberg chain has no spin gap, the alternating chain compound on the other hand shows spin gap [2, 12], the magnitude of which depends on J_2/J_1 . If $J_2=0$, the system is equivalent to the magnetic dimer.

The Hamiltonian in equation (1.3) describes the case of isotropic alternating chain. The Hamiltonian corresponding to anisotropic alternating chain is represented by

$$H = \sum_i \left(J_1 [S_1^z(i)S_2^z(i) + \frac{\alpha_1}{2} \{S_1^+(i)S_2^-(i) + S_1^-(i)S_2^+(i)\}] \right. \\ \left. + J_2 [S_2^z(i)S_1^z(i+1) + \frac{\alpha_2}{2} \{S_2^+(i)S_1^-(i+1) + S_2^-(i)S_1^+(i+1)\}] \right) \quad (1.4)$$

where α_1 and α_2 being the spin anisotropy. Neither the anisotropic chain nor the isotropic chain has been solved exactly, although a variety of approximation methods have been applied to them.

A good example of alternating spin chain system is that of vanadyl pyrophosphate, $(VO)_2P_2O_7$ [13, 14]. In $(VO)_2P_2O_7$, the edge-sharing pairs of VO_6 octahedra are stacked along the a axis to form a two-leg structural ladder. The ladders are linked by covalently bonded PO_4 tetrahedra to form a three dimensional network with corner-sharing VO_6 octahedra. INS investigation of the magnetic excitation [15–17] as well as several studies of spin-phonon coupling [18–21] have been carried out, giving rise to well understood knowledge of the spin Hamiltonian and low energy dynamics of this material. $(VO)_2P_2O_7$ is now known to be alternating chain compound. The alternating magnetic chains form along the b axis, with V–O–V and V–O–P–O–V superexchange interactions. The strongest exchange path is found to be that between two V^{+4} ions through two phosphate groups PO_4 and not between nearest-neighbor vanadium ions V–O–V as was initially thought. Substantial “beyond Heisenberg” interactions have also been observed, including spin singlet to triplet gap activated via magnetoelastic coupling in the $(VO)_2P_2O_7$ system.

An example of $S = 1/2$ alternating linear Heisenberg organic antiferromagnet is pentafluorophenyl nitroxide (F_5PNN) [22]. The alternating linear Heisenberg antiferromagnet has two antiferromagnetic interactions lying alternately in one dimension, and shows the excitation gap at very low temperatures.

1.2.3 Ladder Compounds:

Both the magnetic systems, dimers and alternating chains, discussed above are one dimensional, while a ladder system is intermediate between a one and two dimensional system, called quasi 1-D system. To make the transition from the quasi long range order in a chain of antiferromagnetically coupled $S=1/2$ spin to the true long range order that occurs in a plane, one can assemble chains to make ladders of increasing width. Therefore a ladder consists of two or more spin chains coupled together across “rung”. This additional coupling changes the character of the interaction from one dimensional to two dimensional. The Hamiltonian for general spin ladder is given by

$$H = J_{\parallel} \sum_{\parallel} \vec{S}_i \cdot \vec{S}_j + J_{\perp} \sum_{\perp} \vec{S}_i \cdot \vec{S}_j \quad (1.5)$$

where J_{\parallel} is the exchange coupling along the direction of the spin chain (i.e., along the leg of the ladder), and J_{\perp} is the exchange coupling between the chains (i.e., along the rung of the ladder).

The corresponding anisotropic spin ladder system can be represented by the Hamiltonian

$$\begin{aligned}
 H = \sum_i & \left(J_{\perp} [S_1^z(i)S_2^z(i) + \frac{\alpha_{\perp}}{2} \{S_1^+(i)S_2^-(i) + S_1^-(i)S_2^+(i)\}] \right. \\
 & + J_{\parallel} [S_1^z(i)S_1^z(i+1) + \frac{\alpha_{\parallel}}{2} \{S_1^+(i)S_1^-(i+1) + S_1^-(i)S_1^+(i+1)\}] \\
 & \left. + J_{\parallel} [S_2^z(i)S_2^z(i+1) + \frac{\alpha_{\parallel}}{2} \{S_2^+(i)S_2^-(i+1) + S_2^-(i)S_2^+(i+1)\}] \right) \quad (1.6)
 \end{aligned}$$

where spins 1 and 2 form a “rung” of the ladder, and the position i is summed along the “length” of the ladder. The rungs and the legs of the ladder have different spin anisotropy, α_{\perp} and α_{\parallel} .

Schematic diagrams of 2- and 3-leg ladders are shown in Figure 1.3. Ladders made from an even number of legs have spin liquid ground states, so called because of their purely short-range spin correlation. An exponential decay of the spin-spin correlation is observed characterized by a finite spin gap, namely, a finite energy gap to the lowest $S=1$ excitation. A ladder with an odd number of legs on the other hand behaves quite differently and displays properties similar to those of single chains at low energies, namely, gap less spin excitations and a power-low falloff of the spin-spin correlations [23, 24].

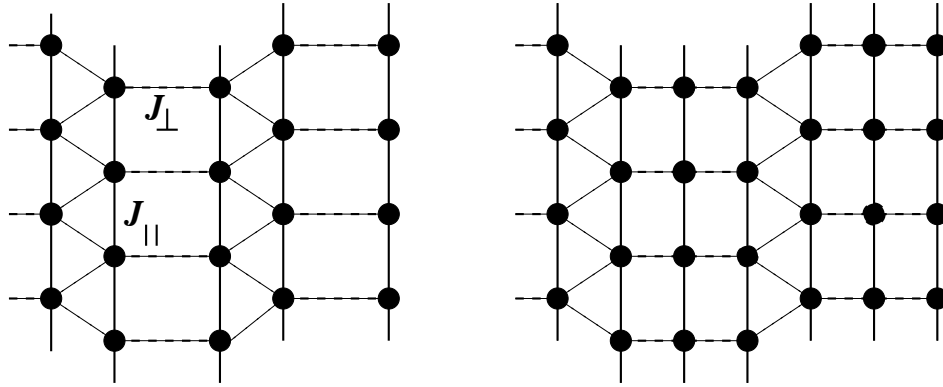


FIGURE 1.3: 2-leg and 3-leg ladder

Dagotto *et al.* [25] assumed the ideal case where the exchange coupling along the rungs of a 2-leg ladder is much larger than the coupling along the legs of the ladder. This idealization has the advantage that rungs interact only weakly with each other, and the dominant configuration in the ground state is the product state with the spins on each rung forming a spin singlet. The ground state has a total spin $S=0$ because each rung is in a spin singlet

$$|\psi_s\rangle = (|\uparrow\downarrow\rangle - |\downarrow\uparrow\rangle)/\sqrt{2} \quad (1.7)$$

To produce a S=1 excitation, a rung singlet must be promoted to a S=1 triplet

$$|\psi_t\rangle = \left[|\uparrow\uparrow\rangle, \quad (|\uparrow\downarrow\rangle + |\downarrow\uparrow\rangle)/\sqrt{2}, \quad |\downarrow\downarrow\rangle \right] \quad (1.8)$$

An isolated rung-triplet has an energy J_\perp above the rung singlet. The coupling along the chains creates a band of S=1 magnons with a dispersion, $w(k) = J_\perp + J_\parallel(\cos k)$ in the limit $J_\perp \gg J_\parallel$, where k is the wave vector. The spin gap is the minimum excitation energy $\Delta_{spin} = w(\pi) \approx J_\perp - J_\parallel$, which remains large in this limit [26]. Concurrently, the spins are mostly uncorrelated between rungs because the spin correlations decay exponentially with distance along the chains, leading to the spin liquid nature of this state.

In the other extreme, $J_\perp/J_\parallel = 0$, the two chains decouple, but isolated spin-1/2 Heisenberg chains do not have a spin gap and excitations with S=1 and $k = \pi$ are degenerate with the ground state in the bulk limit. To reconcile the different behavior in the limits $J_\perp/J_\parallel \gg 1$ and $J_\perp/J_\parallel = 0$, it was conjecture [25] that the spin gap should smoothly decrease as J_\perp/J_\parallel is reduced, reaching $\Delta_{spin} = 0$ at some critical value of the coupling. Later, Barnes *et al.* [26] observed that the power-law decay of the spin correlation in an isolated chain implies that a chain is in a critical state and thus small perturbations can qualitatively alter its properties. They predicted that the spin gap would vanish only at $J_\perp/J_\parallel = 0$, so that $\Delta_{spin} > 0$ at all $J_\perp/J_\parallel > 0$, including the values of experimental interest, $J_\perp/J_\parallel \sim 1$. The ladder spin systems therefore are always in spin-liquid states, in contrast to the more familiar cases of the 1-D and 2-D Heisenberg models, which are gapless.

Physical realizations of ladders like SrCu_2O_3 correspond to $J_\perp \approx J_\parallel$. However, at $J_\perp = J_\parallel$ there is no small parameter to guide a perturbative calculation, nor is an exact solution known. Numerical techniques can handle the region $J_\perp \approx J_\parallel$, and exact diagonalization of small clusters and results of QMC has been used [25, 26] to study Δ_{spin} as a function of J_\perp/J_\parallel . Numerical calculation of Δ_{spin} [26] shows that indeed $\Delta_{spin} > 0$ for all $J_\perp/J_\parallel \neq 0$. At the realistic coupling $J_\perp = J_\parallel$, the spin gap is $\Delta_{spin} \approx 0.5J_\parallel$. For even-leg ladders in which the ratio of the rung to leg exchange constants is $J_\perp/J_\parallel \leq 1$, the spin gap decreases exponentially with increasing number of legs [27]. A reduction in the size of the gap is natural because as the width of the ladder grows, the limit for the 2-D square lattice is approached and $\Delta_{spin} \rightarrow 0$. The spin gap on the other hand remains zero with increasing the number of legs for odd-leg ladder.

The first experimentally realized series of even- and odd-leg ladder structures was provided by the cuprates $\text{Sr}_{n-1}\text{Cu}_{n+1}\text{O}_{2n}$ ($n=3,5,\dots$) [23, 28]. SrCu_2O_3 ($n=3$) is a two-leg ladder. Measurement of spin susceptibility [1] shows that it vanishes exponentially at low temperature, which is a clear sign of spin gap. Neutron scattering and muon spin resonance measurements are consistent with short range spin order in the two-leg ladders, although

they are unfrustrated spin systems that classically should order without a spin gap. Further nuclear magnetic resonance (NMR) experiments have confirmed the large spin gap in the excitation spectrum. Three-leg ladders ($n=5$ or $\text{Sr}_2\text{Cu}_3\text{O}_5$) by contrast show longer range spin correlations. There is excellent agreement between theory and experiment, confirming that there is a dramatic difference between even- and odd-leg $S=1/2$ Heisenberg AFM ladders.

The family of potential spin-ladder compounds was recently enriched with the synthesis of the organic charge-transfer salt, $[(\text{DT-TTF})_2][\text{Au}(\text{mnt})_2]$ (DT-TTF=dithio phenetetrathiafulvalene, mnt=malonitrile dithiolate). At room temperature, the DT-TTF and $\text{Au}(\text{mnt})_2$ molecules form regular stacks of donor DT-TTF and acceptor $\text{Au}(\text{mnt})_2$ units along the monoclinic crystallographic b axis. The DT-TTF stacks are arranged in pairs related by a twofold screw axis and are isolated from each other by the $\text{Au}(\text{mnt})_2$ stacks. Pairs of organic donor molecules are strongly linked by three interstack $\text{S} \cdots \text{S}$ close contacts, resulting in a structural two-leg ladder. Below 220 K, the DT-TTF stacks are dimerized giving rise to the two-leg spin ladder in which the $[(\text{DT-TTF})_2^+]$ dimers are the spin carrying units. The temperature dependence of the susceptibility was interpreted as providing clear evidence that $[(\text{DT-TTF})_2][\text{Au}(\text{mnt})_2]$ is the first purely organic system with a two-leg spin-ladder configuration [29].

1.2.4 Spin-Peierls Systems:

The spin-Peierls transition is an intrinsic lattice instability in spin-1/2 antiferromagnetic Heisenberg chains; the driving force is the magnetoelastic coupling between the one-dimensional spin structure and the three-dimensional lattice vibrations [30]. Above the transition temperature T_{sp} , there is a uniform antiferromagnetic next-neighbor exchange in each chain; below T_{sp} there is an elastic distortion resulting in dimerization, and hence two, unequal alternating exchange constants. The dimerization increases progressively as the temperature is lowered and reaches a maximum at zero temperature. The alternating chain possesses an energy gap between the singlet ground state and the lowest lying band of triplet excited states. The magnitude of the gap is related to the degree of dimerization and hence to the degree of lattice distortion, becoming zero for the uniform chain (zero dimerization). Thus the magnetic susceptibility $\chi(T)$ shows a knee at T_{sp} , with a rather abrupt fall of χ below T_{sp} , corresponding to the opening of the gap. Whereas the normal Peierls distortion (the electronic analogue of the spin-Peierls transition) occurs at a temperature T_p of the order of $k_B T_p \sim E_F \exp(-1/\lambda)$, where λ is the electron-phonon coupling constant, the spin-Peierls transition will occur at $k_B T_{sp} \sim |J| \exp(-1/\lambda)$, where J is the exchange interaction between adjacent spins; since $J \ll E_F$ (e.g. J is typically 50 K, E_F is typically 500–5000 K), T_{sp} is always small in comparison with T_p .

There are only very few materials which show a spin-Peierls transition. This is because antiferromagnetic chains usually form three-dimensional order at low temperature due to inter-chain coupling. Only in very few materials is the spin-phonon coupling able to dominate the inter-chain spin-spin coupling and allow the formation of a spin-Peierls ground state. Examples of such materials are mainly organic systems, e.g. MEM(TCNQ)₂ ($T_{sp}=18$ K) [31], TTF-CuS₄C₄(CF₃)₄ ($T_{sp}=12$ K) [32], TTF-AuS₄C₄(CF₃)₄ ($T_{sp}=2$ K) [32, 33]. This is because such materials contain flat organic molecules in columnar stacks. The large inter-chain separation and weak van der Waals intermolecular interactions favor the dominance of magnetoelastic effects over inter-chain ordering. In contrast the chains in corresponding inorganic materials, such as copper chain compounds, are quite rigid due to the ionic bonding and only a single example of an inorganic spin-Peierls material is known (CuGeO₃, with $T_{sp}=14$ K [34]).

1.3 Motivation of the present work

A very important aspect in the study of low-dimensional QSS is the knowledge of the spin model, given a specific compound. A microscopic investigation for this purpose is essential, since often the nature of the underlying exchange network is not what is expected from crystal structure—one needs to take into account the chemistry aspect. Microscopic investigation also provides quantitative numbers corresponding to various exchange interactions. Another possible route often used, is to fit the measured susceptibility data with some assumed theoretical model. This method suffers from the drawback that the susceptibility data is quite insensitive to the details and two different models may be fitted to same data with two different sets of fitting parameters. (VO)₂P₂O₇ forms a classic example in this regard which turned out to be an alternating chain compound while it was originally considered to be an example of ladder compound [35]. Therefore microscopic understanding is required for the sake of uniqueness. In the following, we sketch the framework which we will follow for the microscopic investigation.

From a microscopic point of view, theoretical solid state physics is concerned with the investigation of interacting many particle systems involving both electrons and ions. However, it is an established fact that many of the properties of matter are well described by the purely electronic Hamiltonian of the form

$$\begin{aligned} \hat{H} &= \sum_{\sigma} \int d^3r \hat{\Psi}^{\dagger}(\mathbf{r}, \sigma) \left[-\frac{\hbar^2}{2m_e} \nabla^2 + V_{ion}(\mathbf{r}) \right] \hat{\Psi}(\mathbf{r}, \sigma) \\ &+ \frac{1}{2} \sum_{\sigma, \sigma'} \int d^3r d^3r' \hat{\Psi}^{\dagger}(\mathbf{r}, \sigma) \hat{\Psi}^{\dagger}(\mathbf{r}', \sigma') V_{ee}(\mathbf{r} - \mathbf{r}') \hat{\Psi}(\mathbf{r}', \sigma') \hat{\Psi}(\mathbf{r}, \sigma), \end{aligned} \quad (1.9)$$

where the crystal lattice enters only through an ionic potential. The applicability of this

approach may be justified by the validity of the Born and Oppenheimer approximation [36]. Here, $\hat{\Psi}^\dagger(\mathbf{r}, \sigma)$ and $\hat{\Psi}(\mathbf{r}, \sigma)$ are field operators that create and annihilate an electron at position \mathbf{r} with spin σ , m_e the electron mass, e the electron charge, and

$$V_{ion}(\mathbf{r}) = -e^2 \sum_i \frac{Z_i}{|\mathbf{r} - \mathbf{R}_i|} \quad (1.10)$$

and

$$V_{ee}(\mathbf{r} - \mathbf{r}') = \frac{e^2}{2} \sum_{\mathbf{r} \neq \mathbf{r}'} \frac{1}{|\mathbf{r} - \mathbf{r}'|} \quad (1.11)$$

denote the one particle potential due to all ions i with charge eZ_i at given positions \mathbf{R}_i , and the electron-electron interaction, respectively.

While the *ab initio* Hamiltonian (1.9) is easy to write down, it is impossible to solve exactly if more than a few electrons are involved. Numerical methods like Green's Function Monte Carlo and related approaches have been used successfully for relatively modest numbers of electrons. Because of this, one generally either needs to make substantial approximations to deal with the Hamiltonian (1.9) as is done in local density approximation of density functional theory (LDA-DFT), or replace it by a greatly simplified many-body model Hamiltonian. At present these two different strategies for the investigation of the electronic properties of solids are applied by two largely separate groups of people: the density functional theory community and the many-body community.

DFT-based LDA calculations have been immensely successful in providing the ground state properties of many of the systems [37]. However, it is not possible to describe the electronic structure and related properties of strongly correlated systems like d - and f -electron systems which have a Coulomb interaction comparable to band width within the DFT-LDA framework. Application of DFT-LDA in describing ground state properties of such materials is seriously restricted in its accuracy and reliability. This is because the strong interactions preclude the possibility of any effective single-particle description. The transitional metal based quantum spin systems that we are interested in precisely falls in this category of strongly correlated electron system. On the other hand, although the models play an important role in understanding many of the interesting physics in correlated electrons; it must be noted that depending on parameter values they can show vastly different properties. All the anomalous properties of these correlated compounds are highly sensitive to small changes in temperature, pressure and doping, there by proving an intricate interplay between material specific chemistry and the correlation effect. The material-specific aspect and the correlation effect therefore need to be dealt on equal footing. DFT-LDA approach though fails in capturing the correlation aspect, correctly incorporates the material-specific details. It is therefore highly desirable to combine the many-body model

Hamiltonian approach with that of DFT-LDA approach in terms of defining material-specific model Hamiltonians out of DFT-LDA calculations.

The work presented in this thesis focuses on modeling of a system of complex materials, which fall in the category of quantum spin systems, starting from DFT-LDA electronic structure of the compounds. Such microscopically derived many-body model Hamiltonian which is the spin Hamiltonian of the systems can be used as inputs to the next level of calculation in terms of solution of the first principles derived model Hamiltonian by many-body techniques like Quantum Monte Carlo (QMC) or Exact diagonalization to derive the physical properties of the systems.

In this thesis application has been made to systems where magnetic ions are linked by inorganic ligands as well as materials having magnetic ions linked by organic ligands, the so-called hybrid materials. While sections 3, 4 and 5 deal with materials with inorganic linkers, sections 6 and 7 are devoted to materials with organic ligands. In section 2 we briefly describe the DFT-LDA framework which has been employed for the study of these materials.

References

- [1] E. Dagotto and T. M. Rice, *Science* **271**, 618 (1996).
- [2] G. S. Uhrig and H. J. Schulz, *Phys. Rev. B* **54**, R9624 (1996).
- [3] H. Bethe, *Z. Phys.* **71**, 205 (1931).
- [4] F. D. M. Haldane, *Phys. Rev. Lett.* **50**, 1153 (1983).
- [5] Y. Sasago, M. Hase, K. Uchinokura, M. Tokunaga and N. Miura, *Phys. Rev. B* **52**, 3533 (1995).
- [6] M. Nishi, O. Fujita and J. Akimitsu, *Phys. Rev. B* **50**, 6508 (1994).
- [7] R. M. Morra, W. J. L. Buyers, R. L. Armstrong and K. Hirakawa, *Phys. Rev. B* **38**, 543 (1988).
- [8] M. Azuma, Z. Hiroi, M. Takano, K. Ishida and Y. Kitaoka, *Phys. Rev. Lett.* **73**, 3463 (1994).
- [9] A. Zheludev, G. Shirane, Y. Sasago, M. Hase and K. Uchinokura, *Phys. Rev. B* **53**, 11642 (1996).
- [10] R. Valenti, T. Saha-Dasgupta and C. Gross, *Phys. Rev. B* **66**, 054426 (2002).
- [11] C. Weeks, Y. Song, M. Suzuki, N. A. Chernova, P. Y. Zavalij and M. S. Whittingham, *J. Mater. Chem.* **13**, 1420 (2003).
- [12] A. Auerbach, *Interacting Electrons and Quantum Magnetism* (Springer, Graduate Texts in Contemporary Physics, New York) (1994).
- [13] C. C. Torardi and J. C. Calabrese, *Inorg. Chem.* **23**, 1308 (1984).
- [14] C. C. Torardi, Z. G. Li, H. S. Horowitz, W. Liang and W. H. Whangbo, *J. Solid State Chem.* **119**, 349 (1995).
- [15] D. A. Tennant, S. E. Nagler, A. W. Garrett, T. Barnes and C. C. Torardi, *Phys. Rev. Lett.* **78**, 4998 (1997).

-
- [16] A. W. Garrett, S. E. Nagler, T. Barnes and B. C. Sales, *Phys. Rev. B* **55**, 3631 (1997).
- [17] A. W. Garrett, S. E. Nagler, D. A. Tannant, B. C. Sales and T. Barnes, *Phys. Rev. Lett.* **79**, 745 (1997).
- [18] J. Cao, J. T. Haraldsen, S. Brown, J. L. Musfeldt, J. R. Thompson, S. Zvyagin, J. Krzystek, M. -H. Whangbo, S. E. Nagler and C. C. Torardi, *Phys. Rev. B* **72**, 214421 (2005).
- [19] L. M. L. Daku, S. Borshch, V. Robert and B. Bigot, *Phys. Rev. B* **63**, 174439 (2001).
- [20] G. S. Uhrig and B. Normand, *Phys. Rev. B* **63**, 134418 (2001).
- [21] U. Kuhlmann, C. Thomsen, A. V. Prokofiev, F. Büllfeld, E. Uhrig, M. Anton, C. Gross and W. Assmus, *Phys. Rev. B* **66**, 064420 (2002).
- [22] Y. Yoshida, K. Yurue, M. Mitoh, T. Kawae, Y. Hosokoshi, K. Inoue, M. Kinoshita and K. Takeda, *Physica B: Condensed Matter* **329-333**, 979 (2003).
- [23] T. M. Rice, S. Gopalan and M. Sigrist, *Europhys. Lett.* **23**, 445 (1993).
- [24] S. Gopalan, T. M. Rice and M. Sigrist, *Phys. Rev. B* **49**, 8901 (1994).
- [25] E. Dagotto, J. Riera and D. J. Scalapino, *Phys. Rev. B* **45**, 5744 (1992);
E. Dagotto and A. Moreo, *Phys. Rev. B* **38**, 5087 (1988).
- [26] T. Bernes, E. Dagotto, J. Riera and E. S. Swanson, *Phys. Rev. B* **47**, 3196 (1993).
- [27] D. Poilblanc, H. Tsunetsung and T. M. Rice, *Phys. Rev. B* **50**, 6511 (1994).
- [28] Z. Hiroi, M. Azuma, M. Takano and Y. Bando, *J. Solid State Chem.* **95**, 230 (1991).
- [29] C. Rovira, J. Veciana, E. Ribera, J. Tarres, E. Candell, R. Rousseau, M. Mas, E. Molins, M. Almeida, R. T. Henriques, J. Morgado, J. -P. Schoeffel and J. -P. Pouget, *Angew. Chem. Int. Ed. Engl.* **36**, 2324 (1997); *Chem. Eur. J.* **5**, 2025 (1999).
- [30] J. W. Bray, L. V. Interrante, I. S. Jacobs, and J. C. Bonner, *Extended Linear Chain Compounds* **3**, 353 (New York: Plenum) (1983).
- [31] S. Huizinga, J. Kommandeur, G. A. Sawatzky, B. T. Thole, K. Kopinga, W. J. M. de Jonge, and J. Roos, *Phys. Rev. B* **19**, 4723 (1979).
- [32] J. W. Bray, H. R. Hart, L. V. Interrante, I. S. Jacobs, J. S. Kasper, G. D. Watkins, S. H. Wee and J. C. Bonner, *Phys. Rev. Lett.* **35**, 744 (1975).

-
- [33] I. S. Jacobs, J. W. Bray, H. R. Hart, L. V. Interrante, J. S. Kasper, G. D. Watkins, D. E. Prober and J. C. Bonner, *Phys. Rev. B* **14**, 3036 (1976).
- [34] M. Hase, I. Terasaki and K. Uchinokura, *Phys. Rev. Lett.* **70**, 3651 (1993).
- [35] D. C. Johnston *et al.*, *Phys. Rev. B* **61**, 9558 (2000).
- [36] M. Born and J. R. Oppenheimer, *Ann. Phys. (Leipzig)* **84**, 457 (1927).
- [37] R. O. Jones and O. Gunnarsson, *Rev. Mod. Phys.* **61**, 689 (1989).

2 Methodology

2.1 Density functional theory and local density approximation

The fundamental theorem of DFT by Hohenberg and Kohn [1] states that the ground state energy is a functional of the electron density which assumes its minimum at the ground state electron density. Following Lavy's constrained search approach [2] is easily proved and functional can even be constructed by taking the minimum (infimum) of the energy expectation value w.r.t all (many-body) wave functions $\varphi(\mathbf{r}_1\sigma_1, \dots, \mathbf{r}_N\sigma_N)$ at a given electron number N which yield electron density $\rho(\mathbf{r})$:

$$E[\rho] = \inf \left\{ \langle \varphi | \hat{H} | \varphi \rangle \mid \langle \varphi | \sum_{i=1}^N \delta(\mathbf{r} - \mathbf{r}_i) | \varphi \rangle = \rho(\mathbf{r}) \right\} \quad (2.1)$$

However, this construction is of no practical value since it actually requires the evaluation of the Hamiltonian (1.9). Only certain contributions like the Hartree energy $E_{Hartree}[\rho] = \frac{1}{2} \int d^3r' d^3r V_{ee}(\mathbf{r}-\mathbf{r}')\rho(\mathbf{r}')\rho(\mathbf{r})$ and the energy of the ionic potential $E_{ion}[\rho] = \int d^3r V_{ion}(\mathbf{r})\rho(\mathbf{r})$ can be expressed directly in terms of the electron density. DFT assumes existence of a functional of the form

$$E[\rho] = E_{kin}[\rho] + E_{ion}[\rho] + E_{Hartree}[\rho] + E_{xc}[\rho], \quad (2.2)$$

where $E_{kin}[\rho]$ denotes the kinetic energy (K.E.) and $E_{xc}[\rho]$ is the unknown exchange and correlation term which contains the energy of the electron-electron interaction except for the Hartree term. Hence all the difficulties of the many-body problem has been transferred into $E_{xc}[\rho]$. While the K.E. $E_{kin}[\rho]$ can not be expressed explicitly in terms of the electron density one can employ a trick to determine it. Instead of minimizing $E[\rho]$ w.r.t ρ one minimizes it w.r.t a set of one particle wave functions φ_i related to ρ via

$$\rho(\mathbf{r}) = \sum_{i=1}^N |\varphi_i(\mathbf{r})|^2 \quad (2.3)$$

To guarantee the normalization of φ_i , the Lagrange parameters ϵ_i are introduced such that the variation $\delta\{E[\rho] + \epsilon_i[1 - \int d^3r |\varphi_i(\mathbf{r})|^2]\}/\delta\varphi_i(\mathbf{r}) = 0$ yields the Kohn-Sham [3]

equations:

$$\left[-\frac{\hbar^2}{2m_e}\nabla^2 + V_{ion}(\mathbf{r}) + \int d^3r' V_{ee}(\mathbf{r} - \mathbf{r}')\rho(\mathbf{r}') + \frac{\delta E_{xc}[\rho]}{\delta\rho(\mathbf{r})} \right] \varphi_i(\mathbf{r}) = \epsilon_i \varphi_i(\mathbf{r}) \quad (2.4)$$

These equations have the same form as a one-particle Schrödinger equation which, *a posteriori*, justifies to calculate the K.E. by means of the one particle wave-function ansatz. The K.E. of a *one particle* ansatz which has the ground state density is, then, given by $E_{kin}[\rho_{min}] = -\sum_{i=1}^N \langle \varphi_i | \hbar^2 \nabla^2 / 2m_e | \varphi_i \rangle$ if the φ_i are the self-consistent (spin-degenerate) solutions of Eqs. (2.4) and (2.3) with lowest “energy” ϵ_i . Note, however, that the one particle potential of Eq. (2.4), i.e.,

$$V_{eff} = V_{ion}(\mathbf{r}) + \int d^3r' V_{ee}(\mathbf{r} - \mathbf{r}')\rho(\mathbf{r}') + \frac{\delta E_{xc}[\rho]}{\delta\rho(\mathbf{r})}, \quad (2.5)$$

is only an auxiliary potential which artificially arises in the approach to minimize $E[\rho]$. Here, the wave functions φ_i and the Lagrange parameters ϵ_i have no physical meaning at this point.

So far no approximations have been employed since all the difficulty of the many-body problem was transferred to the unknown functional $E_{xc}[\rho(\mathbf{r})]$. A very successful approximation for $E_{xc}[\rho(\mathbf{r})]$ has been provided by local density approximation (LDA) which approximates the functional $E_{xc}[\rho(\mathbf{r})]$ by a function that depends on the local density only, i.e.,

$$E_{xc}^{LDA}[\rho(\mathbf{r})] = \int \epsilon_{xc}^{hom}(\rho(\mathbf{r}))\rho(\mathbf{r})d\mathbf{r}, \quad (2.6)$$

where $\epsilon_{xc}^{hom}(\rho)$ is the exchange-correlation energy per electron of a uniform electron gas of density ρ . The non-uniform electron gas at \mathbf{r} is therefore treated as if it were part of a uniform electron gas of constant density $\rho = \rho(\mathbf{r})$. This approximation is obviously accurate when the electron density is almost uniform, but also works surprisingly well when the distribution of electron is strongly inhomogeneous. $E_{xc}^{LDA}[\rho(\mathbf{r})]$ is usually calculated from the perturbative solution [4] or the numerical simulation [5] of the homogeneous electron gas.

The analogous approximation for spin-polarized systems, which is known as the local spin-density approximation (LSDA), has also proved very successful. The local spin-density approximation is a straightforward generalization of the LDA to include electron spin:

$$E_{xc}^{LSDA}[\rho_{\uparrow}, \rho_{\downarrow}] = \int \epsilon_{xc}^{hom}(\rho_{\uparrow}, \rho_{\downarrow})\rho(\mathbf{r})d\mathbf{r} \quad (2.7)$$

Highly accurate formulae for the exchange-correlation energy density $E_{xc}^{LSDA}[\rho_{\uparrow}, \rho_{\downarrow}]$ have been constructed from Quantum Monte Carlo simulations of a free-electron gas.

A next level of approximations are the so-called generalized gradient approximations. Generalized gradient approximations (GGA) are still local but also take into account the gradient of the density at the same coordinate:

$$E_{xc}^{GGA}[\rho_{\uparrow}, \rho_{\downarrow}] = \int \epsilon_{xc}^{hom}(\rho_{\uparrow}, \rho_{\downarrow}, \vec{\nabla}\rho_{\uparrow}, \vec{\nabla}\rho_{\downarrow})\rho(\mathbf{r})d\mathbf{r} \quad (2.8)$$

Using the latter (GGA) very good results for molecular geometries and ground state energies have been achieved. Many further incremental improvements have been made to DFT by developing better representations of the functionals.

Altogether, these equations allow for the DFT/LDA calculation, see the flow diagram Figure 2.1.

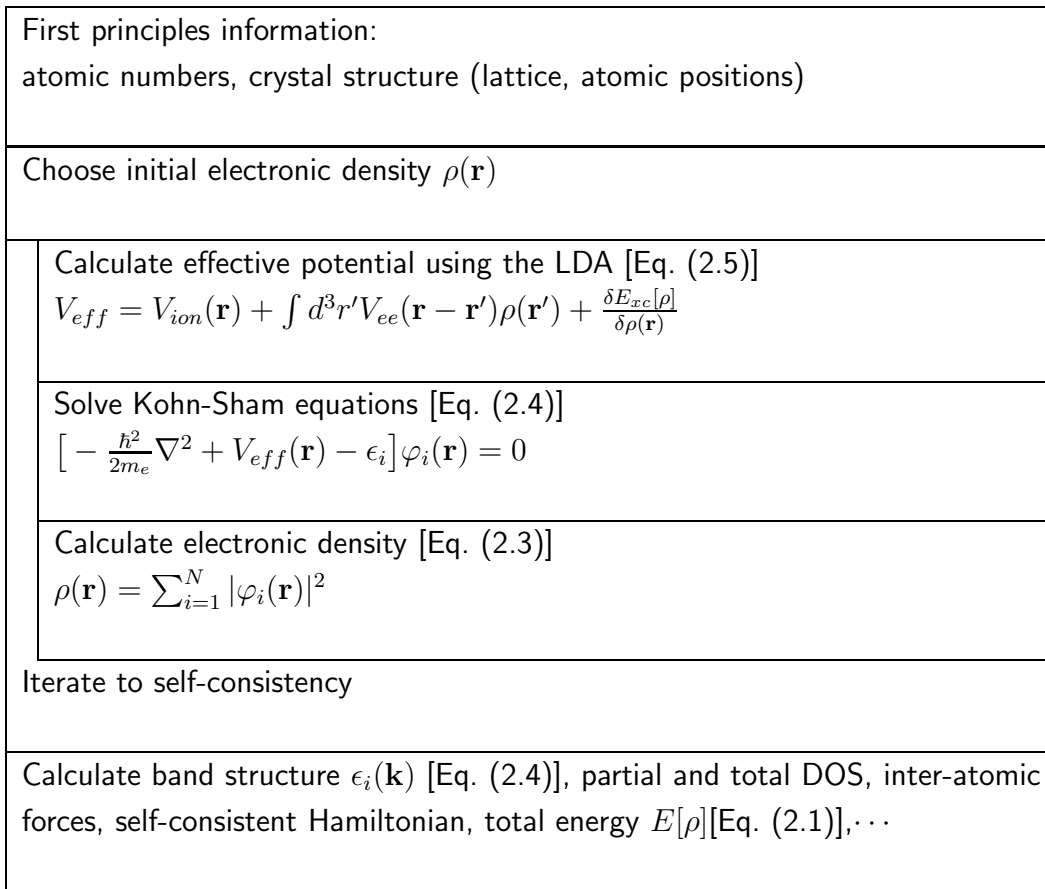


FIGURE 2.1: Flow diagram of the DFT/LDA calculations.

In principle DFT/LDA only allows one to calculate static properties like the ground state energy or its derivatives. However, one of the major applications of LDA is the calculation of band structures. To this end, the Lagrange parameters ϵ_i are interpreted as the physical (one-particle) energies of the system under consideration. Since the true ground state is not a simple one particle wave function, this is an approximation beyond DFT. Actually

this approximation corresponds to the replacement of the Hamiltonian (1.9) by

$$\begin{aligned} \hat{H}_{LDA} = & \sum_{\sigma} \int d^3r \hat{\Psi}^{\dagger}(\mathbf{r}, \sigma) \left[-\frac{\hbar^2}{2m_e} \nabla^2 + V_{ion}(\mathbf{r}) \right. \\ & \left. + \int d^3r' V_{ee}(\mathbf{r} - \mathbf{r}') \rho(\mathbf{r}') + \frac{\delta E_{xc}^{LDA}[\rho]}{\delta \rho(\mathbf{r})} \right] \hat{\Psi}(\mathbf{r}, \sigma) \end{aligned} \quad (2.9)$$

For particular calculation one needs to expand the field operators w.r.t. a basis. One particular band structure code differs from another in the choice of this basis function. For our purpose, we will be mostly using muffin-tin orbital based linear muffin-tin orbital (LMTO) [6] and N^{th} order muffin-tin orbital (NMTO) [7, 8] basis sets. The NMTO method which is not yet self-consistent relies on the self-consistent potential parameters derived from a LMTO calculation. To check the accuracy of our LMTO calculations we have also carried out full potential linear augmented plane waves (LAPW) calculations [9]. For materials, which are not structurally well-characterized we have also performed theoretical structural optimization in terms of *ab initio* molecular dynamics (AIMD) calculations [10] based on the Projected Augmented Wave (PAW) method [11] (see Section 3, 6, and 7).

2.2 Basis sets

2.2.1 Linear Muffin-Tin Orbital (LMTO) method:

The traditional basis sets may be divided into those which express the wave-functions as linear combinations of some fixed basis functions say plane waves or atomic orbitals and those like the cellular, Augmented Plane Wave (APW) and Korringa-Kohn-Rostoker (KKR) methods [12] which employ matching of partial waves. In the method of fixed basis sets by standard variation techniques one obtains a set of linear eigenvalue equations given by

$$(H - \epsilon O) \cdot \mathbf{b} = 0 \quad (2.10)$$

in terms of the Hamiltonian H and overlap matrix O to determine the eigenvalues ϵ and the expansion coefficients \mathbf{b} , while the methods of partial waves result in solving set of equations of the form,

$$M(\epsilon) \cdot \mathbf{b} = 0 \quad (2.11)$$

In contrast to equation (2.10) which is polynomial in ϵ , the secular equation (2.11) has a complicated non-linear energy dependence.

The partial wave methods though complicated to solve, do have advantages. Firstly, they provide solutions of arbitrary accuracy for a muffin-tin potential and for close packed systems, this makes them far more accurate than the traditional fixed basis methods. Secondly

the information about the potential enters only via a few functions of energy. However as already stressed, it has the disadvantage of being computationally heavy, the eigen energies ϵ_j must be found individually by tracing the roots of the determinant of M as a function of ϵ .

The linear methods devised by Andersen (1975) are characterized by using fixed basis functions constructed from partial waves and their first energy derivatives obtained within the muffin-tin approximation to the potential. These methods therefore lead to secular equations like (2.10) rather than (2.11). The linear methods thus combine the desirable features of the fixed basis and partial wave methods. In the LMTO [6] an energy dependent basis set $\chi_{RL}(r)$ is derived from the energy dependent partial waves in the form of muffin-tin orbitals.

The transformation of this method for self-consistent calculations of the electronic structure of solids into a first-principles tight-binding method (TB-LMTO) is particularly useful due to localized nature of basis functions, which will be particularly useful for the real space construction of model Hamiltonians.

The method relies on the muffin-tin approximation of the potential which divides the space into atom-centered muffin-tin spheres and the interstitial. While the solution of Schrödinger equation inside the spherically symmetric muffin-tin sphere is partial waves, that in the interstitial is plane waves which can be expanded in terms of spherical Neumann and Bessel functions. The basis is constructed by joining these two solutions at the muffin-tin sphere boundaries continuously and smoothly. Finally the LMTO basis is derived by linearising this energy dependent basis set. In the further steps towards simplification, the method relies on atomic sphere approximation (ASA) which replaces the muffin-tin spheres by space-filling atomic spheres, called Wigner-Seitz (WS) spheres. With the above mentioned approximations, the information needed to set up the Hamiltonian can be divided into two independent parts. The first part contains the structure matrix which depends only on the structure and the positions of the atoms and not on the type of atoms occupying the sites. The second part of the information depends on the solution of the Schrödinger equation inside each inequivalent WS sphere with appropriate boundary conditions. This second part yields the so-called potential parameters for each site.

Within the ASA, the LMTO basis functions have the following form:

$$\chi_{RL}^{\alpha}(r_R) = \phi_{RL}(r_R) + \sum_{R'L'} \dot{\phi}_{R'L'}^{\alpha}(r_{R'}) h_{R'L',RL}^{\alpha} \quad (2.12)$$

where L denotes collective angular momentum index (lm). Atomic sites are given by the position vectors \mathbf{R} with $\mathbf{r}_{\mathbf{R}} = \mathbf{r} - \mathbf{R}$. ϕ is a product of a spherical harmonic and the solution $\phi_{\nu RL}(|r_R|)$ to the radial wave equation, i.e., the partial waves inside the sphere centered at R for a certain energy $\epsilon_{\nu RL}$ which is the energy of linearization. The functions $\dot{\phi}^{\alpha}$ are

the linear combinations of the ϕ 's and their energy derivatives $\dot{\phi}$. The actual choice of how the linear combination is made determines the basis i.e. the label α . The functions ϕ are normalized inside the spheres to which they are associated, ϕ and $\dot{\phi}$ are orthogonal and they vanish, by definition outside their own sphere. The matrix h^α is given by

$$h^\alpha = C^\alpha - \epsilon_\nu + (\Delta^\alpha)^{1/2} S^\alpha (\Delta^\alpha)^{1/2} \quad (2.13)$$

where C^α and Δ^α are the diagonal potential matrices. They depend on the potential inside the spheres, the representation (α) chosen and on the sphere radii. The band center parameter C^α is given by

$$C^\alpha = \epsilon_\nu - \frac{P^\alpha(\epsilon_\nu)}{\dot{P}^\alpha(\epsilon_\nu)} \quad (2.14)$$

and the band width parameter is given by

$$\sqrt{(\Delta^\alpha)} = \frac{1}{\dot{P}^\alpha(\epsilon_\nu)} \quad (2.15)$$

where $P^\alpha(\epsilon)$ and $\dot{P}^\alpha(\epsilon)$ are the potential function and its energy derivative appropriate to the representation α . The relationship between the potential function $P^\alpha(\epsilon)$, the representation matrix α and the logarithmic derivative D_l of the partial wave at sphere boundary is given by

$$\left\{ P^\alpha(\epsilon) \right\}^{-1} = \left\{ 2(2l+1) \frac{D_l + l + 1}{D_l(\epsilon) - 1} \right\}^{-1} - \alpha \quad (2.16)$$

S^α is the structure constant matrix depending on the representation and the geometrical arrangement of the atomic sites. In terms of the canonical structure constant S^0 , S^α is given by

$$S^\alpha = S^0 (1 - \alpha S^0)^{-1} \quad (2.17)$$

The representation is uniquely defined by the choice of the α matrix. All representations span the same Hilbert space, and there exists an exact transformation from one representation to another. Two particular representations are of interest the γ -representation and the tight-binding (TB) representation, β . The former e.g. can be used in the construction of sp^3 hybrids for which it is convenient due to the orthogonality of the basis function. In the TB representation on the other hand the basis functions are very localized. The γ -representation Hamiltonian correct to second order in energy ($\epsilon - \epsilon_\nu$) is given by

$$H^{(2)} = \epsilon_\nu + h^\gamma = C^\gamma + (\Delta^\gamma)^{1/2} S^\gamma (\Delta^\gamma)^{1/2} \quad (2.18)$$

where ϵ_ν is the diagonal matrix containing the linearization energies. The overlap matrix in this representation is a unit, diagonal matrix and therefore this representation is also

referred to as the *orthogonal representation*. The transformation from the γ to the β representation involves a scaling of the potential parameters C and Δ , calculation of the real space structure constants S^β . With the choice

$$\beta = \left\{ \begin{array}{lll} 0.3485 & l = 0 & (s) \\ 0.05303 & l = 1 & (p) \\ 0.010714 & l = 2 & (d) \end{array} \right\} \quad (2.19)$$

the screened structure constants are found to be most localized with universal exponential decay in distance d measured in terms of WS radius w .

$$S_{l'm}^\beta = A.exp(-\lambda_{l'm}^\beta d/w) \quad (2.20)$$

for all the structures (f.c.c, b.c.c, h.c.p etc.). In this representation the TB orbitals are extremely compact, extending only to nearest neighbor shell.

For the purpose of self-consistency, particularly for open structures it is necessary to go beyond the ASA to attend the desired accuracy. This is done by including a correction term called combined correction. Including the combined correction, the Hamiltonian is given by

$$\begin{aligned} H^{(2)} &= \epsilon_\nu + h^\gamma - (\kappa_\nu^2 + V_0)\partial_{\kappa^2} h^\gamma \\ &= C^\gamma + (\Delta^\gamma)^{1/2} S^\gamma (\Delta^\gamma)^{1/2} - (\kappa_\nu^2 + V_0)\partial_{\kappa^2} h^\gamma, \end{aligned} \quad (2.21)$$

where $\epsilon = \kappa^2 + V_0$.

In the following all the self-consistent calculations have been carried out with TB-LMTO including the combined correction. For open structure in addition to atomic spheres, the empty spheres have been used to fill up the space without violating the maximum overlap criteria between the different spheres recommended within LMTO formalism. We have made use of both LDA and GGA for the exchange correlation part.

2.2.2 NMTO method:

Although the LMTO method has been highly successful in terms of computer inexpensive calculations of self-consistent electronic calculations, the essential disadvantages of the method are the followings:

- (i) The basis is complete to $(\epsilon - \epsilon_\nu)$ (i.e., 1st order) inside the sphere while it is only complete to $(\epsilon - \epsilon_\nu)^0=1$ (i.e., 0th order) in the interstitial which is inconsistent. It can be made consistent by removing the interstitial region by ASA.
- (ii) The non-ASA corrections, namely the combined corrections, may of course be included in the Hamiltonian and in the overlap matrices as discussed in previous section. But,(a)this makes the formalism heavy, and (b) basis must often be increased by multi-panel calculation.

(iii) The expansion of the Hamiltonian H in the orthogonal representation as a power series in the two centered tight-binding Hamiltonian h :

$$\langle \tilde{\chi} | (H - \epsilon_\nu) | \tilde{\chi} \rangle = h - hoh + \dots \quad (2.22)$$

is obtained only within ASA and excluding downfolding.

In step towards providing an energetically more accurate basis set that is based on MTO formalism and to rectify the disadvantages associated with LMTO basis, the N^{th} order MTO basis was introduced. The primary features of this method is:

- (i) It still has a Muffin-tin potential.
- (ii) Still uses the partial waves, ϕ within the atomic spheres.
- (iii) Instead of Neumann function it use screened spherical waves (SSWs) in the interstitial region.
- (iv) Out of partial waves and SSWs it define the kinked partial waves (KPWs).
- (v) It construct energy-independent NMTOs, which are superpositions of KPWs evaluated at $N + 1$ energy points.

In general, the members (labeled by $R'L'$) of the NMTO basis set for the energy mesh $\epsilon_0, \dots, \epsilon_N$ are superpositions,

$$\chi_{R'L'}^N(\mathbf{r}) = \sum_{n=0}^N \sum_{RL \in A} \phi_{RL}(\epsilon_n, \mathbf{r}) L_{nRL, R'L'}^{(N)}, \quad (2.23)$$

of the kinked partial waves, $\phi_{RL}(\epsilon, \mathbf{r})$ at the $N + 1$ points (labeled by n) of the energy mesh. Expression (2.23) is the energy-quantized form of Lagrange interpolation,

$$\chi^N(\epsilon) \approx \sum_{n=0}^N \phi(\epsilon_n) l_n^{(N)}(\epsilon), \quad l_n^{(N)}(\epsilon) \equiv \prod_{m=0, \neq n}^N \frac{\epsilon - \epsilon_m}{\epsilon_n - \epsilon_m}, \quad (2.24)$$

of a function of energy, $\phi(\epsilon)$, by an N th-degree polynomial, $\chi^N(\epsilon)$: The N th-degree polynomial, $l_n^{(N)}(\epsilon)$, is substituted by a matrix with elements, $L_{nRL, R'L'}^{(N)}$, the function of energy, $\phi(\epsilon)$, by a Hilbert space with axes, $\phi_{RL}(\epsilon, \mathbf{r})$, and the interpolating polynomial, $\chi^N(\epsilon)$ by a Hilbert space with axes, $\chi_{R'L'}^{(N)}(\mathbf{r})$.

A kinked partial wave is basically a partial wave with a tail joined continuously to it with a kink at a central, so-called hard sphere of radius a_R . As usual, the partial wave is $\varphi_{RL}(\epsilon, r) Y_L(\hat{\mathbf{r}}_R)$, where the function of energy is the regular solution of the radial Schrödinger equation,

$$- [r\varphi_{RL}(\epsilon, r)]'' = [\epsilon - v_R(r) - l(l+1)/r^2] r\varphi_{RL}(\epsilon, r), \quad (2.25)$$

for the potential-well $v_R(r)$. The tail of the kinked partial wave is so called *screen spherical wave*, $\psi_{RL}(\epsilon, \mathbf{r})$, which is essentially the solution with energy ϵ of the wave equation in the

interstitial between the hard spheres, $\Delta\psi(\varepsilon, \mathbf{r}) = \varepsilon\psi(\varepsilon, \mathbf{r})$, with the boundary condition that, independent of the energy, $\psi_{RL}(\varepsilon, \mathbf{r})$ go to $Y_L(\hat{\mathbf{r}}_R)$ at the central hard sphere, and to *zero* (with a kink) at all other hard spheres. The Lagrange coefficients, $L_n^{(N)}$, as well as the Hamiltonian and overlap matrices in the NMTO basis are expressed solely in terms of the KKR resolvent, $K(\varepsilon)^{-1}$, and its first energy derivative, $\dot{K}(\varepsilon)^{-1}$, evaluated at the energy mesh, $\varepsilon = \varepsilon_o, \dots, \varepsilon_N$.

This NMTO method gives rise to an energetically accurate and compact formalism for intelligible electronic structure calculation. The energy selective and localized nature of NMTO basis makes the NMTO set *flexible* and may be chosen as *truly minimal* (\equiv span selected bands with as few basis functions as there are bands) via the so called downfolding procedure [7, 8]. The downfolding procedure is an energy selection procedure which selectively picks up few bands of interest out of the LDA all band calculation by integrating out degrees of freedom that are not of interest, called passive channels and retaining few degrees of freedom, called active channels. The accuracy of such a procedure can be tuned by the choice of N , the number of energy points used in the NMTO calculation. If the selected bands are isolated, the NMTO set spans the Hilbert space of the Wannier functions and the orthonormalized NMTOs are the *Wannier functions*. Even if the bands overlap with other bands, it is possible to pick out those few bands and their corresponding Wannier-like functions with NMTO method. The NMTO method can thus be used for direct generation of Wannier or Wannier-like functions which can be used as effective orbitals that have the central character of an active orbital and the tails shaped according to passive, downfolded orbital characters. The real space representation of the downfolded Hamiltonian in the basis of NMTO provide the hopping matrix elements. This procedure of direct generation of Wannier function may be constructed with the procedure of constructing Wannier function out of computed Bloch functions through maximum localization criteria [13].

References

- [1] P. Hohenberg and W. Kohn, *Phys. Rev. B* **136**, 864 (1964).
- [2] M. Levy, *Proc. Natl. Acad. Sci. (USA)* **76**, 6062 (1979).
- [3] W. Kohn and L. J. Sham, *Phys. Rev.* **140**, A1133 (1965);
W. Kohn and L. J. Sham, *Phys. Rev.* **140**, 1133 (1965);
L. J. Sham and W. Kohn, *Phys. Rev.* **145**, 561 (1966).
- [4] L. Hedin and B. I. Lundqvist, *J. Phys. C: Solid State Phys.* **4**, 2064 (1971);
U. von Barth and L. Hedin. *J. Phys. C: Solid State Phys.* **5**, 1629 (1972).
- [5] D. M. Ceperley and B. J. Alder, *Phys. Rev. Lett.* **45**, 566 (1980).
- [6] O. K. Andersen, *Phys. Rev. B* **12**, 3060 (1975);
O. Gunnarsson, O. Jepsen and O. K. Andersen, *Phys. Rev. B* **27**, 7144 (1983);
O. K. Andersen and O. Jepsen, *Phys. Rev. Lett.* **53**, 2571 (1984).
- [7] O. K. Andersen, T. Saha-Dasgupta and S. Ezhov, *Bull. Mater. Sci.* **26**, 19 (2003).
- [8] O. K. Andersen and T. Saha-Dasgupta, *Phys. Rev. B* **62**, R16219 (2000).
- [9] O. K. Andersen, *Phys. Rev. B* **12**, 3060 (1975).
- [10] R. Car and M. Parrinello, *Phys. Rev. Lett.* **55**, 2471 (1985).
- [11] P. E. Blöchl, *Phys. Rev. B* **50**, 17953 (1994).
- [12] J. Callaway, *Energy Band Theory* Academic Press, New York, London (1964).
- [13] N. Marzari and D. Vanderbilt, *Phys. Rev. B* **56**, 12847 (1997).

3 Microscopic model for the frustrated Cu II -spin tetrahedron-based $Cu_4Te_5O_{12}X_4$ ($X = Cl, Br$) systems*

3.1 Introduction

Frustrated magnetism has gained a lot of attention in recent years due to the wealth of exotic behavior that arises out of this condition such as spin ice and spin liquid phases [1]. In the search for new materials exhibiting frustrated magnetism, a few years ago Johnsson *et al.* [2] synthesized a family of oxohalogenides $Cu_2Te_2O_5X_2$, $X=Br, Cl$ whose structure was based on weakly coupled tetrahedra of $Cu(II)$ with geometrically frustrated antiferromagnetic (AF) interactions. These materials have been intensively studied both experimentally and theoretically [3–6, 8–11]. They show magnetic ordering with incommensurate wave vectors at temperatures $T_N = 18$ K (Cl) and 11 K (Br) and the observation of a longitudinal magnon [5] in $Cu_2Te_2O_5Br_2$ was interpreted as evidence for the proximity of this system to a quantum phase transition between antiferromagnet and spin liquid behavior.

The various intratetrahedral and intertetrahedral couplings and the relative strengths of exchange pathways in these compounds have been obtained in detail [6] by using the electronic structure technique of muffin-tin orbital (MTO) based NMTO-downfolding [12]. The results predicted by this study have been confirmed by subsequent neutron diffraction experiments [13] proving the powerfulness of this *ab initio* Density Functional Theory (DFT) based method in predicting the underlying microscopic model of a complex material [7].

By changing the subtle ratio between the various interaction paths in these materials, for instance by applying pressure or by introducing chemical modifications [14–16], one can attempt to drive these systems into quantum criticality. Following these ideas, a new oxohalogenide $Cu_4Te_5O_{12}Cl_4$ has been very recently synthesized by Takagi *et al.* [17]

*This work has been published in *Phys. Rev. B* **75**, 024404 (2007)

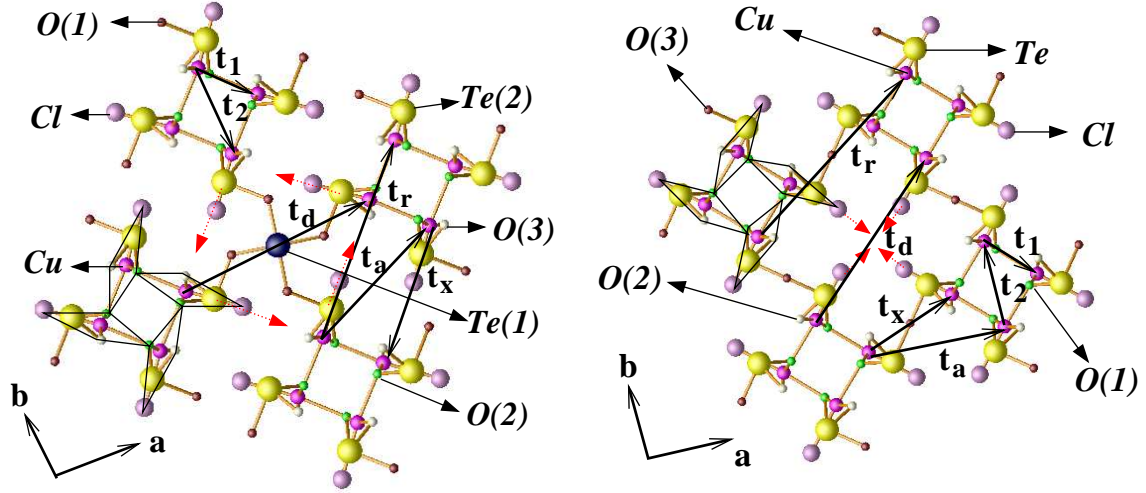


FIGURE 3.1: Crystal structure of Cu-45124(Cl) (left panel) and Cu-2252(Cl) (right panel) projected on the ab plane. In order to emphasize the similarity between the Cu-2252(Cl) and Cu-45124(Cl) structures, we use four unit cells of Cu-45124(Cl) but show only the section that makes this structure analogous to a section of four Cu-2252(Cl) unit cells showing four connected Cu tetrahedra. The balls representing various atoms are of varying sizes, Te being the largest, and Cl, Cu and O in order of decreasing sizes. Magenta and pink atoms stand for Cu and Cl. Two inequivalent Te atoms, Te(1) and Te(2) in Cu-45124(Cl) are shown in deep blue and yellow colors (left panel), while the only one inequivalent Te atom present in Cu-2252(Cl) is shown in yellow color (right panel). The smallest brown, green and white balls denote O(1), O(2) and O(3) respectively for Cu-45124(Cl) (left panel) and O(3), O(1) and O(2) for Cu-2252(Cl) (Ref. [18]). Note that every four Cu atoms appearing in a square arrangement, due to the projection, actually form tetrahedra. We also show the various interaction paths in black arrows (see the text for discussion).

which orders antiferromagnetically at $T_N = 13.6$ K. This system is structurally similar to the previously discussed $Cu_2Te_2O_5Cl_2$ but presents some markedly different features. As pointed out by Takagi *et al.*, the primary structural difference between the $Cu_4Te_5O_{12}Cl_4$ (which we refer to as Cu-45124(Cl) following Ref. [17]) and $Cu_2Te_2O_5Cl_2$ (Cu-2252(Cl)) is the presence of a TeO_4 complex in the middle of the Cu-tetrahedral network in the ab plane (see Fig. 3.1). This fact led the authors of Ref. [17] to expect an increase in the separation between the Cu_4 tetrahedra and hence an increase in the relative importance of the intratetrahedral coupling with respect to the intertetrahedral coupling.

In the following, we study this proposition within the framework of the NMTO-downfolding technique. In addition, motivated by the more anomalous properties of $Cu_2Te_2O_5Br_2$ compared to $Cu_2Te_2O_5Cl_2$ as reported in the literature [3–6, 8–11, 14, 15], we explore the implications of substituting Cl by Br in the Cu-45124(Cl). Since the Cu-45124(Br) system

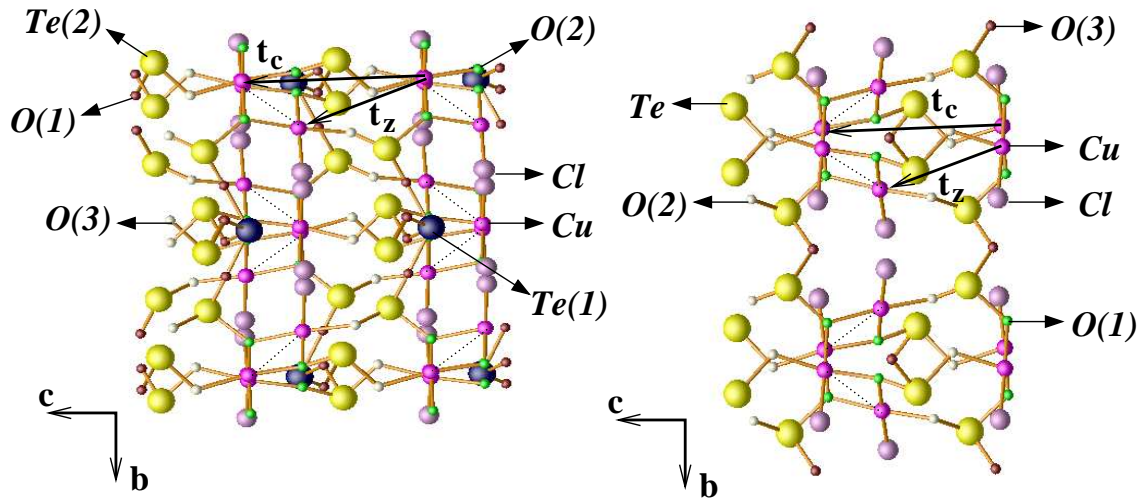


FIGURE 3.2: View of the crystal structure of the Cu-45124(Cl) (left panel) and Cu-2252(Cl) (right panel) compounds along the [001] direction. Color scheme and the convention for ball sizes is the same as in Fig. 3.1. The thick arrows denote the various interaction paths.

has not been synthesized yet, we propose the crystal structure of $\text{Cu}_4\text{Te}_5\text{O}_{12}\text{Br}_4$ by performing a geometry relaxation in the framework of *ab-initio* molecular dynamics and we analyze its electronic structure by the *NMTO*-downfolding technique.

3.2 Structure

Both Cu-45124(Cl) and Cu-2252(Cl) compounds crystallize in a tetragonal structure. The basic structural unit in both systems is the $[\text{CuO}_3\text{Cl}]$ distorted square (marked in thin lines in Fig. 3.1) with Cu (marked in magenta in Fig. 3.1) at the center. Groups of four such squares share corners, giving rise to $[\text{Cu}_4\text{O}_8\text{Cl}_4]$ units with Cu ions in tetrahedral coordination. Cu-45124(Cl) has two inequivalent Te atoms, Te(1) and Te(2) (marked in black and yellow in Fig. 3.1 left panel), while Cu-2252(Cl) has only one type of Te atoms (marked in yellow in Fig. 3.1 right panel). The Te(2) atoms in Cu-45124(Cl) sit on an equivalent position to the Te atoms in Cu-2252(Cl). Viewing the structures along the [001] direction (see Fig. 3.2), they show a stacking of Cu_4 tetrahedra separated by layers of Te(2)–O(3) (Cu-45124(Cl)) or Te–O(2) (Cu-2252(Cl)) units. In the case of Cu-45124(Cl), additional Te(1)–O(1) units appear in the same layer as Cu. The relative orientation of the Cu_4 tetrahedra along the [001] direction is also different between the two compounds. In the case of Cu-2252(Cl) the Cu_4 tetrahedra show the same orientation, while for Cu-45124(Cl) they alternate between

successive rows. The latter feature leads to two different space group symmetries, $P\bar{4}$ for Cu-2252(Cl) and $P4/n$ for Cu-45124(Cl) with elongation of the unit cell in the ab plane with lattice parameter $a = 11.35 \text{ \AA}$ for Cu-45124(Cl) compared to $a = 7.84 \text{ \AA}$ for Cu-2252(Cl). The unit cell dimensions along the c axis remain comparable with $c = 6.32 \text{ \AA}$ for Cu-2252(Cl) and $c = 6.33 \text{ \AA}$ for Cu-45124(Cl). The change in space group defines Cu-45124(Cl) as centrosymmetric compared to the non-centrosymmetric Cu-2252(Cl).

A crucial difference between the two compounds apart from the change in bond lengths, is the relative orientation of the Cu–Cl bonds (Cl atoms are marked in pink in Fig. 3.1) among different Cu_4 tetrahedra. As has been discussed in Ref. [6], the Cl atoms play an important role in mediating the Cu–Cu interaction in the Cu-2252 systems. While for Cu-2252(Cl) the Cu–Cl bonds belonging to different Cu_4 tetrahedra point towards each other (marked with red arrows in Fig. 3.1 right panel), in the case of Cu-45124(Cl), due to the relative shift of the tetrahedra, they are oriented parallel to each other (see the red arrows in Fig. 3.1 left panel). This aspect is found to have important consequences in the context of hopping interaction pathways as will be discussed later.

3.3 Bandstructure

Fig. 3.3 shows the non spin-polarized band dispersion of Cu-45124(Cl) obtained with the linear muffin-tin orbital (LMTO) basis [19] within the framework of local density approximation (LDA). The bands are plotted along the various symmetry directions of the tetragonal Brillouin zone. The orbital characters indicated in the figure are obtained by choosing the local coordinate system with the y axis pointing along the Cu–O(3) bond and the x axis pointing along the Cu–Cl bond. The square planar symmetry of the ligands surrounding the Cu^{2+} ion sets the $Cu-3d_{x^2-y^2}$ energy level as the highest energy level. Consistent with the Cu^{2+} valency, eight bands (there are 8 Cu atoms in the unit cell) dominated by $Cu-d_{x^2-y^2}$ character and split off from the rest of the bands, span an energy range from $\approx -0.3 \text{ eV}$ to 0.2 eV with the zero of energy set at the LDA Fermi level. The energy bands dominated by other d characters like d_{xy} , d_{zx} , d_{yz} and d_{3z^2-1} are located in the energy range between $\approx -3 \text{ eV}$ and -2 eV overlapping with the O- p manifold. The Cl- p dominated bands appear right above and partly overlapping the O- p bands within an energy range of $\approx -1 \text{ eV}$. These Cl- p dominated bands are separated by a gap of $\approx 0.5 \text{ eV}$ from the $Cu-d_{x^2-y^2}$ dominated bands. There is only a negligible contribution of Te(1) and Te(2) to the bands crossing the Fermi energy. We note that in the low-energy scale, the LDA calculation leads to eight almost half-filled bands, i.e., to a metallic state. Introduction of correlation effects within an LDA+U treatment are expected to drive the system insulating. In what follows though we will focus on the *ab initio* determination of effective one electron hopping interactions

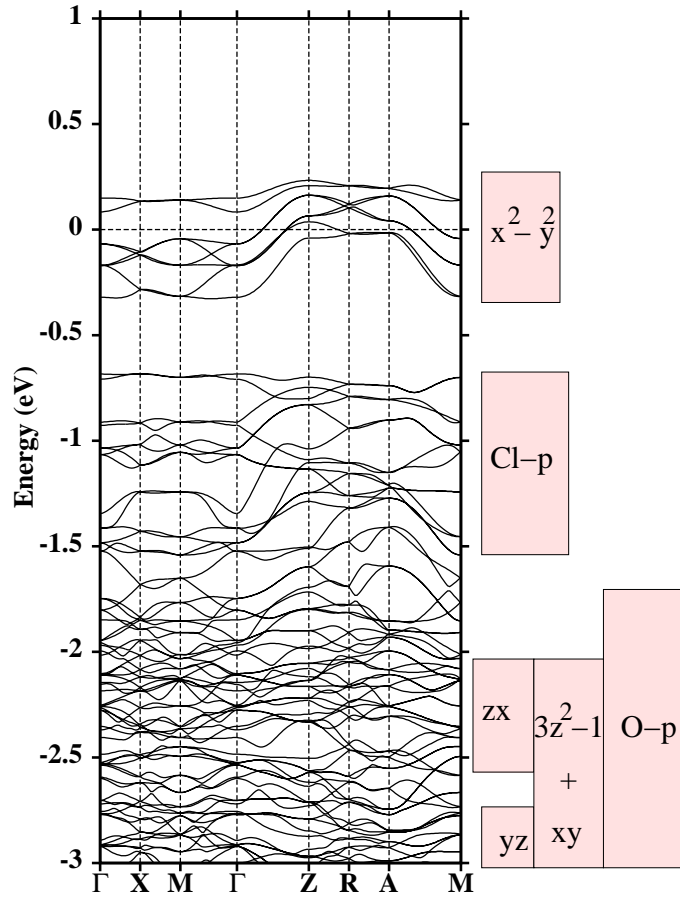


FIGURE 3.3: LDA band dispersion of Cu-45124(Cl) plotted along various symmetry directions with $\Gamma = (0, 0, 0)$, $X = (\pi, 0, 0)$, $M = (\pi, \pi, 0)$, $Z = (0, 0, \pi)$, $R = (0, \pi, \pi)$ and $A = (\pi, \pi, \pi)$. The dominant orbital contributions in various energy ranges are shown in small boxes drawn on the right hand side.

which are well described within LDA and GGA.

In Fig. 3.4 we show a comparative study of the various partial LDA density of states (DOS) for Cu-45124(Cl) and Cu-2252(Cl).

While the basic features of the DOS remain the same between the two compounds—indicating that the overall nature of the interactions will be similar for both systems—there are a few quantitative differences. The Cu-*d* bandwidth at E_F is narrower in Cu-45124(Cl) than in Cu-2252(Cl). The relative proportion of the Cl-*p* and O-*p* contribution to the bands at E_F is also smaller in the case of Cu-45124(Cl). The O-*p* and Cl-*p* dominated bands, instead of being separated, overlap to a larger extent in the case of Cu-45124(Cl). Understanding and quantifying these differences requires the analysis of the bandstructure in terms of a microscopic model.

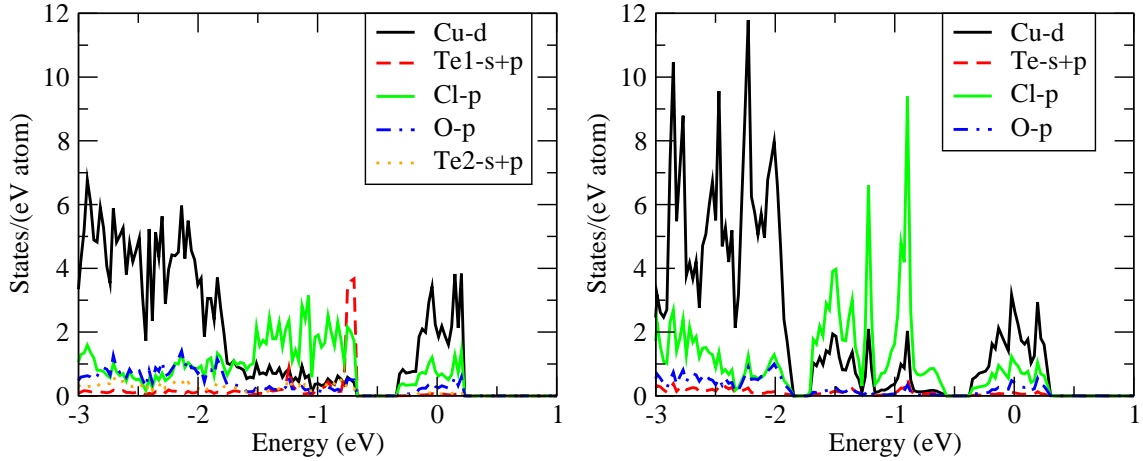


FIGURE 3.4: Comparison of the density of states between the Cu-45124(Cl) (left panel) and Cu-2252(Cl) (right panel) compounds.

3.4 Downfolding and effective model

A powerful technique to construct a low-energy, tight-binding (TB) Hamiltonian starting from a complex LDA bandstructure is achieved via the NMTO-downfolding technique [12] as introduced in previous section. For the present study, we construct the massively downfolded Hamiltonian by keeping only the $Cu-d_{x^2-y^2}$ degrees of freedom active and integrating out all the rest. The computed, downfolded bands are shown in the left panel of Fig. 3.5 with solid lines. With the choice of two energy points, E0 and E1, the downfolded bands are indistinguishable from the $Cu-d_{x^2-y^2}$ dominated bands of the full LDA calculation shown in dashed lines in the left panel of Fig. 3.5.

The corresponding Wannier function is plotted in Fig. 3.6. Two different views of the same orbital are shown. The central part has the $3d_{x^2-y^2}$ symmetry with the choice of the local coordinate system as stated above, while the tails are shaped according to $Cl-p_x$ and $O-p_x/p_y$ symmetry demonstrating the hybridization effects. The strong $pd\sigma$ antibonds are evident in the plot with Cu hybridization being stronger with Cl than with O, a fact also evident in the density of states plot, shown in Fig. 3.4.

The real space representation of the downfolded Hamiltonian in the Wannier function basis, $H_{TB} = -\sum_{ij} t_{ij} (\hat{c}_i^\dagger \hat{c}_j + h.c.)$ provides the information of the effective hopping interaction t_{ij} , between the Cu^{2+} ions at sites i and j . The various dominant hopping interactions are tabulated in Table 3.1. The notation for the hoppings are shown in Figs. 3.1 and 3.2. While the hoppings t_1 , t_2 , t_x , t_a and t_r are in-plane hoppings in the plane defined by the Cu tetrahedra, t_z and t_c are out-of-plane hoppings. For the sake of consistency, we adopt for Cu-45124(Cl) the same hopping notation introduced earlier for Cu-2252(Cl) in

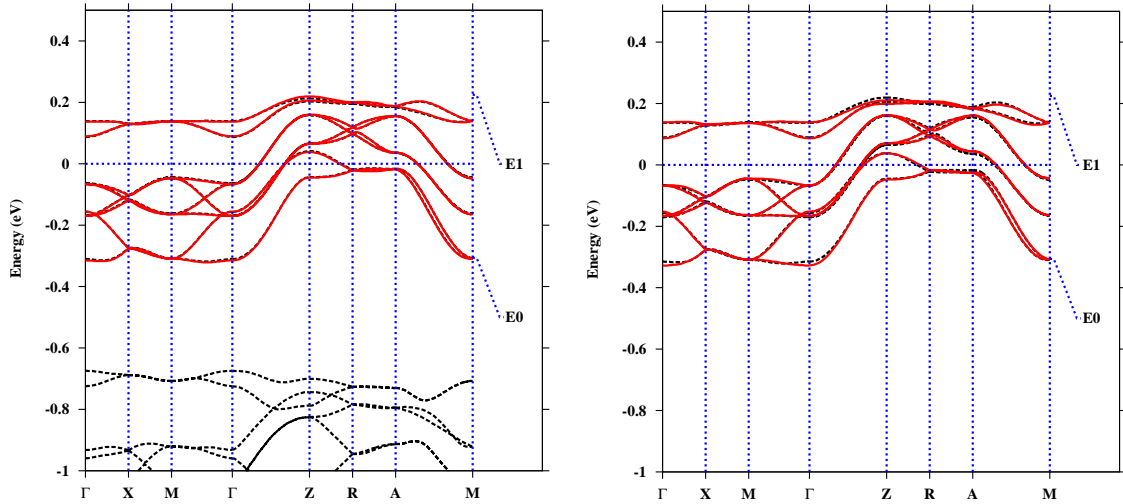


FIGURE 3.5: Left panel: Bands obtained with massively downfolded Cu $d_{x^2-y^2}$ basis (in solid lines) compared to full LDA band structure (in dashed lines). The NMTO energy points E_n spanning the region of interest are shown on the right-hand side. Right panel: The tight-binding bands obtained with the hopping interactions shown in Table. 3.1 (in dashed lines) compared with downfolded bands (in solid lines).

Ref. [6].

For comparison, in Table 3.1 we reproduce the results for the Cu-2252(Cl) compound from Ref. [6]. The bond lengths corresponding to each hopping element have been also tabulated. For the dominant, intratetrahedral nearest neighbor interaction, t_1 , we observe that while the bond length is decreased by only 2.5% for Cu-45124(Cl) compared to Cu-2252(Cl), t_1 is reduced by as much as 22% due to a smaller superexchange path angle in Cu-45124(Cl) ($\angle \text{Cu-O(2)-Cu} = 105.7^\circ$ for Cu-45124(Cl) and $\angle \text{Cu-O(1)-Cu} = 109.8^\circ$ for Cu-2252(Cl)). The intratetrahedral hopping t_2 which was weak for Cu-2252(Cl)—a fact also supported by neutron diffraction [10]—remains weak for Cu-45124(Cl). The in-plane intertetrahedral hopping t_x , remains in magnitude similar to its analog in Cu-2252(Cl) while other in-plane intertetrahedral hoppings like t_a and t_r get suppressed. The out-of-plane, intertetrahedral hopping, t_c remains more or less the same as in Cu-2252(Cl), while the t_z hopping increases by a factor of two. The most remarkable change is observed for the diagonal hopping, t_d , which is reduced to 7 meV in Cu-45124(Cl) compared to a value of 80 meV in the Cu-2252(Cl) compound. This reduction however is not caused by the elongation of the bond lengths due to the insertion of the Te(1)O_4 group in Cu-45124(Cl), as was suggested in Ref. [17]. We reveal the origin of this marked difference in the following in terms of a detailed analysis of the involved hopping paths.

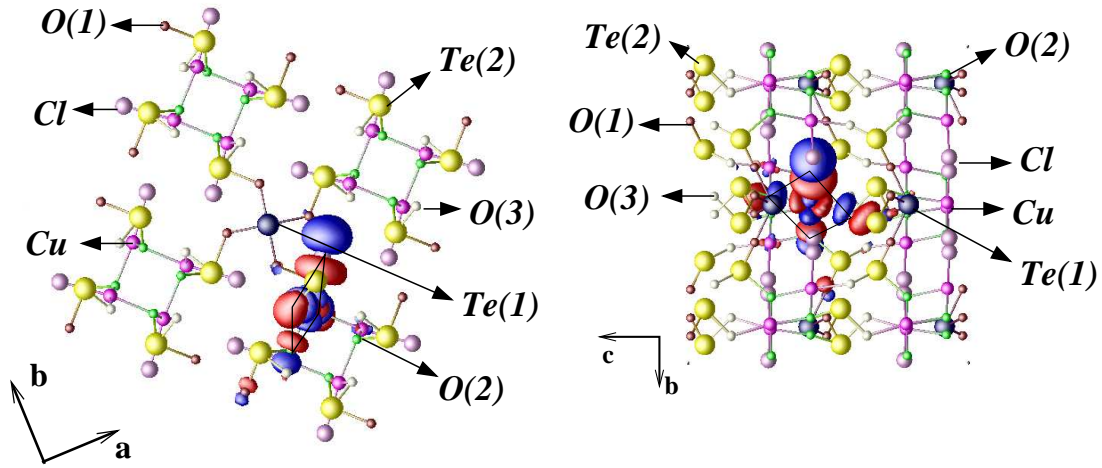


FIGURE 3.6: Effective orbital corresponding to massively downfolded $Cu-d_{x^2-y^2}$ calculation viewed in two different planes. Plotted are the orbital shapes (constant-amplitude surfaces) with lobes of opposite signs colored as red and blue. The $d_{x^2-y^2}$ orbital is defined with the choice of the local coordinate system with the y axis pointing along $Cu-O(3)$ and the x axis pointing along the $Cu-Cl$ bond within the square plane.

The tight-binding (TB) bands, constructed out of the hopping parameters tabulated in Table 3.1 are shown on the right panel of Fig. 3.5 in comparison to downfolded bands. The TB bands compare satisfactorily with the downfolded bands. Omission of long-ranged interactions such as t_c and t_r deteriorates the agreement of the TB bands with the downfolded bands, proving the essential need for inclusion of long-ranged interactions in the correct description of this compound.

3.5 Interaction pathways

It was pointed out in Ref. [6] that $Cl-p$ degrees of freedom play a crucial role in the renormalization process of the effective $Cu-Cu$ hopping. Keeping this fact in mind, we carried out downfolding calculations where the $Cl-p$ degrees of freedom have been kept active in addition to $Cu-d_{x^2-y^2}$, so as to define a basis consisting of $Cu-d_{x^2-y^2}$ and $Cl-p$. The $Cu-Cu$ hopping interactions extracted out of such calculation are tabulated in Table 3.2. For comparison, we show the results for $Cu-2252(Cl)$ reproduced from Ref. [6]. The crucial role of hopping paths involving $Cl-p$ is evident by comparing the hopping interactions between the massively downfolded $Cu-d_{x^2-y^2}$ -only calculation and the $Cu-d_{x^2-y^2} + Cl-p$ calculation. The

	Cu-45124(Cl)		Cu-2252(Cl)	
	Bond length	Interaction	Bond length	Interaction
t_1	3.147	76	3.229	98
t_2	3.523	4	3.591	0
t_x	5.539	12	4.163	-10
t_a	6.180	15	6.021	-29
t_d	7.834	7	8.033	-80
t_r	8.251	18	9.048	-48
t_z	5.063	24	5.015	12
t_c	6.332	-48	6.320	-45

Table 3.1: Cu–Cu hopping parameters corresponding to the massively downfolded Cu- $d_{x^2-y^2}$ Hamiltonian. The bond lengths are in Å and the hopping interaction strengths are in meV corresponding to hoppings shown in Figs. 3.1 and 3.2. The values for Cu-2252(Cl) have been reproduced from Ref. [6].

	Cu-45124(Cl)		Cu-2252(Cl)	
	Cu	Cu+Cl	Cu	Cu+Cl
t_1	76	82	98	181
t_2	4	-117	0	-132
t_x	12	42	-10	-14
t_a	15	-39	-29	8
t_d	7	9	-80	8
t_r	18	-11	-48	-72
t_z	24	27	12	33
t_c	-48	-15	-45	-19

Table 3.2: TB parameters in meV corresponding to two sets of calculations. Set-1: Massively downfolded Cu- $d_{x^2-y^2}$, Set-2: minimal set consisting of Cl- p and Cu- $d_{x^2-y^2}$ degrees of freedom (Cu+Cl downfolding). The numbers for Cu-2252(Cl) have been reproduced from Ref. [6]

former includes the renormalization due to Cl- p 's while the latter does not. While the pattern of renormalization remains essentially the same for the intratetrahedral hopping t_2 and the intertetrahedral out-of-plane hopping t_c , it is quite different for intertetrahedral hoppings like t_x , t_a , t_d , t_r and t_z which involve pathways via Cl atoms belonging to two different Cu₄ tetrahedra. The most significant change happens for the in-plane intertetrahedral diagonal hopping, t_d . The bare hopping strength of t_d in absence of the renormalization effect of Cl- p is more or less the same between the two compounds (8 meV for Cu-2252(Cl) and 9 meV for Cu-45124(Cl)). However, while a large renormalization is observed for Cu-2252(Cl) when

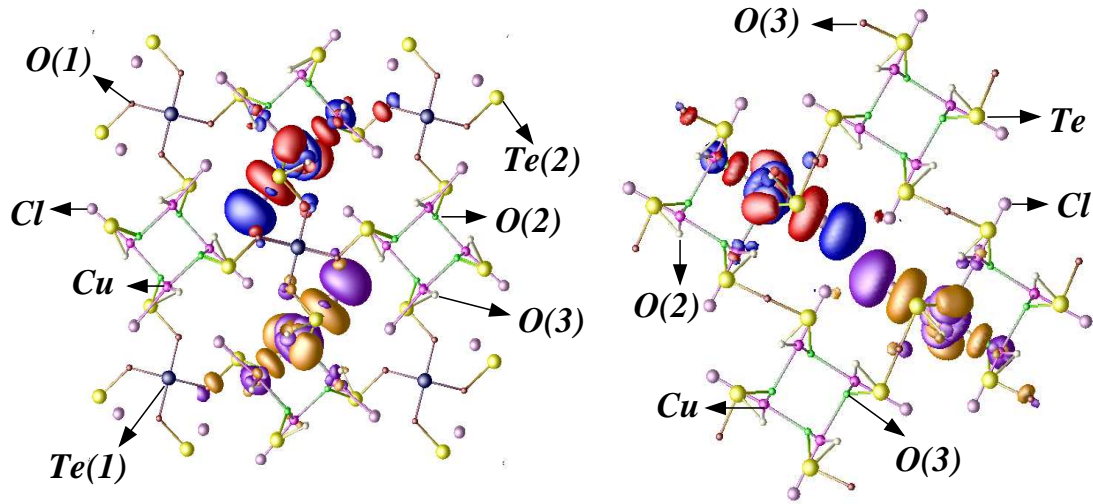


FIGURE 3.7: Overlap between $Cu-d_{x^2-y^2}$ downfolded NMTOs, placed at two Cu sites situated at in-plane intertetrahedral, diagonal positions. Opposite signed lobes of the orbitals are colored as blue or violet and red or orange.

integrating out the $Cl-p$ degrees of freedom, such renormalization is practically absent in $Cu-45124(Cl)$. This difference is caused—as pointed out previously—by the different alignment of the $Cu-Cl$ bonds belonging to neighboring Cu_4 tetrahedra which are parallel to each other in $Cu-45124(Cl)$ while in $Cu-2252(Cl)$ they point to each other. *This makes the intertetrahedral $Cl-p-Cl-p$ bonding in $Cu-45124(Cl)$ of $pp\pi$ type as opposed to the $Cu-2252(Cl)$ case, where the $Cl-p-Cl-p$ bonding was of $pp\sigma$ type.* This is nicely demonstrated in the Wannier function plot (see Fig. 3.7), where the effective $Cu-d_{x^2-y^2}$ like Wannier orbitals are placed at the Cu sites at in-plane diagonal positions. The overlap between the two orbitals provides a rough estimate of the strength of the hopping matrix elements. In the case of $Cu-2252(Cl)$, the $Cl-p$ tails from two Cu sites belonging to two different Cu_4 tetrahedra overlap to a large extent due to direct alignment providing a $Cl-p-Cl-p$ $pp\sigma$ bonding which mediates the $Cu-Cu$ bonding between different Cu_4 tetrahedra. For $Cu-45124(Cl)$, in contrast, the $Cl-p$ tails from different Cu sites belonging to two different Cu_4 tetrahedra have practically negligible contribution in the effective $Cu-Cu$ bonding due to misalignment of the $Cl-p$ tails.

The nature of the discussed interaction paths plays a crucial role in the magnetic properties of this material. Starting from the hopping parameters, t 's, the exchange integrals, J 's, for antiferromagnetic superexchange paths may be estimated by making use of the expression $J \approx 4t^2/U$. While this is a valid approach for cases like the t_1 and t_2 interaction paths, in general for more complicated paths this expression is not anymore precise and one

has to use more involved estimations of the exchange coupling constants. Nevertheless, already the knowledge of the hopping parameters gives us the clue about the important interaction paths. The drastic reduction of the in-plane t_d and to a lesser extent of t_a and the longer-ranged t_r , in Cu-45124(Cl) compared to Cu-2252(Cl), indicate an overall weakening of the intertetrahedral coupling in the Cu-45124(Cl) compound with respect to Cu-2252(Cl) and therefore if the system orders at low temperatures, the ordering should occur at a lower T_N than in Cu-2252(Cl), as observed experimentally [17]. The spin ordering patterns will be also strongly influenced by the change of interaction paths, especially by the near absence of the t_d and reduction of the t_a path (we refer to the discussion in Ref. [13]) which places the system in the limit of weakly coupled tetrahedra. Also the reduction by 22% of the t_1 value implies a smaller intratetrahedron exchange coupling J_1 than in Cu-2252(Cl). By considering $J \approx 4t^2/U$, with $U=4$ eV we obtain as exchange coupling constants $J_1 \approx 5.8$ meV = 67 K and $J_2 \approx 0.02$ meV = 0.2 K in comparison with the values $J_1 = 2.84$ meV = 32.9 K and $J_2 = 1.58$ meV = 18.4 K obtained by fitting the susceptibility of a model of independent tetrahedra to the experimental data [17]. The ratio of J_2/J_1 is largely overestimated in the fitting, presumably because of the neglect of the inter-tetrahedral interactions.

3.6 Br System

In an attempt to predict the properties of the not yet synthesized $\text{Cu}_4\text{Te}_5\text{O}_{12}\text{Br}_4$ (Cu-45124(Br)) and motivated by the discussed proximity to a quantum critical behavior of the recently studied $\text{Cu}_2\text{Te}_2\text{O}_5\text{Br}_2$ (Cu-2252(Br)), we have investigated the electronic and magnetic properties of the *ab initio* relaxed structure Cu-45124(Br) obtained from first principles calculations. In order to obtain a theoretical prediction of the Cu-45124(Br) crystal structure, we substituted Cl by Br in the original Cu-45124(Cl) structure and we relaxed the volume and internal coordinates by performing Car-Parrinello *ab initio* molecular dynamics (AIMD) calculations [20] with a projector augmented wave (PAW) basis set [21]. This procedure has proven to be very suitable for predicting reliable crystal structures [22]. For Cu-45124(Br) we assumed the same tetragonal space group $P4/n$ (No. 85) as for Cu-45124(Cl). Of the seven atoms in the primitive cell, only Te(1) is in Wyckoff position $2c$, while all others [Te(2), Cu, Br, O(1), O(2), O(3)] are in position $8g$. We thus have 19 degrees of freedom, but as the AIMD relaxation is done in the conventional cell, we need 131 constraints for the 50 atoms in order to preserve the symmetry. We verified convergence of our structure relaxation not only with the help of the forces but we checked that each of the 19 independent coordinates has converged. This is especially important in this structure as we find that the relaxation happens in two steps: First, immediately

	<i>x</i>	<i>y</i>	<i>z</i>
Te(1)	0.25	0.25	0.37660383
Te(2)	0.67370804	0.018727271	0.87086473
Cu	0.75587933	0.40510264	0.34817424
Br	0.89355065	0.56680922	0.32307512
O(1)	0.29531785	0.40609792	0.23273845
O(2)	0.28384154	0.87238649	0.36101169
O(3)	0.291597	0.58080843	0.93893775

Table 3.3: Fractional coordinates obtained by AIMD of the relaxed Cu-45124(Br).

after the Br atoms introduced into the Cl positions, they rearrange, increasing their bond distance to the Cu atoms which are the nearest neighbors. This Cu–Br repulsion makes an adjustment of the O(1) positions next to Br and the O(2) and O(3) positions next to Cu necessary. However, in course of further AIMD iterations, while the Br atom moves further and finds a relatively favorable position, some changes to Cu and O(1)–O(3) coordinates are actually reversed. Thus, the structure immediately following the first fast rearrangement would have produced quite different interactions strengths than the final relaxed structure given in Table 3.3. As would be expected from the different radii of Br and Cl atoms, we find the largest adjustments in the Br atom positions which change by 0.16 Å during the relaxation. The other changes are 0.05 Å for Te(1), 0.04 Å for Te(2), 0.04 Å for Cu, 0.10 Å for O(1), 0.04 Å for O(2) and 0.07 Å for O(3). While the volume of the Cu-45124(Br) structure shows a negligible change with respect to the volume of Cu-45124(Cl), appreciable changes in bond lengths and angles are observed. The Cu–O(2) distance which alternates between 1.94 Å and 2.01 Å in Cu-45124(Cl), becomes 1.91 Å and 2.01 Å in Cu-45124(Br). The Cu–O(3) distance is slightly smaller at 1.90 Å [from 1.91 Å in Cu-45124(Cl)]. The Cu–O(2)–Cu angle changes from 105.7° in Cu-45124(Cl) to 107.2° in Cu-45124(Br), while the O–Cu–O angle stays nearly constant at 87.0° [87.1° in Cu-45124(Cl)]. While the Cu–Cl distance is 2.24 Å, the Cu–Br distance 2.42 Å. Finally, the Cl–O(1) distances alternate between 3.27 Å and 3.40 Å while the Br–O(1) distances are 3.22 Å and 3.55 Å. In Table 3.3 we present the relaxed coordinates of Cu-45124(Br).

We performed NMTO-downfolding for this system and in Tables 3.4 and 3.5 we present the bond distance and hopping values together with those of [Cu-2252(Br)]. Both a Cu- $d_{x^2-y^2}$ and a Cu- $d_{x^2-y^2}+Br-p$ downfolding were performed.

Cu-45124(Br) shows the same trend as Cu-45124(Cl) regarding the intertetrahedral hopping t_d , namely the near absence of Cu–Cu interaction along this path. The rest of in-plane intertetrahedral hopping paths in Cu-45124(Br) are a bit larger than in Cu-45124(Cl) but, except for t_x , they are smaller than in Cu-2252(Br). From the knowledge of the previous

	Cu-45124(Br)		Cu-2252(Br)	
	Bond length	Interaction	Bond length	Interaction
t_1	3.147	75	3.195	80
t_2	3.522	0	3.543	4
t_x	5.535	23	4.385	-16
t_a	6.248	20	6.289	-30
t_d	7.829	3	8.439	-73
t_r	8.251	-29	9.130	-35
t_z	5.064	19	5.059	11
t_c	6.332	-39	6.378	-48

Table 3.4: Cu-Cu hopping parameters corresponding to the massively downfolded Cu- $d_{x^2-y^2}$ Hamiltonian. The bond lengths are in Å and the hopping interaction strengths in meV corresponding to hoppings shown in Figs. 3.1 and 3.2. The numbers for Cu-2252(Br) has been reproduced from Ref. [6].

	Cu-45124(Br)		Cu-2252(Br)	
	Cu	Cu+Br	Cu	Cu+Br
t_1	75	106	80	155
t_2	0	-60	4	-156
t_x	23	-15	-16	-10
t_a	20	-16	-30	5
t_d	3	11	-73	8
t_r	-29	-16	-35	-62
t_z	19	68	11	34
t_c	-39	-53	-48	-26

Table 3.5: Cu-Cu hopping parameters in meV corresponding to two sets of calculations. Set-1: Massively downfolded Cu- $d_{x^2-y^2}$, Set-2: Minimal set consisting of Br- p and Cu- $d_{x^2-y^2}$ degrees of freedom (Cu+Br downfolding). The numbers for Cu-2252(Br) have been reproduced from Ref. [6].

systems, a phase transition to an ordered state is also to be expected for this system at low temperatures.

An important issue to be mentioned at this point is the value of the intratetrahedron ratio t_2/t_1 in all the compounds discussed here. Large values of this ratio can be related to an enhancement of intratetrahedron frustration, what has been already discussed for Cu-2252(Br) [6]. Cu-2252(Br) is found to have a small but nonzero t_2 in comparison to its value for Cu-2252(Cl), where the t_2 hopping path is basically zero, mainly due to the Cl renormalization. The new set of systems, i.e the synthesized Cu-45124(Cl) and the

ab initio computer designed Cu-45124(Br) seem to behave in the opposite way. While Cu-45124(Cl) has a small but nonzero t_2 , Cu-45124(Br) relaxes into a structure where the t_2 path is completely renormalized to zero by the hybridization with the Br ions (see Table 3.5) in the square planar configuration. Though we found an interesting transient structure for Cu-45124(Br) with a moderate intratetrahedron t_2/t_1 , this doesn't seem to be the energetically favored structure within the AIMD approach.

Finally, we note that the value of the *ab initio* calculated hopping parameters is very susceptible to small changes of distances and angles between the atoms. Our AIMD calculations were performed within the GGA approximation. Consideration of other exchange correlation potentials may change slightly the relaxed structure, which could be important especially for the intratetrahedron hopping paths, where changes of 0.02 to 0.03 Å in the distance between Cu and O(2) and of 2.9° in the Cu-O(2)-Cu angle are decisive for the variation of the hopping parameters.

3.7 Summary

To conclude, we have made a comparative study between the spin tetrahedron system $\text{Cu}_2\text{Te}_2\text{O}_5\text{Cl}_2$ and a recently synthesized compound $\text{Cu}_4\text{Te}_5\text{O}_{12}\text{Cl}_4$ in terms of the microscopic analysis of the electronic structure. Our study shows that although the basic nature of the interactions remains the same, there is a drastic reduction of the in-plane intertetrahedral diagonal interaction in comparison to the case of $\text{Cu}_2\text{Te}_2\text{O}_5\text{Cl}_2$ where this diagonal interaction was estimated to be nearly as strong as the Cu_4 intratetrahedral nearest neighbor interaction t_1 . We show that the origin of this reduction is due to subtle changes in the crystal structure of $\text{Cu}_4\text{Te}_5\text{O}_{12}\text{Cl}_4$ which causes Cu-Cl bonds belonging to different Cu_4 tetrahedra to align in parallel in the $\text{Cu}_4\text{Te}_5\text{O}_{12}\text{Cl}_4$ compound rather than pointing towards each other as was the case in $\text{Cu}_2\text{Te}_2\text{O}_5\text{Cl}_2$. This reduction of the in-plane diagonal hopping in turn increases the importance of the out-of-plane hopping to the extent that some intertetrahedral hoppings along [001] (t_c) are even about three times stronger than those within the plane.

In absence of the, yet to be synthesized, $\text{Cu}_4\text{Te}_5\text{O}_{12}\text{Br}_4$ and motivated by the more anomalous properties observed in the Br analog to $\text{Cu}_2\text{Te}_2\text{O}_5\text{Cl}_2$, we have theoretically derived the hypothetical crystal structure of $\text{Cu}_4\text{Te}_5\text{O}_{12}\text{Br}_4$ by performing a geometry relaxation in the framework of *ab initio* molecular dynamics. We have analyzed the electronic properties of this system within the NMTO downfolding procedure. We observe that, while the overall electronic and magnetic behavior seems to be similar to its Cl sister compound, this computer designed Br system shows (except for t_d) a stronger in-plane intertetrahedron interaction than the Cl system—an effect that was also observed in the comparison between

$\text{Cu}_2\text{Te}_2\text{O}_5\text{Br}_2$ and $\text{Cu}_2\text{Te}_2\text{O}_5\text{Cl}_2$. However we don't observe any noticeable effect on the intratetrahedron frustration in the final relaxed $\text{Cu}_4\text{Te}_5\text{O}_{12}\text{Br}_4$ structure.

References

- [1] R. Moessner and A. Ramirez, *Physics Today* **59**, 24 (2006).
- [2] M. Johnsson, K. W. Törnroos, F. Mila and P. Millet, *Chem. Mater.* **12**, 2853 (2000).
- [3] P. Lemmens, K.-Y. Choi, E. E. Kaul, C. Geibel, K. Becker, W. Brenig, R. Valentí, C. Gros, M. Johnsson, P. Millet and F. Mila, *Phys. Rev. Lett.* **87**, 227201 (2001).
- [4] W. Brenig and K. W. Becker, *Phys. Rev. B* **64**, 214413 (2001).
- [5] C. Gros, P. Lemmens, M. Vojta, R. Valentí, K. Y. Choi, H. Kageyama, Z. Hiroi, N. Mushnikov, T. Goto, M. Johnsson and P. Millet, *Phys. Rev. B* **67**, 174405 (2003).
- [6] R. Valentí, T. Saha-Dasgupta, C. Gros and H. Rosner, *Phys. Rev. B* **67**, 245110 (2003).
- [7] T. Saha-Dasgupta, R. Valentí, F. Capraro and C. Gros, *Phys. Rev. Lett.* **95**, 107201 (2005).
- [8] J. Jensen, P. Lemmens and C. Gros, *Europhys. Lett.* **64**, 689 (2003).
- [9] V. N. Kotov, M. E. Zhitomirsky, M. Elhajal and F. Mila, *Phys. Rev. B* **70**, 214401 (2004).
- [10] O. Zaharko, A. Daoud-Aladine, S. Streule, J. Mesot, P.-J. Brown and H. Berger, *Phys. Rev. Lett.* **93**, 217206 (2004).
- [11] S. J. Crowe, M. R. Lees, D. M. K. Paul, R. I. Bewely, J. Taylor, G. McIntyre, O. Zaharko and H. Berger, *Phys. Rev. B* **73**, 144410 (2006).
- [12] O. K. Andersen and T. Saha-Dasgupta, *Phys. Rev. B* **62**, R16219 (2000);
O. K. Andersen, T. Saha-Dasgupta and S. Ezhov, *Bull. Mater. Sci.* **26**, 19 (2003).
- [13] O. Zaharko, H. Ronnow, J. Mesot, S. J. Crowe, D. McK. Paul, P. J. Brown, A. Daoud-Aladine, A. Meents, A. Wagner, M. Prester and H. Berger, *Phys. Rev. B* **73**, 064422 (2006).

-
- [14] P. Lemmens, K.-Y. Choi, G. Güntherodt, M. Johnsson, P. Millet, F. Mila, R. Valentí, C. Gros and W. Brenig, *Physica B* **329**, 1049 (2003).
- [15] J. Kreitlow, S. Süllow, D. Menzel, J. Schoenes, P. Lemmens and M. Johnsson, *J. Magn. Magn. Mater.* **290**, 959 (2005).
- [16] X. Wang, I. Loa, K. Syassen, P. Lemmens, M. Hanfland and M. Johnsson, *J. Phys.: Condens. Matter* **17**, 807 (2005).
- [17] R. Takagi, M. Johnsson, V. Gnezdilov, R. K. Kremer, W. Brenig and P. Lemmens, *Phys. Rev. B* **74**, 014413 (2006).
- [18] Please note that we used the atom labelling given in Refs. [2] and [17].
- [19] O. K. Andersen and O. Jepsen, *Phys. Rev. Lett.* **53**, 2571 (1984).
- [20] R. Car and M. Parrinello, *Phys. Rev. Lett.* **55**, 2471 (1985).
- [21] P. E. Blöchl, *Phys. Rev. B* **50**, 17953 (1994).
- [22] L. A. Salguero, H. O. Jeschke, B. Rahaman, T. Saha-Dasgupta, C. Buchsbaum, M. U. Schmidt and R. Valentí, *New J. of Phys.* **9**, 26 (2007).

4 Electronic structure and microscopic model of $V_2GeO_4F_2$ —a quantum spin system with $S = 1^*$

4.1 Introduction

In this section, we take up the case of vanadium oxide fluoride system, namely $V_2GeO_4F_2$ which has recently been synthesized [1]. The nominal valence of V ion in this compound is 3^+ which puts this system in the category of $S=1$ system. The preliminary susceptibility measurement indicates the basic exchange interactions to be of antiferromagnetic nature and having the signature of low-dimensional behavior. The compound, therefore is a promising candidate for low-dimensional QSS. We present the LDA electronic structure of the compound, and starting from such description we derive $V-t_{2g}$ only low-energy, few-orbital Hamiltonian by means of $NMTO$ -downfolding calculations. We also present the quantitative estimates of the dominant exchange interactions and infer the possible spin-model based on those estimates.

4.2 Crystal structure

$V_2GeO_4F_2$ occurs in primitive orthorhombic space group $Pnma$ with four formula unit in the unit cell and lattice constants, $a = 9.336 \text{ \AA}$, $b = 8.898 \text{ \AA}$ and $c = 4.912 \text{ \AA}$ [1]. The immediate surrounding of V^{3+} ion is constituted of two F^{2-} ions and four O^{2-} ions giving rise to a distorted octahedral geometry with one short V–F, one intermediate V–F and four long V–O bonds (see Fig. 4.1 (a)). The F atom belonging to the short V–F distance occupies the apical position of the octahedra, pointed approximately along the crystallographic c -axis, while the other F belongs to the approximate ab plane. There are three different types of O atoms, O1, O2 and O3 as marked in Fig. 4.1. One of the O3 atoms occupies the second apical position and another goes in the plane. O1 and O2 occupies the other two positions

*This work has been published in *J. Phys.: Condens. Matter* **19**, 296206 (2007)

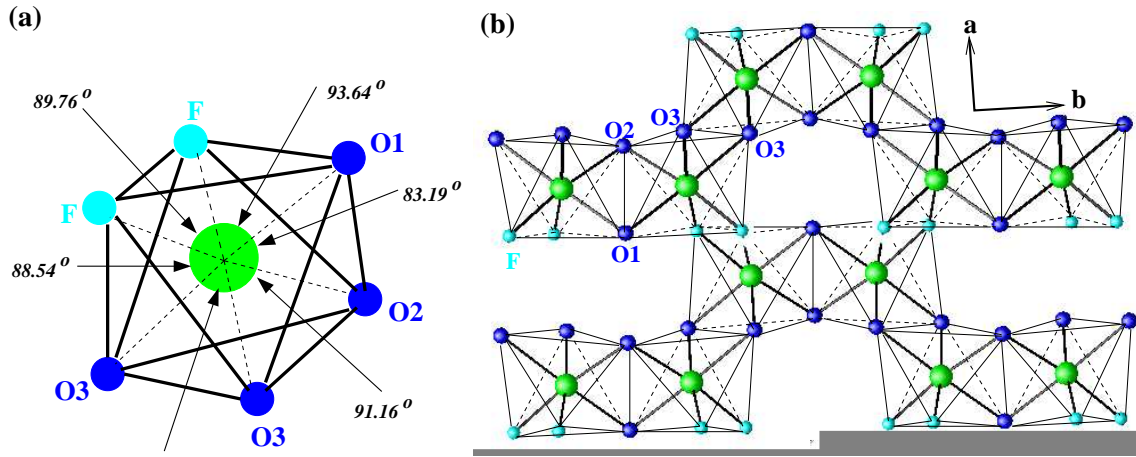


FIGURE 4.1: (a) The octahedral surrounding of V^{3+} ion consisting of four O-s and two F-s. Various bond angles are marked in the figure. The various bond lengths, in clock wise order starting from V–O1, are given by V–O1=1.990 Å, V–O2=1.998 Å, V–O3(1)=1.996 Å, V–O3(2)=2.014 Å, V–F(1)=1.928 Å and V–F(2)=1.864 Å. (b) Projection of zig-zag chains of VO_4F_2 octahedra.

in the plane. The nearest-neighbor (NN) VO_4F_2 octahedra edge-share via O1–O2 and form a pair, oriented along the crystallographic b -direction. The second-nearest-neighbor VO_4F_2 octahedra also edge-share via O3–O3, thereby giving rise zig-zag chain like structure of VO_4F_2 octahedra of composition VO_4F_2 , which is connected to next zig-zag chain by means of corner-sharing via the plane F (see Fig. 4.1(b)). The Ge^{4+} ion is co-ordinated by four oxygen atoms giving rise to GeO_4 tetrahedra which sit in the hollow formed between $V_2O_6F_4$ units. The co-ordination of GeO_4 tetrahedra with VO_4F_2 octahedra via the corner-shared O atoms gives rise to a three-dimensional network (see Fig. 4.2) with no direct connection between two VO_4F_2 octahedra along the crystallographic c -direction.

4.3 LDA Electronic structure

The self-consistent electronic structure calculation within the framework of local density approximation (LDA) of density functional theory (DFT) has been carried out in the tight-binding linear muffin-tin orbital (TB-LMTO) basis. The basis set consisted of Ge sp , V spd , F sp and O sp . Eight different classes of empty spheres were used to space fill the system. The self-consistency was achieved using 64 k-points in the irreducible Brillouin zone (BZ). The calculated band structure and the corresponding density of states are shown in Fig. 4.3. The octahedral surrounding of anions around the V ion, splits the V d -manifold into t_{2g} and e_g manifold. The distortion of the octahedra further splits the strict degeneracy of t_{2g}

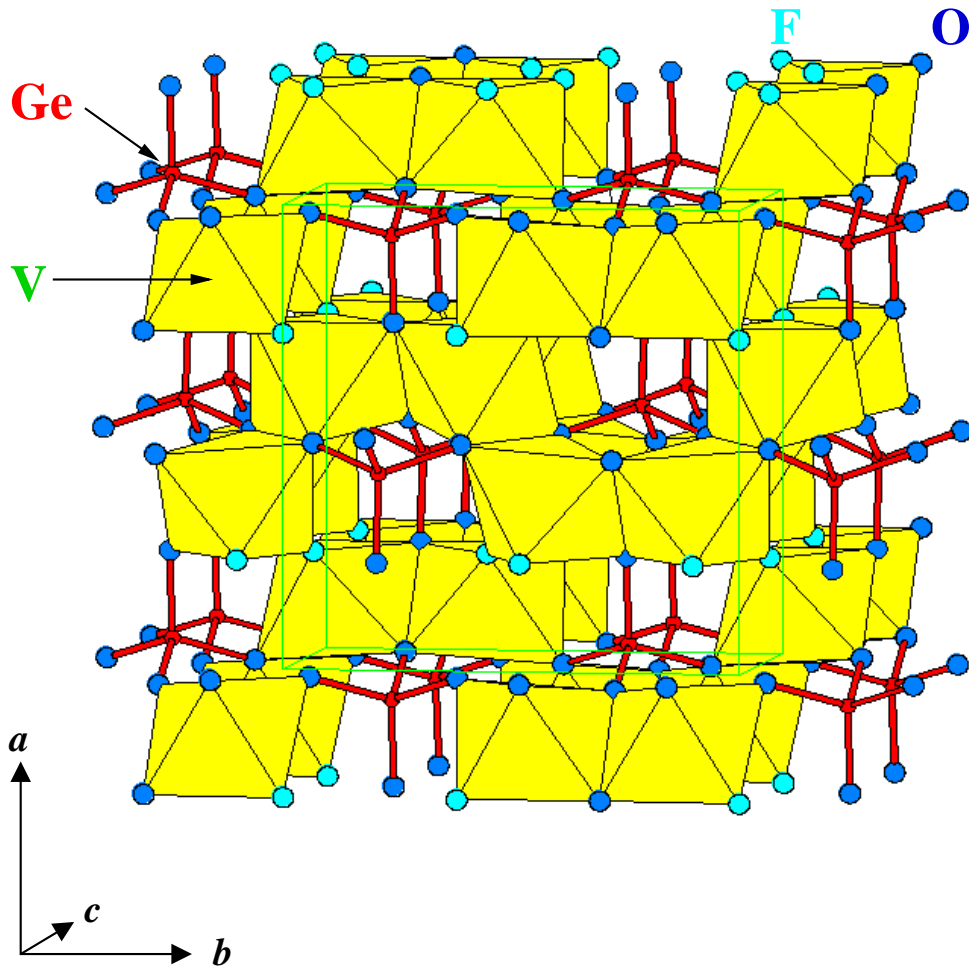


FIGURE 4.2: Crystal structure of $V_2GeO_4F_2$ showing the three-dimensional network of VO_4F_2 octahedra and GeO_4 tetrahedra.

and e_g manifolds with splitting of the order of ≈ 0.05 eV and small admixture between t_{2g} and e_g states. This causes 24 $V-t_{2g}$ bands to cross the Fermi level—there are 8 V atoms in the unit cell, each contributing three t_{2g} bands. The $V-e_g$ dominated states lie higher up in energy, crystal split by about 1 eV from the $V-t_{2g}$ bands crossing the LDA Fermi level. The $O-p$ and $F-p$ dominated bands are split from the $V-d$ manifold by a gap of about 3.5 eV and occupy energy range below -4 eV or so. The Ge dominated states appear high up in energy and remain essentially empty. The dominant band characters spanning various energy ranges are shown in Fig. 4.3(a) with bars. For $V-d$ characters, the anion-based local co-ordinate is chosen with the local \hat{z} -axis pointing along the short $V-F$ bond and local \hat{x} -axis pointing approximately along the other $V-F$ bond. Examining the density of states, we see V -dominated states have contributions from both $O-p$ and $F-p$. $O-p$ contribution is

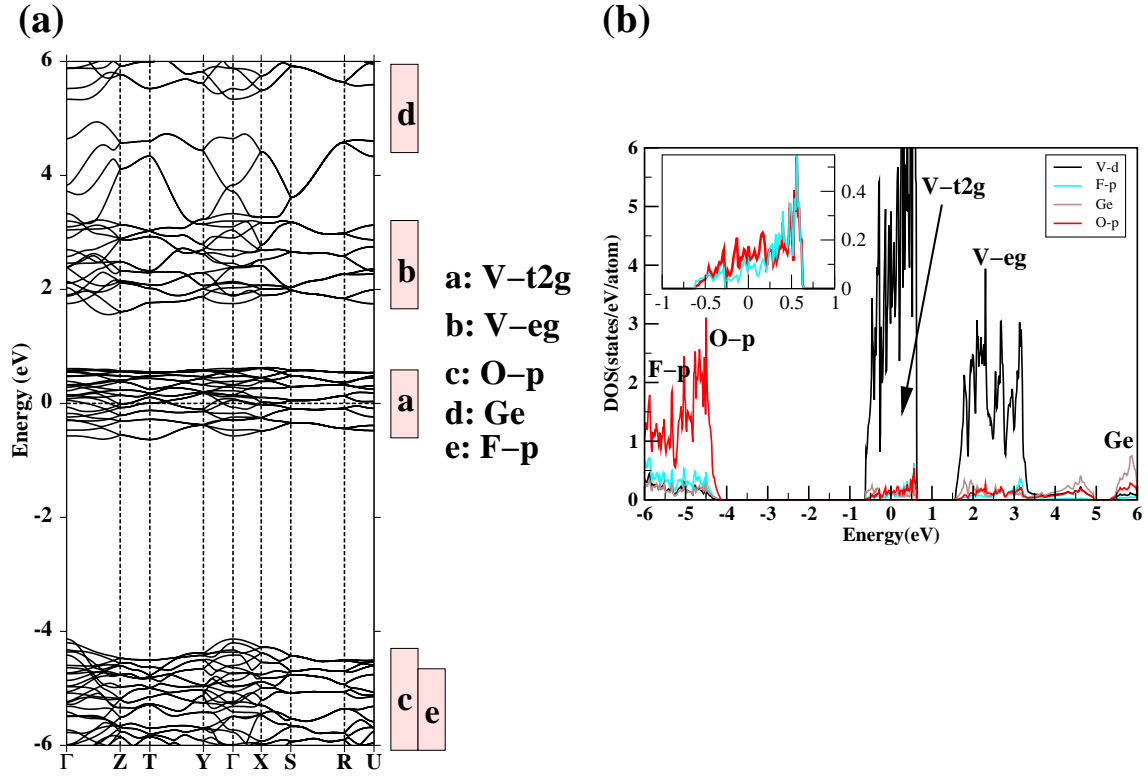


FIGURE 4.3: (a) LDA band structure of $V_2GeO_4F_2$. The bands are plotted along the high symmetry points of the orthorhombic BZ, Γ (0,0,0), Z(0,0, π/c), T(0, π/b , π/c), Y(0, π/b ,0), X(π/a ,0,0), S(π/a , π/b ,0), R(π/a , π/b , π/c) and U(π/a ,0, π/c). The zero of energy is set at the LDA Fermi energy. The bars mark the energy regions with respective dominant orbital characters. (b) LDA site and orbital-projected density of states of $V_2GeO_4F_2$. The inset shows the F- p and O- p projected density of states in the region of dominant V- t_{2g} character.

a bit larger than F- p , which indicates somewhat larger hybridization with O than with F (see inset of Fig. 4.3(b)). This happens due to larger on-site energy differences between V- d and F- p , compared to that between V- d and O- p , though the V-O bonds are on average longer than V-F bonds by about 0.1 Å.

We note that LDA predicts the system to be metallic. It is well-known that LDA fails to describe the correct insulating ground state for strongly correlated electron system, as is the case here. The inclusion of the missing correlation effect beyond LDA in a partially filled V- d manifold provides the insulating description of the system. We have checked this by treating the correlation within the LDA+U framework. Although LDA fails to provide the correct ground state for this class of materials, it describes the bonding and chemistry aspects correctly. This method has been highly successful in deriving the microscopic model based on such information [2] and construction of Hubbard-like Hamiltonians by adding the missing correlation effect to the LDA derived one-electron part. In spite of the failure of

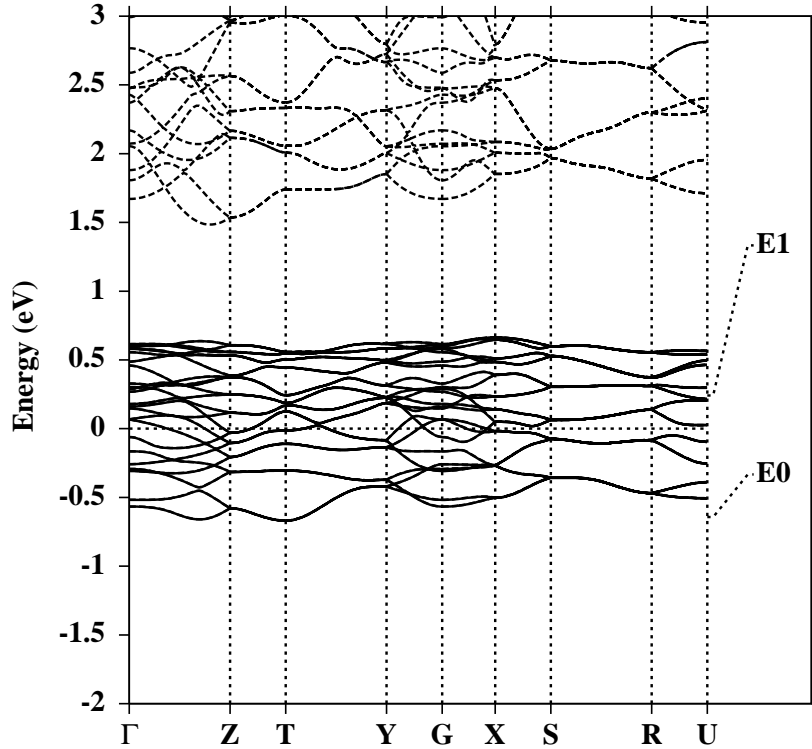


FIGURE 4.4: Downfolded t_{2g} (solid lines) bands of $V_2GeO_4F_2$ in comparison with LDA all-band structure (dotted lines). The zero of the energy is set at the LDA Fermi energy. E0 and E1 denote the energy points used in *NMTO*-downfolding calculation to pick up V - t_{2g} only bands.

LDA in prediction of correct ground state, the computed one electron part is found to be surprising robust and gives a very good account of the chemical aspect of even a correlated insulator, as is the case in discussion. Extraction of the essential LDA information, however needs filtering of the full LDA details. In the following, we applied the N -th order muffin-tin orbital (*NMTO*) based downfolding technique, which has been designed to serve this purpose.

4.4 *NMTO*-downfolding and the hopping interactions

For application of *NMTO*-downfolding technique to the present case, we generate the few-band, downfolded Hamiltonian constructed out of effective V - t_{2g} orbitals by integrating out all the degrees of freedom associated with Ge, O and F, and also the e_g states of V. This choice is driven by the fact that the vanadium is nominally in V^{3+} state with two electrons in the t_{2g} manifold. Therefore these are the bands that appear close to Fermi energy

$(i, j) \rightarrow$ $(m', m) \downarrow$	Dimer intrn. (0-1)	Intn. via O (0-2)	Intn. via F (0-3)
xy, xy	296	-68	37
yz, yz	58	-177	16
xz, xz	-67	-79	-114
xy, yz	-56	-49	-125
yz, xy	56	49	1
xy, xz	-73	125	43
xz, xy	-73	125	15
yz, xz	-107	-23	16
xz, yz	107	23	-116

Table 4.1: Hopping interactions, $t_{m,m'}^{i,j}$ in meV between m and m' orbitals situated at V sites belonging to the central octahedra, marked as 0, and the neighboring octahedra marked as 1, 2 and 3 (see Fig. 4.5).

and contribute in defining the low-energy Hamiltonian. The downfolded band-structure, in comparison with full LDA band structure, is shown in Fig. 4.4. With choice of two energy points of expansion, marked as E0 and E1 in the figure 4.4, the downfolded bands are indistinguishable from the full band structure within the region of interest. This indicates well convergence of the downfolded t_{2g} bands which in the present case form an isolated set of bands. The underlying NMTOs, therefore *are* the corresponding Wannier functions.

In Fig. 4.5, we show the three t_{2g} Wannier functions which have the central xy , yz or xz character defined in the local co-ordinate system specified earlier, and have tails shaped according to integrated out O- p or F- p character. Shown are the orbital shapes with two different lobes colored differently. We note the $pd\pi$ antibonds formed between V- t_{2g} and O- p , and V- t_{2g} and F- p , with somewhat stronger weights at O sites compared to that at F sites in conformity with the conclusions drawn from density of states plot. We also note non-negligible weight of the tails sitting at neighboring V sites. The tails sitting at neighboring V sites are shaped according to V- e_g like symmetry that occurs due to the distorted geometry of VO_4F_2 octahedra and the resultant mixing between t_{2g} and e_g . The quantitative estimates of various hopping interactions, $t_{m,m'}^{i,j}$, between the orbital m at the V site, i , belonging to the central VO_4F_2 octahedra, and the orbital m' at the V sites j 's, belonging to neighboring VO_4F_2 octahedra marked as 1, 2, 3 in Fig. 4.5 (m and m' run from 1 to 3, with $|1\rangle \equiv xy$, $|2\rangle \equiv yz$ and $|3\rangle \equiv xz$) are listed in Table. 4.1. We consider only the dominant V-V interactions, namely the nearest neighbor (NN) V-V dimer interaction that proceeds via O1 and O2, the second-nearest-neighbor V-V interaction that proceed via two

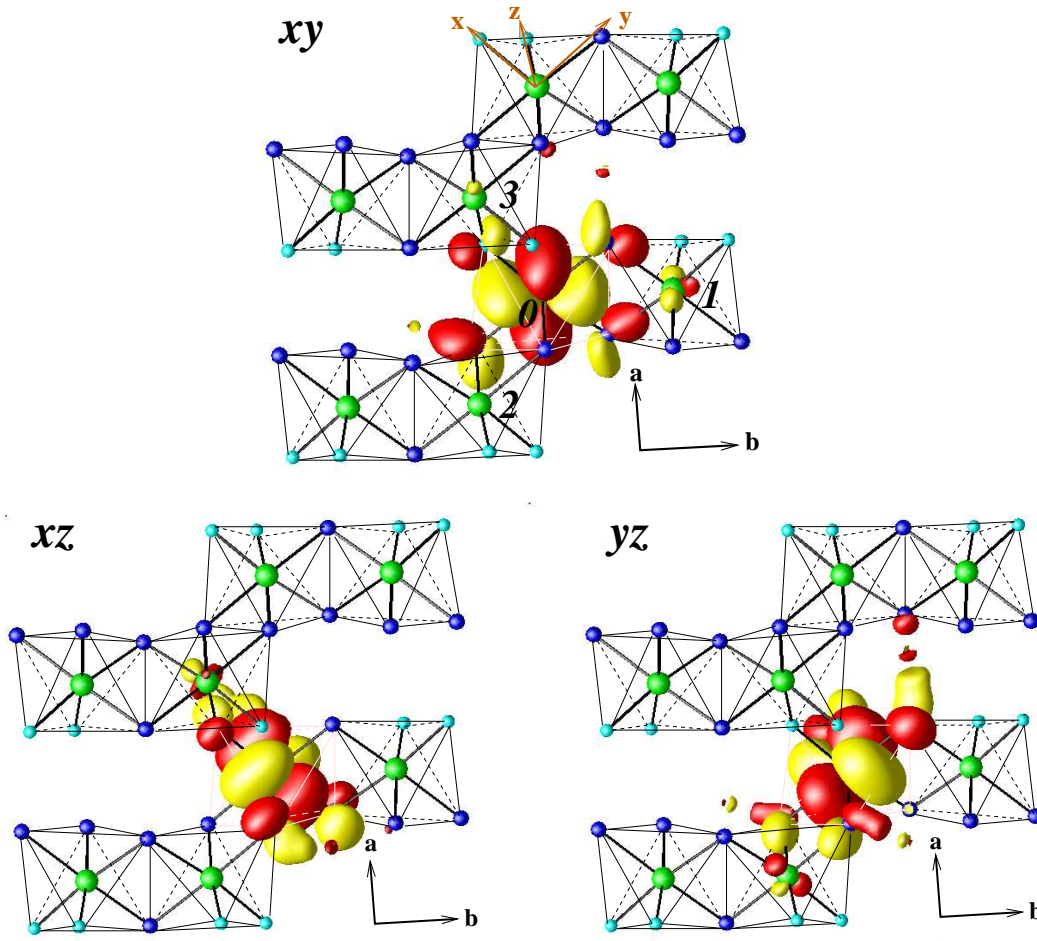


FIGURE 4.5: t_{2g} NMTOs for $V_2GeO_4F_2$. Shown are the orbital shapes, with the positive and negative lobes colored with red and yellow. The neighboring octahedra surrounding the central octahedra (marked as 0) are numbered as follows: the NN octahedra edge sharing with the central octahedra via O1 and O2 is marked as 1, the 2NN octahedra edge sharing with the central octahedra via O3s is marked as 2 and the 3NN octahedra corner sharing with the central octahedra via F is marked as 3. The local co-ordinate system used to define the xy , xz and yz orbitals is shown in the first figure. The Ge atoms have been omitted from the structure for clarity.

O3 atoms, and the third-nearest-neighbor V–V between two VO_4F_2 octahedra that corner share via the F atom. Rest of the interactions are order of magnitude smaller. Examining the shapes of the downfolded xy , yz and xz Wannier functions, we conclude the NN V–V interaction has to be strongest, contributed primarily by $V\text{-}xy - V\text{-}xy$ exchange path, while the 2NN V–V interaction is contributed primarily by $V\text{-}yz - V\text{-}yz$ exchange path and the 3NN V–V interaction is contributed primarily by $V\text{-}xz - V\text{-}xz$. The real-space representation of the downfolded Hamiltonian in the basis of Wannier functions, listed in

Table. 4.1 reveal also strong contributions arising from inter-orbital hoppings between $V-yz$ and $V-xz$ for NN, between $V-xy$ and $V-xz$ for 2NN, and between $V-xy$ and $V-yz$, and $V-xz$ and $V-yz$ for 3NN.

4.5 Magnetic exchange interactions and the microscopic model

Starting from the t_{2g} Hubbard Hamiltonian given by, $H_{t_{2g},RR'}^{LDA} + U_{R=R'}^{t_{2g}}$, where U is the on-site Coulomb repulsion, one may derive the super-exchange (SE) Hamiltonian, which plugging in various hopping interactions, provides the estimates of the magnetic interaction J^{ij} between V sites i and j . In deriving such an expression, we assume that the ground state is fully occupied by electrons in state $|1\rangle$ and $|2\rangle$ as confirmed by our LDA+ U calculations. Following the standard approach of second order perturbation, since the hopping interaction involves only two sites in the process of hopping, the difference between the excited state $|\beta\rangle$ and the zero-th order ground state $|\alpha\rangle$ is only in these two sites. For both sites, the atomic $|\alpha\rangle$ is a two-electron state, while one of the atomic $|\beta\rangle$ state is one-electron and the other is three-electron state. The energy of the ground state configuration is therefore given by $E_\alpha = 2(U_2 - J_H)$, where U_2 is the Coulomb repulsion between electrons belonging to different orbitals and J_H is the Hund's rule coupling. U , the Coulomb repulsion between electrons in the same orbital is $U = U_2 + 2J_H$. On the other hand, the energy of the excited state E_β consists only of three-electron site contribution, as the one-electron site does not contribute to the subspace of doubly occupied sites.

Considering the full, multiplet structure of excited states $|\beta_\lambda\rangle$ with three-electron sites, it is possible to show that there are three distinct excited energies, $3(U_2 - J_H)$, $3U_2$ and $3U_2 + 2J_H$ [3]. Considering the various possible matrix elements between the ground state configurations and excited states, and the energy differences between the Néel state and the ferromagnetic state as done in Ref. [4] for the case of t_{2g} manifold occupied by one electron, one gets

$$J_{SE}^{ij} = \left[(t_{11}^{ij})^2 + (t_{22}^{ij})^2 + (t_{12}^{ij})^2 + (t_{21}^{ij})^2 \right] \left[\frac{1}{U + 2J_H} + \frac{1}{U} \right] \\ + \left[(t_{13}^{ij})^2 + (t_{31}^{ij})^2 + (t_{23}^{ij})^2 + (t_{32}^{ij})^2 \right] \left[-\frac{1/3}{U - 3J_H} + \frac{1/3}{U} \right]$$

In the above we have neglected the crystal field splitting Δ between different m and m' level which is about $0.012 U$. Putting values of various $t_{mm'}^{ij}$'s and using $U = 4$ eV and $J_H = 0.8$ eV as appropriate for an early transition metal like V, gives all the exchange interactions to be of antiferromagnetic nature (see Table 4.2) in agreement with the preliminary susceptibility measurement [1]. The strongest interaction, J_1 , (J_{ij} , $i = 0$, $j = 1$)

i, j	J_{ij} (meV)
0-1 (dimer intrn.)	38
0-2 (intrn. via O)	13
0-3 (intrn. via F)	5

Table 4.2: Magnetic exchange interaction, J^{ij} , between V^{3+} ions belonging to the central octahedra (marked as 0) and the neighboring octahedra marked as 1, 2 and 3 (see Fig. 4.5).

is given by nearest neighbor pair, followed by the 2NN interaction, J_2 , (J_{ij} , $i = 0$, $j = 2$) which connects two V ions via two O3 atoms and is about one-third of the strongest NN interaction. The 3NN interaction, J_3 , (J_{ij} , $i = 0$, $j = 3$) that proceeds via the F atom is weak—1/8th of the NN V pair interaction. The above study therefore leads to a description of $V_2GeO_4F_2$ as that of a weakly coupled, $S=1$ alternating chain compound with alternation parameter ≈ 0.3 , where the alternation parameter is given by the ratio J_2/J_1 .

Antiferromagnetic (AF) $S=1$ spin chains gives rise to rather interesting properties. For uniform chains the ground state is an exotic quantum spin liquid with only short-range spin correlation and a gap in the excitation spectra, known as Haldane gap [5]. Antiferromagnetic $S=1$ chains that are not uniform, but instead feature alternating strong and weak bonds, are also gaped spin liquids except at quantum critical point [6]. However for sufficiently strong alternation, as may possibly be the case in the present, the so-called dimerized ground state is qualitatively distinct from Haldane state. These differences are significant yet subtle [7]. In literature, there have been considerable interest in distinction of behavior of two such systems like $Ni(C_6D_{24}N_4)(NO_2)ClO_4$ [NTENP] and $Ni(C_5H_{12}N_2)_2N_3(PF_6)$ [NDMAP] [8, 9]. It will be interesting to carry out similar studies to find out what is the nature of possible gap in case of $V_2GeO_4F_2$, which we predict to be a $S=1$ quasi one-dimensional bond-alternating AF.

4.6 Conclusion

In summary, using first-principles calculations, we study the electronic properties of the oxide-fluoride quantum spin system, $V_2GeO_4F_2$ which has been synthesized recently. We have analyzed the computed electronic structure in terms of $NMTO$ -downfolding which provided the effective hopping interactions between V^{3+} ions. Employing these estimates of hopping interactions, we derive the magnetic exchange interactions, which defines the

system as a weakly coupled, antiferromagnetic $S=1$ alternating spin chain. This forms an interesting class of QSS. Our prediction needs to be tested in terms of rigorous experimental study.

References

- [1] S. N. Achary, A. K. Tyagi and J. Köhler, *J. Solid State Chem.* **165** 74 (2002).
- [2] R. Valentí, T. Saha-Dasgupta, J. V. Alvarez, K. Pozgajcic and C. Gros, *Phys. Rev. Lett.* **86**, 5381 (2001);
R. Valentí and T. Saha-Dasgupta, *Phys. Rev. B* **65**, 144445 (2002);
R. Valentí, T. Saha-Dasgupta and C. Gros, *Phys. Rev. B* **66**, 054426 (2002);
T. Saha-Dasgupta and R. Valentí, *Europhys. Lett.* **60**, 309 (2002);
R. Valentí, T. Saha-Dasgupta and F. Mila, *Phys. Rev. B* **68**, 024411 (2003);
R. Valentí, T. Saha-Dasgupta, C. Gros and H. Rosner, *Phys. Rev. B* **67**, 245110 (2003);
T. Saha-Dasgupta, R. Valentí, H. Rosner and C. Gros, *Europhys. Lett.* **67**, 63 (2004);
T. Saha-Dasgupta, R. Valentí, F. Capraro and C. Gros, *Phys. Rev. Lett.* **95**, 107201 (2005).
- [3] S. Di Matteo, N. B. Perkins and C. R. Natoli, *Phys. Rev. B* **65**, 054413 (2002).
- [4] E. Pavarini, A. Yamasaki, J. Nuss and O. K. Andersen, *New J. Phys.* **7**, 188 (2005).
- [5] F. D. M. Haldane, *Phys. Lett A* **93** 464 (1983);
F. D. M. Haldane, *Phys. Rev. Lett.* **50** 1153 (1983).
- [6] M. Hagiwara *et al*, *Phys. Rev. Lett.* **80** 1312 (1998).
- [7] M. Hagiwara *et al*, *Preprint cond-mat/0501207* (2005).
- [8] A. Escuer *et al*, *J. Chem. Soc. Dalton Trans.* 531 (1997)
- [9] A. Zheludev *et al*, *Phys. Rev. B* **68** 134438 (2003);
A. Zheludev *et al*, *Phys. Rev. B* **69** 054414 (2004).

5 Electronic structures and low-dimensional magnetic properties of the ordered rocksalt oxides

$Na_3Cu_2SbO_6$ and $Na_2Cu_2TeO_6$ *

5.1 Introduction

Magnetic oxides with an ordered rocksalt structure often show low-dimensional behavior due to either the topology of the cation ordering or to orbital ordering, especially with Jahn-Teller active ions. For example, the thermodynamically stable form of $LiMnO_2$ with $Pmmn$ symmetry has zigzag layers of Mn^{3+} ions and shows short-range, two-dimensional magnetic correlations over a wide temperature range before long-range order sets in below 271 K [1]. More remarkably, the metastable form of this same material, $t-Li_2Mn_2O_4$, with $I4_1/amd$ symmetry and a three-dimensional (3D) topology for the Mn^{3+} ions, shows only two-dimensional spin correlations down to 2 K [2]. The material Li_4MgReO_6 , in which the Re^{6+} ($S=1/2$) ions are arrayed on a geometrically frustrated lattice, shows spin-glass behavior below 12 K and not long-range order [3].

Quite recently oxides with a layered rocksalt structure, $Na_2Cu_2TeO_6$ and $Na_3Cu_2SbO_6$, have been investigated [4, 5], which occur in distorted honeycomb crystal structures. Such a lattice structure with low coordination of magnetic ions is expected to exhibit strong magnetic fluctuations, characteristic of low-dimensional spin systems. These compounds fall in the category of quaternary cuprate-tellurate and cuprate-antimonate which have so far remained largely unexplored. The relationship between the two structures which has been described before [4, 5], may be summarized as follows:

Fig. 5.1(a) and 5.1(b) show the $Na_3Cu_2SbO_6$ structure viewed along the a and c axes of the $C2/m$ cell. Note the presence of layers of edge-sharing Cu–O and Sb–O octahedra separated by Na^+ ions. One Na^+ site is vacant in the tellurate phase, so it can be considered as a

*This work has been published in *Phys. Rev. B* **76**, 104403 (2007)

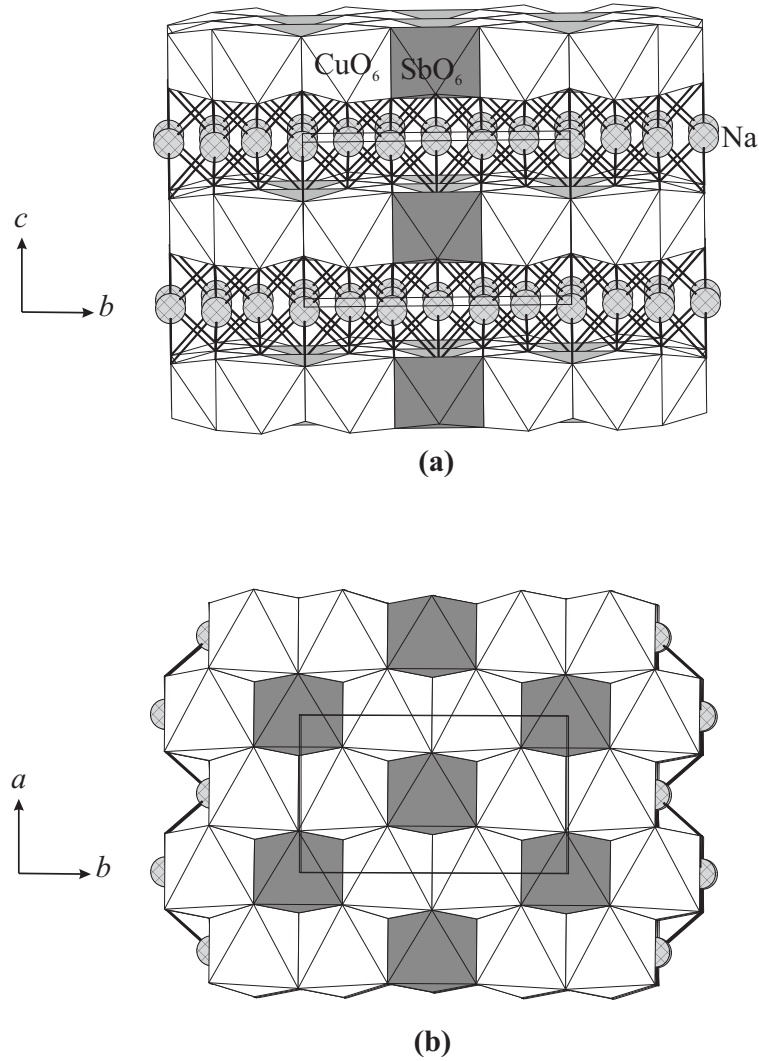


FIGURE 5.1: Edge-sharing octahedra in $Na_3Cu_2SbO_6$ viewed along the a direction (a) and the c direction (b).

defect rocksalt material. The magnetic Cu^{2+} ions lie in planes of composition $Cu_2TeO_6^{2-}$ or $Cu_2SbO_6^{3-}$ and, due to site ordering with the Te^{6+} and Sb^{5+} ions, present a slightly distorted honeycomb lattice topology, as shown in Fig. 5.2. There are five possible exchange pathways within the ab plane. Two possible pathways J_4 and J_5 are relatively long, involving fully occupied d_{z^2} orbitals and, as such, their contribution is negligible. As a result, they have not been taken into account in any subsequent analysis. The three most significant nearest-neighbor exchange pathways are J_1 , J_2 , and J_3 . Depending on their signs and relative magnitudes, the magnetic dimensionality can be 0, 1, or 2 as indicated in Table 5.1. The magnetic susceptibility data suggests a dominant dimeric or zero-dimensional interaction. Closer inspection indicates that an alternating linear chain model provides a somewhat

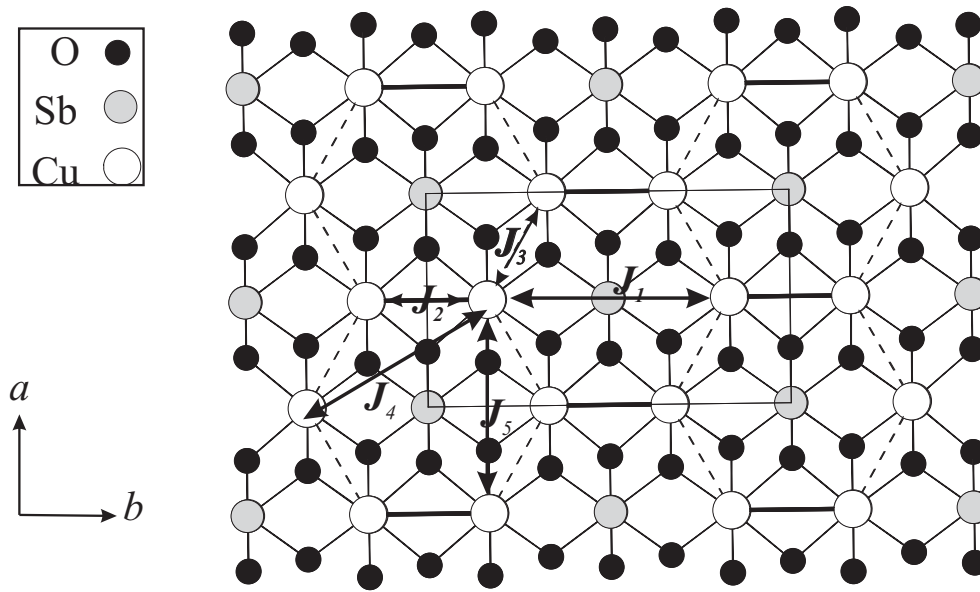


FIGURE 5.2: Schematic representation of different possible Cu–Cu interaction pathways in the ab plane. The thick solid lines denote the shortest Cu–Cu interactions, the thin solid lines show Cu–O and Sb–O connectivity, and the dashed lines represent the shortest interchain interactions.

better fit than the dimer model [4, 5]. There exists some controversy regarding the sign of the second-neighbor interaction J_2 . While one group has fit the data for $\text{Na}_2\text{Cu}_2\text{TeO}_6$ using the antiferromagnetic-antiferromagnetic (AF–AF) alternating chain model with $J_2 / J_1 \sim 0.1$ [4], Miura *et al.* [5] have pointed out that distinguishing between the AF–AF and AF–ferromagnetic (AF–F) models is very difficult based only on the criterion of the fit quality. The AF–F model does indeed provide an excellent fit with rather different parameters—for example, $J_1 / J_2 \sim -0.8$ —for both Sb- and Te-based materials. Fits to low-temperature heat capacity data appear to support the AF–F model [5].

In an attempt to resolve this controversy, we have carried out calculations using the tight-binding and more accurate n th-order muffin-tin-orbital (NMTO) downfolding method on both the Te and Sb compounds to determine the relative magnitudes of the relevant exchange constants by providing estimates of the corresponding hopping interactions. This is compared with experimental reinvestigation of magnetic properties which included data up to 600 K.

5.2 Structural comparisons

A brief but detailed comparison of the salient structural details of both $\text{Na}_3\text{Cu}_2\text{SbO}_6$ and $\text{Na}_2\text{Cu}_2\text{TeO}_6$ is presented in Tables 5.2 and 5.3. As the Sb^{5+} (0.74 Å) (Ref. [7]) ion is

Relative interaction magnitudes	Magnetic model
$J_2 \approx J_3 \gg J_1$	2-D honeycomb
$J_1 = J_2 \gg J_3$	1-D chain
$J_1 > J_2 \gg J_3$	1-D alternating chain
$J_1 \gg J_2 \approx J_3$	0-D dimer

Table 5.1: The different possible dimensionalities of the Cu^{2+} spin correlations.

slightly larger than Te^{6+} (0.70 Å) (Ref. [7]), there is an overall increase in cell volume, the b axis length, and the interatomic distances within the ab plane. The distances and angles relevant to the three identified exchange pathways J_1 , J_2 , and J_3 are indicated in Table 5.3.

	$Na_2Cu_2TeO_6$	$Na_3Cu_2SbO_6$
$2 \times Cu-O(1)$ (Å)	1.978	2.000
$2 \times Cu-O(2)$ (Å)	1.999	2.021
$2 \times Cu-O(1)$ (Å)	2.533	2.494

Table 5.2: Some selected interatomic Cu–O distances of $Na_2Cu_2TeO_6$ and $Na_3Cu_2SbO_6$ (Refs. [4] and [6]).

5.3 Results

5.3.1 Tight-binding, magnetic dimer model:

In the tellurate material [4], the extended Hückel, spin dimer analysis [9] was employed. In these computations the intersite hopping energy (Δe) is estimated using the CAESAR package [10]. Assuming that $J \sim (\Delta e)^2/U$ and that U is constant, the relative magnitude of the various J 's can be determined. For the antimonate system we have followed the same procedure and the obtained results are summarized in Table 5.4 in comparison with results for tellurate [4].

	$\text{Na}_2\text{Cu}_2\text{TeO}_6$	$\text{Na}_3\text{Cu}_2\text{SbO}_6$
b (Å)	8.675	8.867
V (Å ³)	269.05	269.81
(Cu–Cu)[J_1] (Å)	5.82	5.91
(\angle Cu–O–O)[J_1](deg)	139	137.2
(Cu–Cu)[J_2] (Å)	2.86	2.96
(\angle Cu–O–Cu)[J_2](deg)	91.3	95.3
(Cu–Cu)[J_3] (Å)	3.21	3.20
(\angle Cu–O–Cu)[J_3](deg)	90.0	89.6

Table 5.3: Some selected structural parameters of $\text{Na}_2\text{Cu}_2\text{TeO}_6$ and $\text{Na}_3\text{Cu}_2\text{SbO}_6$ (Refs. [4] and [6]).

Note that in both cases, J_1 , which involves the longest Cu–Cu pathway, is, nonetheless, the largest interaction by far. Second in magnitude is J_2 , of order ~ 0.1 of J_1 . J_3 is much smaller, ~ 0.01 of J_1 . Comparing the tellurate and antimonate phases the calculated $J_1(\text{Sb})/J_1(\text{Te})$ ratio is 0.54 compared to the experimental ratio of 0.59, which is an acceptable agreement. However, the observed and calculated J_1/J_2 ratios are in poor correspondence.

5.3.2 Local density approximation calculation:

It is of considerable interest to apply a more rigorous computational method to this problem, specially the accurate N MTO-downfolding procedure as established in previous sections.

Self-consistent electronic structure calculations were carried out within the LDA framework of the density functional theory (DFT) in the tight-binding linear muffin-tin-orbital

Pathway	Te $(\Delta e)^2$ (meV) ²	Rel.	Sb $(\Delta e)^2$ (meV) ²	Rel.
J_1	10200	1	5224	1
J_2	3320	0.33	295	0.06
J_3	130	0.01	16	0.003

Table 5.4: $(\Delta e)^2$ for the various exchange pathways in both $\text{Na}_2\text{Cu}_2\text{TeO}_6$ and $\text{Na}_3\text{Cu}_2\text{SbO}_6$ calculated on the spin dimer model.

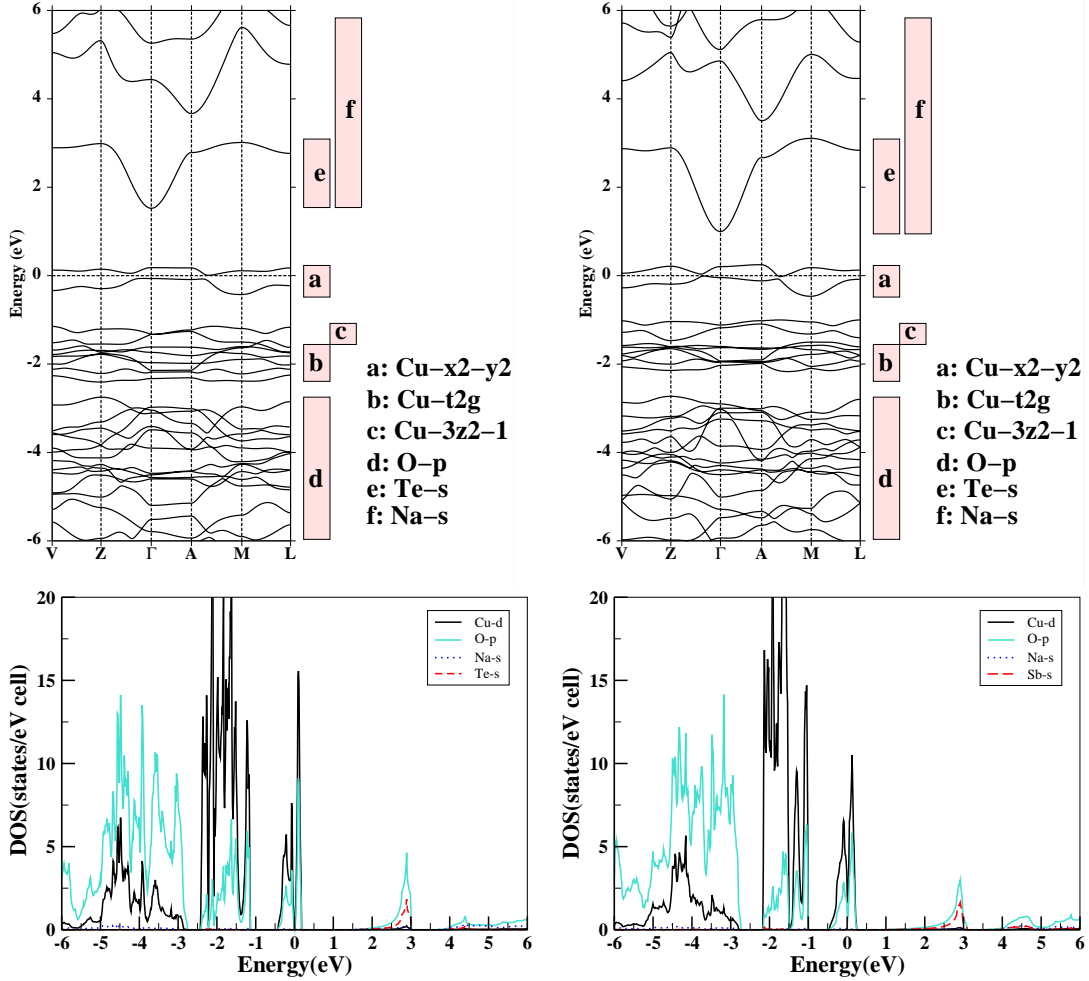


FIGURE 5.3: LDA band structure (top panel) and orbital-projected density of states (bottom panel) of tellurate (left) and antimonate (right). The bands are plotted along the high symmetry points of the monoclinic BZ. The zero-point energy is set at the LDA Fermi energy in both panels. The energy regions with the respective dominant orbital characters are marked in the top panel.

(TB-LMTO) basis. The basis set consisted of Cu spd , Te or Sb sp , O sp , and Na s orbitals. Five (Te) or four (Sb) different classes of empty spheres were used to space fill the system. The band structure and corresponding density of states are shown in Fig. 5.3.

The orbital characters indicated in the figure are obtained by choosing the local coordinate system with the local z axis pointing along the long Cu–O(1) bond and the local y axis pointing along the short Cu–O(1) bond. The distorted octahedral environment of the Cu^{2+} ion sets the energy of the $3d_{x^2-y^2}$ orbital as the highest. Consistent with this picture, there are two bands of $d_{x^2-y^2}$ symmetry (there are two Cu atoms per unit cell) split off from the

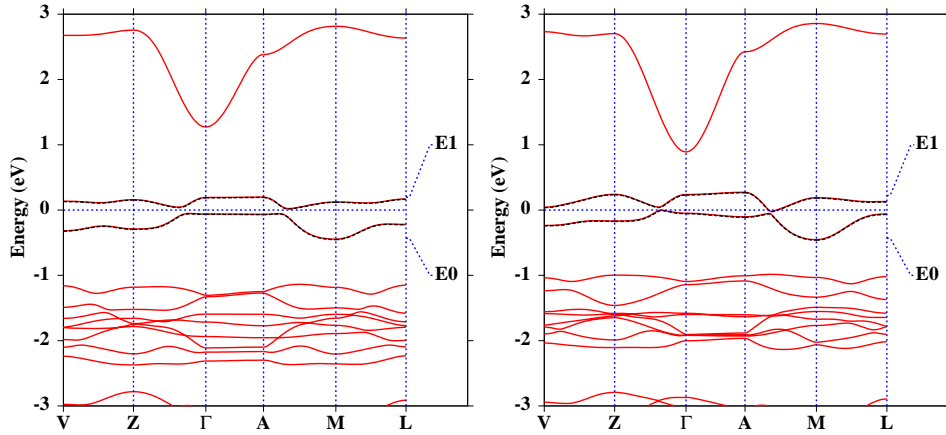


FIGURE 5.4: Bands obtained with massively downfolded Cu $d_{x^2-y^2}$ basis (in thick lines) compared to full LDA band structure (in thin dashed lines) for tellurate (left panel) and antimonate (right panel). The NMTO energy points E_n spanning the region of interest are shown on the right-hand side.

other bands, spanning an energy range from -0.4 eV to 0.2 eV with the zero energy set at the LDA Fermi level. The energy bands dominated by other d characters, such as d_{xy} , d_{xz} , d_{yz} , and d_{z^2} , are located within the energy range -2.4 and -1.2 eV, separated by a gap of ~ 0.8 eV from the $d_{x^2-y^2}$ bands. The O p -dominated bands appear at ~ -6 eV to -3 eV. There is only a negligible contribution from Na states to the bands crossing the Fermi level and a small but non-negligible mixing from Te (Sb) states as is more evident in the plot of effective NMTOs to be presented in Fig. 5.5.

Note that in the low-energy range, the LDA calculation leads to two almost half-filled bands—i.e., to a metallic state. It is well known that the LDA fails to describe the correct insulating ground state for strongly correlated electron systems, as is the case here. The inclusion of the missing correlation beyond the LDA provides the insulating ground state. This was checked by treating the correlation within the LDA+U framework. While the LDA fails to provide the correct ground state for these materials, it describes the chemical bonding aspects correctly and is highly successful in deriving the microscopic model.

The few-band, downfolded Hamiltonian was constructed from the effective Cu $d_{x^2-y^2}$ by integrating out all degrees of freedom associated with Te, Na, and O and the Cu t_{2g} and d_{z^2} states. This choice is driven by the fact that the Cu^{2+} state is described by a half-filled $d_{x^2-y^2}$ orbital. Therefore, these are the bands which appear close to the Fermi level and dominate the low-energy Hamiltonian. The downfolded band structure is shown in Fig. 5.4 (left panel) along with the full LDA result.

With choice of two energy points of expansion, marked as E0 and E1 in the Fig. 5.4,

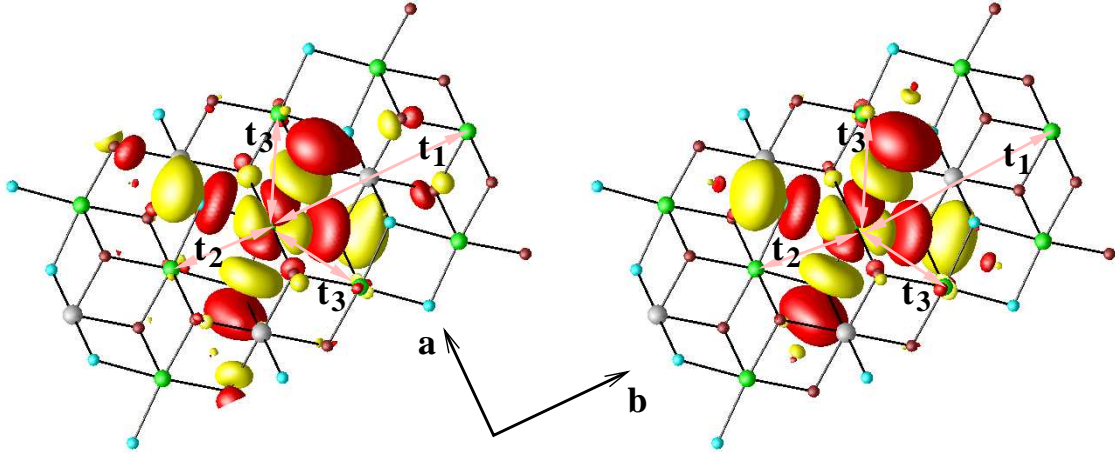


FIGURE 5.5: The effective orbitals corresponding to the downfolded Cu $d_{x^2-y^2}$ calculations viewed for tellurate (left) and antimonate (right). Plotted are orbital shapes (constant-amplitude surfaces) with lobes of opposite signs colored as red and yellow. The $d_{x^2-y^2}$ orbital is defined with the choice of the local coordinate system with the y axis pointing along the short Cu–O(1) bond and the x axis pointing along the Cu–O(2) bond within the square plane. Green and gray atoms stand for Cu and Te(Sb) respectively and brown and cyan atoms represent two inequivalent O.

the downfolded bands are indistinguishable from the full band structure within the region of interest. This indicates excellent convergence of the downfolded $d_{x^2-y^2}$ bands which in the present case form an isolated set of bands. The underlying NMTOs, therefore, are the corresponding Wannier functions which are plotted in Fig. 5.5. The central part has $3d_{x^2-y^2}$ symmetry with the choice of local coordinate system as stated above, while the tails are shaped according to O p symmetry to take into account hybridization effects. Shown are the orbital shapes with two different lobes colored differently. We note the $pd\sigma$ antibonds formed between Cu $d_{x^2-y^2}$ and O p . A careful look at the O p -like tails reveals that one of the lobes is enlarged with respect to the other and bends towards the Te/Sb site which in turn points towards the non-negligible contribution of Te/ Sb, in providing the mediating pathway. This feature is more pronounced for $Na_2Cu_2TeO_6$ than for $Na_3Cu_2SbO_6$, giving rise to a higher value of J_1 in the case of the Te compound compared to that of the Sb compound as discussed in the following.

The real-space representation of the downfolded Hamiltonian, $H_{TB} = \sum_{ij} t_{ij} (\hat{c}_i^\dagger \hat{c}_j + h.c.)$, provides the information of the effective hopping interaction t_{ij} , between the Cu^{2+} ions at sites i and j . Such estimates of the effective hopping integrals are useful in defining the underlying low-energy magnetic model, in the sense that the effective Cu–Cu hopping integral t can be related to the Cu–Cu magnetic exchange coupling interaction J via a second-order perturbative treatment within the framework of a many-body Hubbard-like

Pathway	Te t (meV)	Te t^2 (meV) ²	Rel.	Sb t (meV)	Sb t^2 (meV) ²	Rel.
J_1	139	19321	1	124	15376	1
J_2	14	196	0.01	45	2025	0.13
J_3	38	1444	0.07	31	961	0.06

Table 5.5: Intersite hopping energies calculated from the *NMTO* downfolding model for $\text{Na}_2\text{Cu}_2\text{TeO}_6$ and $\text{Na}_3\text{Cu}_2\text{SbO}_6$.

model. Assuming that these couplings are AF and neglecting the F contributions, J_{AFM} can be estimated as $\sim 4t^2/U$ where U is the effective on-site Coulomb repulsion on the Cu site.

Though such an approach may be quite legitimate for the exchange interaction J_1 with the Cu-O-O angle close to 140° , for interactions like J_2 and J_3 where Cu-O-Cu angles are reduced considerably from 180° , one needs to be more careful. For this purpose, we have carried out total energy calculations with different spin arrangements at various Cu sites. Comparison of the total energies with AF spin alignment between Cu sites connected via J_2 pathways to those for F spin alignment shows the former to be lower in energy, thus proving J_2 to be AF, unequivocally.

In Table 5.5, we present the values of the effective hopping integrals, t_j , for the relevant magnetic exchange pathways. We also include t_j^2 by which the relative strengths of the various magnetic interactions can be obtained as $J \sim t^2/U$. These results can be compared directly with those of Table 5.4 obtained from the TB spin dimer analysis.

Both the TB and *NMTO* downfolding methods find that J_1 is overwhelmingly the strongest exchange pathway for both materials. The predicted $J_1(\text{Sb})/J_1(\text{Te}) \sim 0.8$ is a bit larger than the observed ratio of ~ 0.6 and, oddly, the TB spin dimer result is closer to experiment. For the Te phase, both J_2 and J_3 are of the order 10^{-2} of J_1 , suggesting that this material is close to a pure Bleaney-Bowers dimer. This is roughly consistent with experiment (the experimental result is ~ 0.1).

The calculations predict a stronger J_2 interaction for the Sb phase, $J_2(\text{Sb})/J_1(\text{Sb}) \sim 0.13$, whereas the experimental result is ~ 0.4 . Nonetheless, this is an improvement over the TB calculation for which $J_2(\text{Sb})/J_1(\text{Sb})$ is found to be ~ 0.06 . As well, *NMTO* predicts that $J_2(\text{Sb})/J_1(\text{Sb}) > J_2(\text{Te})/J_1(\text{Te})$ which is observed experimentally, while the TB method predicts the opposite. Perhaps surprisingly, $J_3(\text{Te}) > J_2(\text{Te})$, but both are very small relative to J_1 . One also needs to remember that these estimates are obtained via a t^2/U kind of relation, which is not strictly valid for the J_2 and J_3 pathways.

5.3.3 Magnetic susceptibility:

As mentioned, Miura *et al.* [5] have studied the magnetic behaviors of both $Na_2Cu_2TeO_6$ and $Na_3Cu_2SbO_6$. They have pointed out, correctly, that it is very difficult to distinguish between the AF–AF and AF–F alternating chain models based solely on the fitting of the low-temperature susceptibility data. Furthermore, it was argued that an analysis of the magnetic component of the specific heat data can be used to discriminate between the two models and these data were interpreted in favor of the AF–F model with J_1 and J_2 of comparable magnitudes, $\alpha \sim -0.8$. This approach is not without difficulty. In particular, the isolation of the magnetic contribution from the total specific heat can be problematic, as a good lattice match material is needed, given that the magnetic contribution to the specific heat extends to rather high temperatures. For this purpose $Na_3Zn_2SbO_6$ was chosen, which is isostructural with $Na_3Cu_2SbO_6$, but of course there is no static Jahn-Teller distortion at the Zn^{2+} site which will influence the phonon spectrum and introduce some uncertainty into the subtraction procedure.

Apart from these potential experimental difficulties, it should be noted that neither computational method predicts a J_2 which is of comparable magnitude to J_1 with either sign for both materials. There also exists a rather simple experimental test which can distinguish between the AF–AF and AF–F linear chain models for these materials. By analysis of the high-temperature susceptibility, the models can be compared to the mean-field result for the Weiss temperature θ_c . In the high-temperature regime $T > 300$ K, the Curie-Weiss law is seen to describe the data very well. The relationship between the Weiss temperature and the various exchange constants J_m is well known and given by [11]

$$\theta = \frac{2S(S+1)}{3k_B} \sum_{m=1}^N z_m J_m, \quad (5.1)$$

where θ is the Weiss constant, z_m is the number of m th nearest neighbors of a given atom, J_m is the exchange interaction between m th neighbors, and N is the number of sets of neighbors for which $J_m \neq 0$. For both systems with $S = \frac{1}{2}$ and $z_1 = z_2 = 1$; i.e., neglecting the J_3 contribution the relationship is simplified to

$$\theta = \frac{J_1 + J_2}{2k_B}. \quad (5.2)$$

In Table 5.6 the observed θ values are compared with those derived from Eq. (5.2) and the J 's obtained from the fits to the low-temperature data with both the AF–AF and AF–F linear chain models.

Clearly, the AF–AF linear chain model is in much better agreement with the observed Weiss temperatures for both materials as predicted by theory. In fact, the value derived from the AF–F model for the antimonate is actually of the opposite sign to that observed.

	Na ₂ Cu ₂ TeO ₆	Na ₂ Cu ₂ TeO ₆	Na ₃ Cu ₂ SbO ₆	Na ₃ Cu ₂ SbO ₆
	AF–AF	AF–F	AF–AF	AF–F
J_1/k (K) ^a	–135	–136	–80	–83
J_2/k (K) ^a	–14	108	–31	105
θ_{calc} (K)	–75	–14	–56	11
θ_{obs} (K)	–87(6)	–87(6)	–55(2)	55(2)

Table 5.6: Comparison of observed and calculated Curie-Weiss θ temperatures for both the AF–AF and AF–F linear chain models for Na₂Cu₂TeO₆ and Na₃Cu₂SbO₆. ^aNote that in Ref. [5] the exchange Hamiltonian is written as $J(S_i \cdot S_j)$ whereas, in Ref. [4] and this work $-2J(S_i \cdot S_j)$ is used. Therefore, the J values quoted in Ref. [5] will be of the opposite sign and of twice the magnitude as those in Ref. [4] and the present work. The values in this table have been converted, accordingly.

5.4 Summary and Conclusions

The magnetic properties of Na₃Cu₂SbO₆ have been investigated and compared to those for the structurally related material Na₂Cu₂TeO₆. Two computational methods, the tight-binding spin dimer model and the n th-order muffin-tin-orbital downfolding method, have been used to calculate the intersite hopping energies of the various exchange pathways. We also used total energy calculations of different spin configurations to define the sign. Both methods find that the dominant exchange J_1 is through a Cu–O–Te(Sb)–O–Cu linear pathway and is strongly AF. As well, J_2 is found to be AF. J_2/J_1 is $\sim 10^{-2}$ for the Te phase but ~ 0.15 for the Sb material. These results are compared with each other and with the experiment, and the differences are discussed. A controversy concerning whether the AF–AF or AF–F alternating chain model is appropriate for these materials is addressed both by computation and by experiment, specifically through measurement of the high-temperature, $T > 300$ K, susceptibility and comparison of observed and calculated Weiss temperatures. On the basis of both analyses it can be concluded that the AF–AF alternating chain is the appropriate model for both compounds.

References

- [1] J. E. Greedan, N. P. Raju and I. J. Davidson, *J. Solid State Chem.* **28**, 209 (1997).
- [2] A. S. Wills, N. P. Raju, C. Morin and J. E. Greedan, *Chem. Mater.* **11**, 1936 (1999).
- [3] M. Bieringer, J. E. Greedan and G. Luke, *Phys. Rev. B* **62**, 6521 (2000).
- [4] J. Xu, A. Assoud, N. Soheinia, S. Derakhshan, H. L. Cuthbert, J. E. Greedan, M. H. Whangbo and H. Kleinke, *Inorg. Chem.* **44**, 5042 (2005).
- [5] Y. Miura, R. Hirai, Y. Kobayashi and M. Sato, *J. Phys. Soc. Jpn.* **75**, 847071 (2006).
- [6] O. A. Smirnova, *J. Solid State Chem.* **178**, 1165 (2005).
- [7] R. D. Shannon, *Acta Crystallogr., Sect. A: Cryst. Phys., Diffr., Theor. Gen. Crystallogr.* **32**, 751 (1976).
- [8] J. W. Hall, W. E. Marsh, R. R. Weller and W. E. Hatfield, *Inorg. Chem.* **20**, 1033 (1981).
- [9] M. H. Whangbo, H. J. Koo and D. J. Dai, *J. Solid State Chem.* **176**, 417 (2003).
- [10] J. Ren, W. Liang and M. H. Whangbo, *Crystal and Electronic Structure Analysis Using CAESAR*, PrimeColor Software, Inc., Raleigh, NC, USA, (1998).
- [11] J. S. Smart, *Effective Field Theory of Magnetism*, Philadelphia and London (Saunders, Philadelphia) (1966).

6 *Cu*-based metalorganic systems: an *ab initio* study of the electronic structure*

6.1 Introduction

Metalorganic compounds formed by transition metal centers bridged with organic ligands are being intensively discussed in the context of new molecule-based magnets and electronic materials [1, 2]. The study of these compounds has been increasing over the last decade due to their potential application for data storage, optical switches or magnetic detectors, to give a few examples. In the design of new metalorganic materials and in order to achieve optimally functioning systems, it is of advantage to use ideas that have long been exploited heavily in the fine tuning of the properties of inorganic crystals. Charge and spin densities are routinely being adjusted in semiconductors and high- T_c superconductors by doping or by substituting the transition metals with neighbors in the periodic table. The interest in metalorganic materials is partly due to their modular nature. The modular setup has the advantage of allowing the modification of relevant subunits chemically without changing the subsequent crystal engineering. Substitution of organic groups and ligands in these systems play the role of doping in the search for materials with desired magnetic interaction strengths and charge carrier concentrations.

In the present work we pursue these ideas from a theoretical point of view. We consider a computationally feasible combination of classical with quantum mechanical *ab initio* tools [3] in order to design and analyze new metalorganic compounds. As an example, we introduce systematic changes on existing metalorganic materials in order to achieve desirable electronic or magnetic properties in the modified new structures. Such study i) allows for a gradual understanding of the properties of these low-dimensional systems ii) provides a guide to systematic synthesis in the laboratory.

*This work has been published in *New Journal of Physics* **9**, 26 (2007)

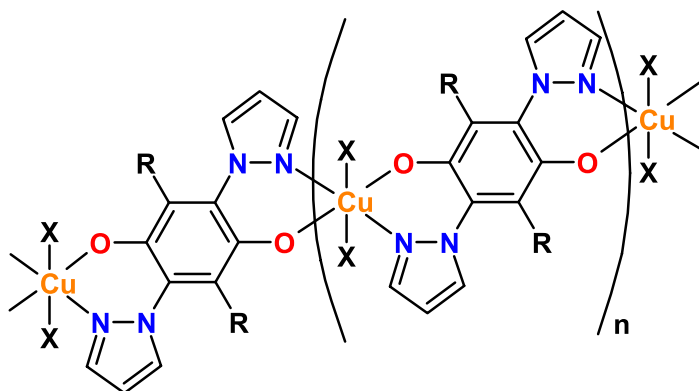


FIGURE 6.1: Polymeric unit of Cu(II)-2,5-bis(pyrazol-1-yl)-1,4-dihydroxybenzene (CuCCP) ($X=\emptyset$, $R=H$). We will consider the substitutions $R=CN$ and $R=NH_2$ on the central benzene ring and the ligands $X=H_2O$ and $X=NH_3$.

We focus our attention on the recently synthesized coordination polymer Cu(II)-2,5-bis(pyrazol-1-yl)-1,4-dihydroxybenzene [4] (CuCCP) which, from susceptibility measurements [5], has been identified as a model system for a spin-1/2 Heisenberg chain with an antiferromagnetic exchange coupling constant of $J = 21.5$ K. The polymeric unit is shown in Fig. 6.1. This compound is a good starting point to study effects of coupling strength variation by appropriately introducing modifications in the linkers as well as changes in the Cu coordination. Note that the coupling strength scale for this system is small compared e.g. to inorganic Cu oxides¹ [6], where the couplings are more than one order of magnitude larger. Accordingly, in this work we will be expecting coupling strength variations in the range of one to a few tens of meV in energy.

The Cu–Cu interaction in this compound depends on the electronic nature of the linker. Its properties can be tuned smoothly and predictably by changing the substitution pattern R (see Fig. 6.1) of the central benzene ring (hydroquinone), or by introduction of additional ligands X at the Cu(II) ions. The substitution or introduction of additional ligands is expected to bring changes in the electronic properties of the compound. For example, it can change the magnitude of magnetic interactions between the Cu(II) centers in the spin chain via change in the charge density in the polymeric chain. It may change the effective, inter-chain interactions, the one-dimensional nature of the original compound may thus be modified. It may even change the coordination and valence of the Cu(II) ions, which may induce changes in the transport properties along the one-dimensional chain by moving away from the Mott insulator at a half-filled Cu $3d_{x^2-y^2}$ orbital.

With the above ideas in mind, we first considered two possible H replacements in the

¹see e.g. the case of La_2CuO_4 with J values greater than 1000 K.

Short name	R	X
CuCCP	H	-
Cu(II)-NH ₂	NH ₂	-
Cu(II)-CN	CN	-
Cu(II)-H ₂ O	H	H ₂ O
Cu(II)-NH ₃	H	NH ₃

Table 6.1: Naming convention for the substitutions and ligands on the CuCCP coordination polymer considered in this work.

central benzene ring: an NH₂ group, which acts as electron donating group, and a CN group, which acts as electron withdrawing group (see Fig. 6.1). Furthermore, extensive crystallization trials showed that crystallites of the Cu(II) polymer always contain lattice defects in high concentration. In many compounds, the Cu(II) ions are coordinated by six nitrogen or oxygen atoms instead of four ligands. The Cu(II) polymer is experimentally crystallized in a mixture of water and ammonia solvents, and it is likely that H₂O or NH₃ molecules are built into the crystal lattice. We have, therefore also considered the introduction of additional ligands like H₂O or NH₃ in the Cu(II) ions in our simulation study. In Fig. 6.1 and Table 6.1 we give an account of these modified structures.

6.2 Method

The methods used in this work, can be primarily categorized into two classes. Firstly, a class of methods has been used for the accurate structural determination of both the parent and the modified compounds. Once the structural aspects are decided, their electronic structures are calculated and analyzed with another class of methods. Note that the understanding of a complex system and design of new compounds need a combination of several different methods, each being focused to deal with one specific aspect. In the following, we give a brief description of all the methods that we have employed.

6.2.1 Determination of crystal structure:

In the absence of diffraction data, a method much used to *a priori* predict crystal structures, is the force field technique [7–12]. While such calculations are computationally fast, they rely on a classical ansatz and therefore miss all possible quantum mechanical effects, which are important for the description of the electronic structure. Quantum mechanical methods, on the other side, are computationally much more demanding, and they are, in this context,

typically employed for two tasks: One is the local optimization after global optimization with force field methods. This has been reported for inorganic systems like NaCl or MgF_2 [13, 14] and for simple organic compounds like glycole $\text{C}_2\text{H}_4(\text{OH})_2$ and glycerol $\text{C}_3\text{H}_5(\text{OH})_3$ [15]. Another is for secondary computations like the determination of molecular geometries, electrostatic charges or for the calculation of intramolecular and intermolecular potential curves [16, 17].

In the present work we used an effective way of designing reliable crystal structures which shares the advantages of both methods, namely the fast calculations with classical force field methods and the subsequent accurate quantum mechanical description with *ab initio* methods. We first created the modified structures on the basis of crystallographic databases [18] and the crystal structures were optimized by force field methods. In the second step the structures were relaxed by *ab initio* quantum mechanical molecular dynamics [19] within the density functional theory (DFT) formalism until the forces on the atoms were less than a given threshold to ensure structure stability. Our work differs from the mentioned previous works in the sense that using this approach, we succeeded in treating materials with large unit cells (of the order of 100 atoms) and complicated electronic structure (transition metal complexes) with sufficient accuracy.

All force field optimizations were performed using the program package Cerius2 [20]. We modified the Dreiding 2.21 [21] force field by introducing energy terms for the case of octahedrally coordinated metal ions. For the energy minimizations we used the modified Dreiding force field with Gasteiger [22] charges. All structural models were based on the experimentally determined crystal structure of CuCCP [4]. The crystallographic symmetry of the structure models was maintained in all relaxations. The position of the Cu ion was kept fixed during all force field and quantum mechanical optimizations. The second step of quantum mechanical relaxations were performed by Car Parrinello (CP) *ab initio* molecular dynamics (AIMD) calculations [19] based on the Projector Augmented Wave (PAW) method² [23].

6.2.2 Electronic structure calculations:

We computed the electronic structure of the relaxed structures with LMTO/*NMTO* as well as the Full Potential Linearized Augmented Plane Wave basis (FPLAPW) as implemented in the Wien2k code [24]. Calculations were performed within the Generalized Gradient Approximation (GGA) [25]. For FPLAPW calculations the choice of muffin-tin radii r_{MT} , k mesh and plane-wave cutoffs k_{max} were carefully tested. We considered a k mesh of

²We have performed non-spin polarized DFT calculations—in contrast to spin-polarized ones—for the structure relaxation since the energy associated with magnetism is much smaller than the cohesion energy and therefore, possible changes on the atomic positions due to the magnetic energy can be assumed to be negligible.

($8 \times 6 \times 5$) in the irreducible Brillouin zone and a $Rk_{\max} = 3.8$, which is reasonable for systems that contain hydrogen atoms. The NMTO downfolding calculations, which rely on the self-consistent potentials derived out of LMTO calculations, were carried out with 17 different empty spheres in addition to atomic spheres to space fill.

It is well known that LDA or GGA fails to describe the correct insulating ground state for strongly correlated electron system, as is the case here. Introduction of missing correlation effects in a static mean-field like treatment as is done in the so called LDA+U approach [26, 27], should give rise to the correct insulating state, as is supported by our calculations (not shown here). In the present work we are mainly interested in estimating the effective one-electron hopping interactions which are well described within LDA or GGA. In fact, the use of DFT calculations to understand the chemistry of correlated materials is a well established method [28].

Finally, in order to analyze the computed electronic structure and to extract an effective microscopic Hamiltonian, we derived quantitatively the Cu–Cu hopping integrals within the *NMTO-downfolding* technique³. Such estimates of the effective hopping integrals are useful in defining the underlying low-energy magnetic model. More precisely, the one-electron effective Cu–Cu hopping integral, t can be related to the Cu–Cu magnetic exchange coupling interaction J via a second-order perturbative treatment within the framework a many-body Hubbard-like model. Assuming that these couplings are antiferromagnetic and neglecting ferromagnetic contributions, J can be estimated as $J_{\text{AFM}} \approx 4t^2/U_{\text{eff}}$ where U_{eff} is the effective onsite Coulomb repulsion on the Cu site.

6.3 Results

6.3.1 Crystal structure:

Dinnebier *et al.* [4] reported the synthesis, and crystal structure determination of the CuCCP system obtained by layering a solution of 2,5-bis(pyrazol-1-yl)-1,4-dihydroxybenzene in CH_2Cl_2 with a solution of CuBr_2 in concentrated aqueous ammonia. The system crystallizes in the triclinic space group $P\bar{1}$ with 27 atoms per unit cell. This compound tends to form independent polymeric chains consisting of deprotonated 2,5-bis(pyrazol-1-yl)-1,4-dihydroxybenzene molecules bridged by Cu(II) ions with a $3d^9$ configuration, which corresponds to a local spin 1/2. As shown in Fig. 6.2 the chain axes are oriented along the c axis of the crystal and the copper ions are located at $(1/2, 1/2, 1/2)$, which is a center of symmetry of the space group $P\bar{1}$. The Cu–Cu distance along the approximate a axis is about 5.2 Å while along the other two axes it is close to 8 Å. These Cu(II) ions are

³The calculations were checked for convergence within the two choices of basis sets (FPLAPW, LMTO/NMTO)

Structure	$a(\text{Å})$	$b(\text{Å})$	$c(\text{Å})$	$\alpha(^{\circ})$	$\beta(^{\circ})$	$\gamma(^{\circ})$	$V(\text{Å}^3)$
CuCCP exp	5.172	7.959	8.230	118.221	91.520	100.148	291.47
Cu(II)-H ₂ O	5.234	11.249	8.072	117.611	68.822	127.155	330.43
Cu(II)-NH ₃	5.459	11.597	8.349	118.423	68.840	130.883	350.49

Table 6.2: Lattice parameters for the experimental crystal structure CuCCP and models Cu(II)-H₂O and Cu(II)-NH₃, optimized with force field methods.

coordinated in an almost square planar fashion by two (pyrazolyl) nitrogen atoms and two oxygen atoms of the deprotonated dihydroxybenzene groups.

The crystal structure was determined from X-ray powder diffraction data; consequently the overall structure and the arrangement of the chains are reliable, but the individual atomic positions had an accuracy of only about 0.3 Å. A DFT analysis of the forces [24] between the atoms shows that the experimentally determined CuCCP structure is still very unstable with forces of the order of 100 mRyd per a_B or more for some atoms. We have therefore relaxed the atomic positions keeping the Cu position fixed with the AIMD method described in section 6.2.1.

The Cu(II)-NH₂ polymer and the Cu(II)-CN polymer were generated from the CuCCP polymer, by substituting the two hydrogen atoms of the benzene rings by amino (NH₂) or cyano (CN) groups, respectively (see Fig. 6.1 and Table 6.1). The Cu(II)-H₂O (Cu(II)-NH₃) polymer was constructed from the CuCCP polymer by adding two water molecules (ammonia molecules) as additional ligands to the Cu(II) ion (see Fig. 6.1 and Table 6.1). In the original crystal structure the chains are quite densely stacked. The introduction of the H₂O (or NH₃) molecules would either lead to unrealistically short contacts to the neighboring chains, or to a considerable increase of the distances between the chains, resulting in an unrealistically loosely packed structure. Therefore the crystal structures of the Cu(II)-H₂O and Cu(II)-NH₃ polymers were fully optimized, including an optimization of the lattice parameters. Moreover, in order to achieve a better packing of the Cu(II) polymer chains with a favorable lattice energy, the Cu(II) chains shifted in the optimization process both sideways as well as along the chain direction with respect to each other. The resulting unit cell parameters are shown in Table 6.2.

All the modified structures were relaxed in the second step with the AIMD method until the forces on the atoms were sufficiently small to ensure stability of the quantum mechanical calculations. In the Appendix we present the relaxed structural data of all the modified structures.

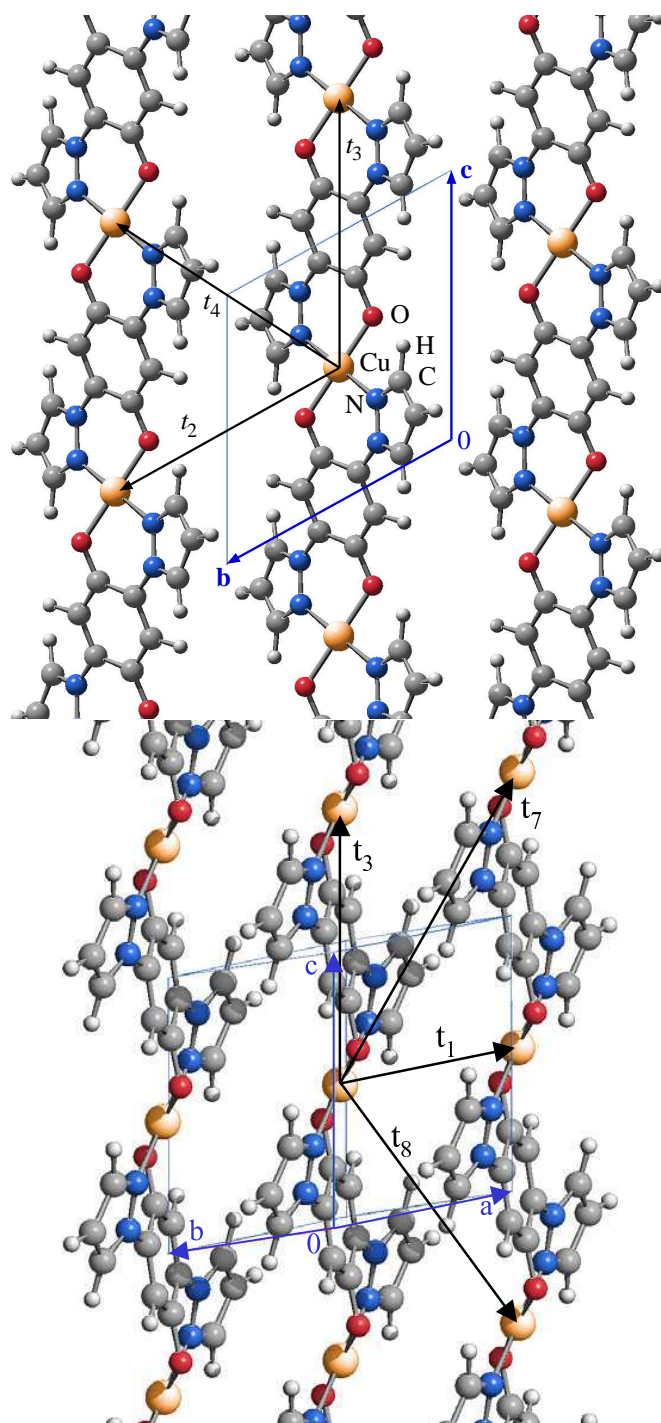


FIGURE 6.2: Crystal structure of the CuCCP polymer in two different orientations. The unit cell is shown in the figures (vectors a , b , and c). Note the arrangements of the Cu chains along the c direction. The various Cu–Cu interaction paths t_i have been also drawn where the index $i=1, 2, 3, 7, 8$ denotes the i -th nearest neighbor.

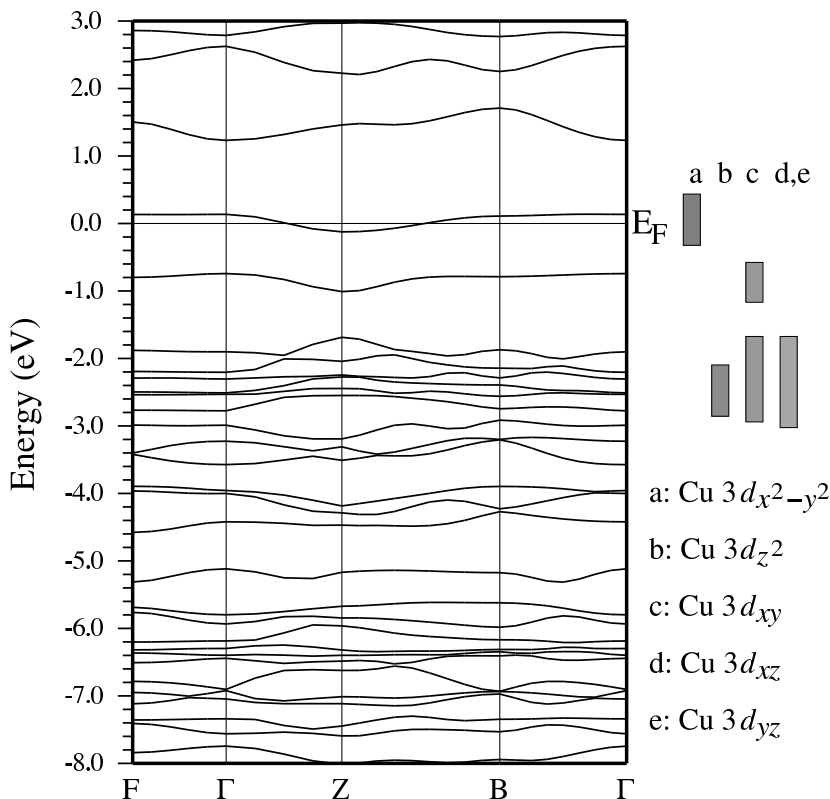


FIGURE 6.3: Band structure for the relaxed Cu(II) polymer CuCCP in the GGA approximation along the path [29] $F(0, 1, 0) - \Gamma(0, 0, 0) - Z(0, 0, 1) - B(0.99, -0.13, 0) - \Gamma(0, 0, 0)$ in units of π/a , π/b , π/c . The bars indicate the dominant band character in the local coordinate frame of Cu (see text for explanation).

6.3.2 Electronic structure and effective Cu–Cu interactions:

(a) CuCCP

In Fig. 6.3 we present the band structure for the relaxed CuCCP where the Cu d band character is shown by bars on the right side. The band characters are given in the local coordinate frame of Cu which is defined with the local z direction pointing from the Cu to out-of-plane N atom in the next layer and the y direction pointing from the Cu to in-plane O atom. Cu is in a $3d^9$ configuration, with all d bands occupied except for the last band which is half-filled. GGA predicts a metallic behavior for this system. As mentioned previously, inclusion of on-site electronic correlation within LDA+U opens a gap between a lower occupied Hubbard band and an upper unoccupied Hubbard band and the system is described as a Mott-Hubbard insulator. Since the O-Cu-N angle in the CuO_2N_2 plane is not exactly 90° , the various Cu d degrees of freedom defined with respect to the local coordinate frame mentioned above show slight admixtures. In particular, the Cu $d_{x^2-y^2}$

Path	CuCCP	Cu(II)-NH ₂	Cu(II)-CN
t_1	4	9	22
t_2	8	3	0
t_3	79	88	68
t_7	5	1	9
t_8	3	8	8
t_{12}	0	0	9

Table 6.3: Values for the Cu–Cu hopping integrals calculated with the *NMTO* downfolding method for the relaxed CuCCP, Cu(II)-NH₂ and Cu(II)-CN structures. The values are given in meV. The subscripts $i=1, 2, 3, 7, 8, 12$ denote the i -th nearest neighbors. See Fig. 6.2. Only the hopping integrals having values larger than or equal to one tenth of a meV have been shown.

dominated band crossing the Fermi level has also small contributions from Cu d_{yz} degrees of freedom which arise from the distorted geometry.

From the dispersion of the Cu d band at the Fermi level, we confirm the one-dimensionality of the structure. The paths $F-\Gamma$ and $B-\Gamma$ which correspond to the inter-chain paths are almost dispersionless and the intrachain $\Gamma-Z-B$ path shows a cosine-like behavior. A quantitative analysis of the various hopping integrals obtained with the downfolding procedure, by keeping only the Cu $d_{x^2-y^2}$ degrees of freedom active and integrating out all the rest within the *NMTO* framework, is given in the first column of Table 6.3. The various interaction paths are as shown in Fig. 6.2. The largest hopping integral t_3 is along the chain (see Fig. 6.2) while all other hoppings are almost an order of magnitude smaller.

(b) *Cu(II)-NH₂ and Cu(II)-CN*

In order to have a quantitative account of the structural changes that the polymer system undergoes under the various substitutions, we define the angle between the vector perpendicular to the CuO₂N₂ plane and the vector perpendicular to the benzene ring as the tilting angle ϑ . The substitution of H by NH₂ groups or CN groups in the benzene rings induces a tilting from $\vartheta = 34.9^\circ$ in CuCCP to $\vartheta = 37.3^\circ$ in Cu(II)-NH₂ and $\vartheta = 36.3^\circ$ in Cu(II)-CN.

In Figs. 6.4 (a) and (b) we present the FPLAPW orbital resolved DOS for the Cu(II)-NH₂ and the Cu(II)-CN within the GGA approximation. Shown is the contribution to the total DOS of Cu, O, N, C and the groups NH₂ and CN. While some changes in the detail shape of the DOS for Cu, O, N and C between Figs. 6.4 (a) and (b) are observed, the most important effect is the different electronic nature of the NH₂ and CN groups. Fig. 6.4 (c) shows the contribution of these groups at the Fermi surface. The CN group bands are deep down into the valence band while the NH₂ group has appreciable contribution near

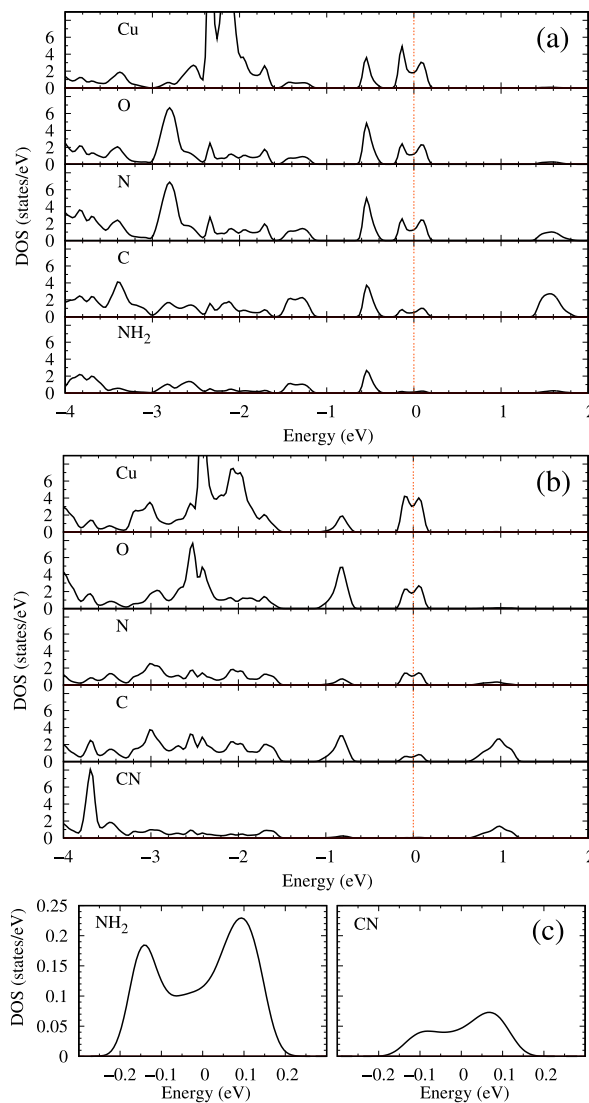


FIGURE 6.4: Orbital resolved DOS for (a) Cu(II)-NH₂ and (b) Cu(II)-CN. Panel (c) shows the comparison of the contribution of the NH₂ and CN groups to the DOS at E_F in a blown up scale.

the Fermi level, which indicates its involvement in the effective interaction paths between copper atoms. We will see this more clearly in the plot of the NMTO-Wannier orbitals to be discussed later in this section.

In Fig. 6.5 we show a comparison of the band structure for the relaxed CuCCP, Cu(II)-NH₂ and the Cu(II)-CN polymers in the energy range $[-0.25 \text{ eV}, 0.25 \text{ eV}]$ where only the Cu $d_{x^2-y^2}$ dominated band is involved. Though the basic nature of the dispersion remains the same upon substitution, the details however do change. NH₂ seems to be the most effective substitution to increase the intrachain Cu-Cu interaction (the bandwidth widens

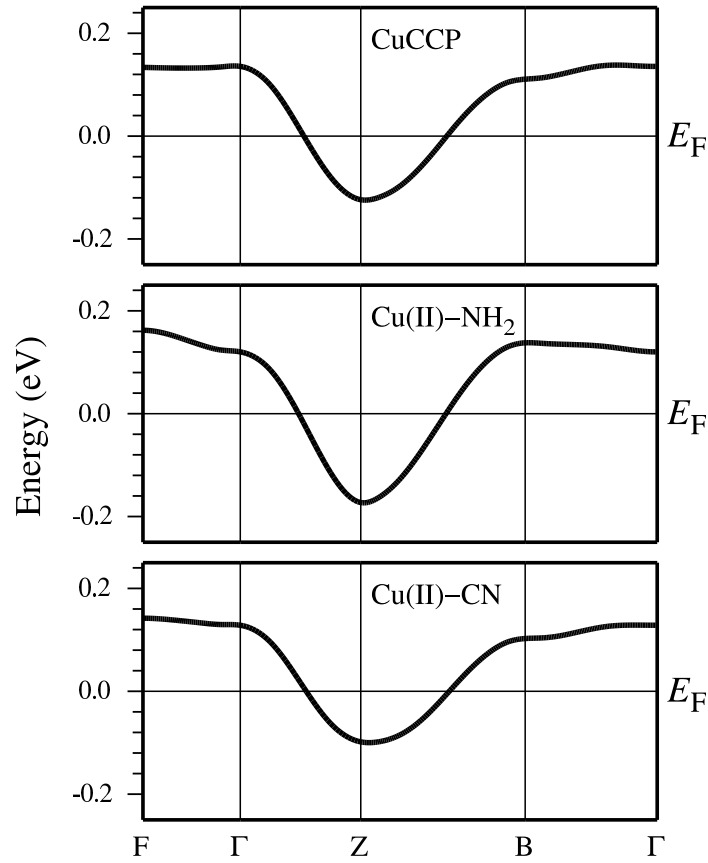


FIGURE 6.5: Comparison between the band structures for (from top to bottom) the relaxed CuCCP, Cu(II)-NH₂ and Cu(II)-CN respectively.

along the Γ -Z-B path for the Cu(II)-NH₂ system). The CN substitution, on the other hand, reduces this interaction (note the bandwidth narrowing along the Γ -Z-B path for the Cu(II)-CN system). The substitution process also enhances certain interchain couplings. The almost dispersionless behavior along F- Γ and B- Γ becomes more dispersive. Description of such fine and subtle changes, need some quantitative measures which can be best described by the changes in effective Cu-Cu hoppings. This is shown in Table 6.3 where the hopping integrals obtained by the NMTO downfolding method are shown. Note that the t_1 hopping for the Cu(II)-CN system along the crystallographic a direction is enhanced by a factor of 4.5. Similarly, t_7 and t_8 hopping terms for the Cu(II)-CN system between neighboring Cu chains in the b direction (see Fig. 6.2) are almost 2-3 times larger compared to that of the CuCCP system. The long-ranged t_{12} hopping parameter between neighboring chains along the a axis also attains appreciable enhancement compared to a vanishing small value for the CuCCP system. Similarly, t_1 and t_8 hoppings are enhanced for the NH₂ substitution by factors of about $\approx 2-3$. Among all the hoppings, only t_2 shows the exception of being

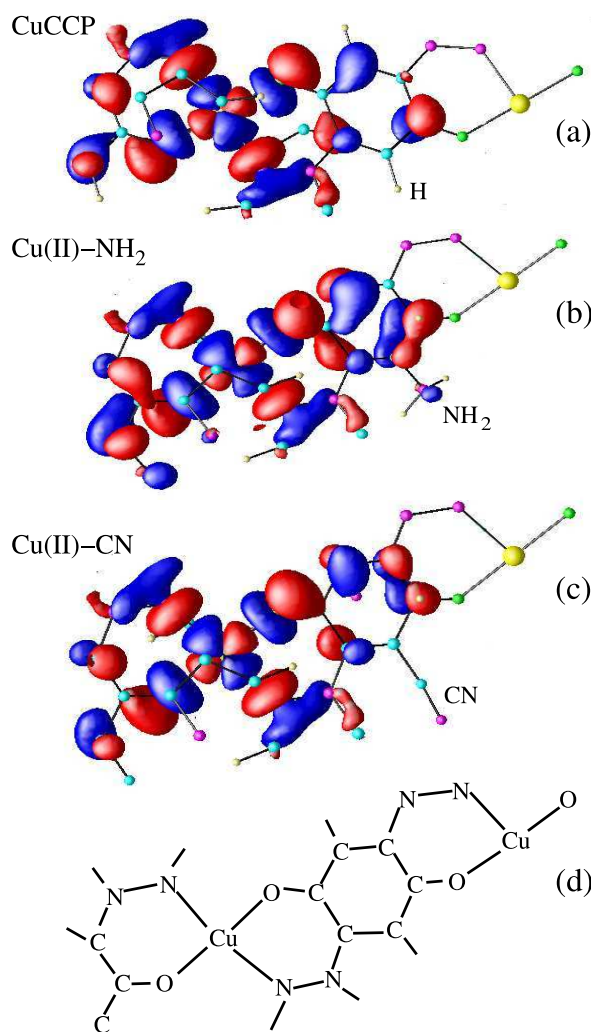


FIGURE 6.6: Cu Wannier functions for (a) the relaxed CuCCP polymer, (b) the Cu(II)-NH₂ polymer, and (c) the Cu(II)-CN polymer. (d) indicates the atom positions common to (a)–(c). The N–C–C–C–H chain of atoms appearing above the Wannier function belongs to the next layer.

systematically decreased upon substitution. The predominant hopping, t_3 is enhanced in the Cu(II)-NH₂ system and reduced in the Cu(II)-CN system as already predicted from bandwidth arguments.

A very helpful tool to understand the origin of these changes is the plot of effective Cu Wannier orbitals. In Fig. 6.6 we show the Wannier orbitals for the three Cu(II) systems presented so far. The plotted Wannier orbitals are obtained with the NMTO downfolding technique.

The effective Cu Wannier orbital has the expected Cu $d_{x^2-y^2}$ symmetry at the central Cu site while the tails sitting at other sites are shaped according to the symmetries of the various integrated out orbitals like the rest of Cu d orbitals, O p , N p or C p . Note

Path	CuCCP	Cu(II)-H ₂ O	Cu(II)-NH ₃
t_1	4	8	11
t_2	8	7	5
t_3	79	57	22
t_7	5	1	1
t_8	3	0	0
t_{12}	0	0	0

Table 6.4: Values for the Cu–Cu hopping integrals calculated with the *NMTO* downfolding method for the relaxed CuCCP, Cu(II)-H₂O and Cu(II)-NH₃ structures. The values are given in meV. The subscripts $i=1, 2, 3, 7, 8, 12$ denote the i -th nearest neighbors. See Fig. 6.2.

that the Cu d , O p and N p antibonding orbitals in the basic CuN₂O₂ square plaquette remain similar in all three cases but the effective orbital distribution in the benzene ring is markedly different. The changes are most prominent for the NH₂ substituted case with the tails attaining appreciable weight at the sites in the benzene ring. We also notice the occurrence of weight at the NH₂ assembly which is in accordance with the orbital resolved DOS study (see Fig. 6.4). This leads to an enhancement in both intra- and some interchain Cu–Cu interactions, caused by the larger overlap of the effective orbitals. The enhancement happens via two different routes: one is due to the different tilting of the benzene ring compared to the original compound and the other one is the opening of additional interaction paths via the NH₂ group which enhances the intrachain as well as interchain interactions t_1 and t_8 as can be seen in the quantitative estimates of the hopping interactions in Table 6.3. In the case of the CN substitution, the opening of an additional intrachain pathway is absent, which is reflected in the reduced intrachain(t_3) hopping interaction. However the mechanism via the tilting of the benzene ring is still operative which is reflected in the enhancement of several interchain couplings, especially t_1 .

Relating the magnetic coupling interaction J with the effective hopping interaction t via a relationship $J_{\text{AFM}} \approx 4t^2/U_{\text{eff}}$, as discussed in Section 6.2.2, and choosing U_{eff} to be 5 eV⁴, we obtain the nearest neighbor coupling for CuCCP system to be $J_{\text{AFM}} \approx 58$ K which is somewhat larger than the experimental estimate [5] obtained by fitting susceptibility data to an effective nearest neighbor Heisenberg model, but remains of the same order of magnitude. The J_{AFM} values estimated for Cu(II)-NH₂ and Cu(II)-CN systems are $J_{\text{AFM}} \approx 72$ K and

⁴Note that this is a very rough U_{eff} estimate since we have here Cu surrounded by two O and two N atoms and the Cu–Cu path is via a complicated organic linker. Typical values of U_{eff} for Cu oxides is 4–6 eV.

≈ 43 K respectively.

(c) *Cu(II)-H₂O* and *Cu(II)-NH₃*

In our second set of modifications we introduce two kinds of ligands, H₂O and NH₃ in the CuCCP system in the way presented in Section 6.3.1. Our goal is to study the effect of H₂O and NH₃ satellites on the CuCCP structure as well as to search for possible routes to change the Cu coordination from planar to octahedral. As explained in Section 6.3.1, in order to obtain realistic structures, the optimization with the force field method was done without keeping the original cell fixed, since that would force very short intermolecular distances between the H₂O (NH₃) moieties and the neighboring chains. The force field optimized structures (see Table 6.2) and subsequently relaxed with AIMD are characterized by Cu–O (O of the H₂O molecule) distances of $d_{\text{CuO}} = 2.17$ Å while the Cu–O and Cu–N in-plane distances are $d_{\text{CuO}} = 1.99$ Å and $d_{\text{CuN}} = 2.01$ Å, respectively. This corresponds to a distorted octahedron elongated along the Cu–H₂O direction. For the case of the NH₃ ligands the Cu–N (N of the NH₃ molecule) distances are $d_{\text{CuN}} = 2.14$ Å, while the Cu–O and Cu–N in-plane distances are $d_{\text{CuO}} = 2.02$ Å and $d_{\text{CuN}} = 2.03$ Å, also giving rise to an elongated octahedron along the Cu–NH₃ direction. The ligands close to the Cu(II) center also induce a tilting of the benzene rings with respect to the CuO₂N₂ plane. From the initial angle of $\vartheta = 34.9^\circ$ in CuCCP the tilting due to the H₂O ligand is quite significant, leading to $\vartheta = 42.9^\circ$ in Cu(II)-H₂O. The NH₃ molecule, by contrast, leads to a lowering of this angle to $\vartheta = 31.8^\circ$ in Cu(II)-NH₃.

In order to quantify the effect of the H₂O and NH₃ ligands on the electronic properties of CuCCP, we show in Table 6.4 the values of the Cu–Cu hopping integrals calculated with the NMTO downfolding method where the hopping parameters for the original CuCCP have been included for comparison. Note that the intrachain Cu–Cu coupling is reduced by a factor of 1.5–3.5 with the inclusion of both ligands. The reduction is especially significant with NH₃. The only Cu–Cu interchain path that is enhanced is t_1 which is between Cu in nearest neighbor chains and has its origin in the hydrogen bonds between the H of the H₂O (NH₃) molecule and the O of the hydroquinone fragments in the chains. Therefore, apart from these hydrogen bonds, the introduction of ligands isolates the Cu ions considerably.

In the Wannier orbital plot in Figs. 6.7 and 6.8, we can see that the distorted octahedral environment of the Cu in the Cu(II)-H₂O and Cu(II)-NH₃ structures induces very little mixing of the Cu d_{z^2} orbital to the predominant $d_{x^2-y^2}$. Also note the little contribution of weight in the hydroquinone ring, in contrast to the previous discussed systems (see Fig. 6.6) which is a manifestation of the isolated nature of Cu in these structures. The inclusion of the H₂O and NH₃ satellites, however, changes the Cu coordination only marginally from four in the direction of six, as opposed to our original motivation for the addition of H₂O and NH₃

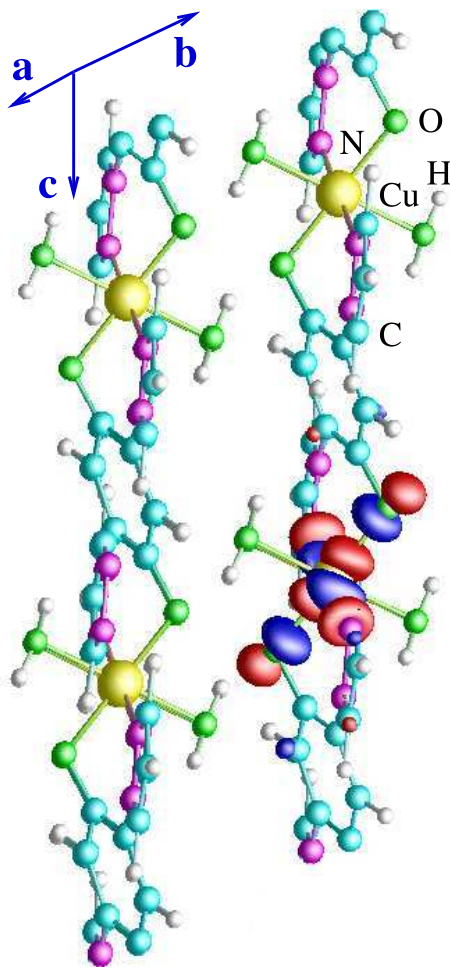


FIGURE 6.7: Cu Wannier functions for the Cu(II)-H₂O system.

ligands. Cu remains in the oxidation state of almost 2+ as observed in our calculations. While the GGA calculations give a metallic behavior with a half-filled predominantly $d_{x^2-y^2}$ Cu band, inclusion of correlation effects with LDA+U drive the system to an insulating state. Therefore the system will remain an insulator.

6.4 Summary

In search of low-dimensional quantum spin systems with tunable properties, we have proposed and analyzed within an *ab initio* framework and using a combination of different computational methods various chemical modifications to the Cu-based polymeric coordination compound CuCCP. Our goal has been to tune in a controlled way the magnetic

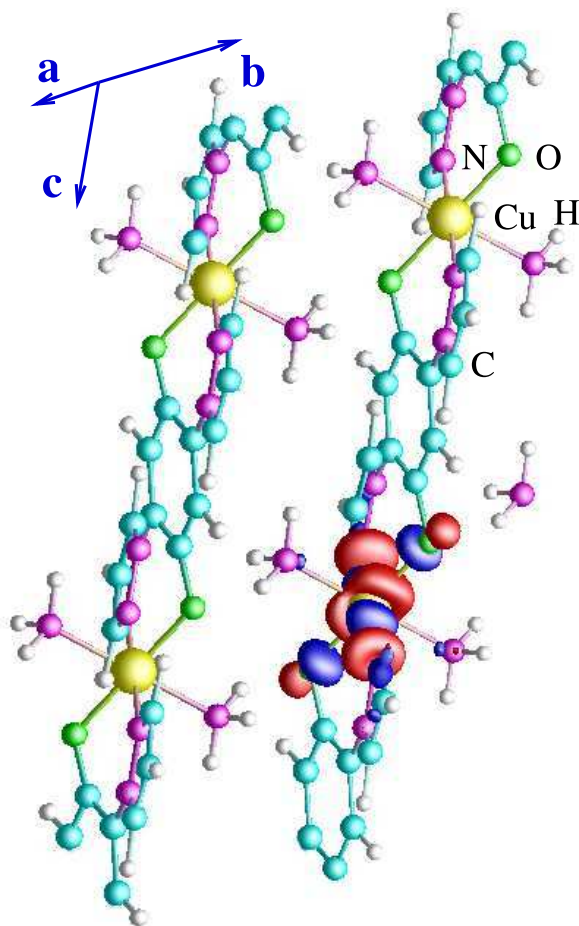


FIGURE 6.8: Cu Wannier functions for the Cu(II)-NH₃ system.

interactions between Cu centers and to test the efficiency and feasibility of the combination of methods proposed here. We pursued two ways of modifying the original CuCCP structure; by changing the substitution pattern in the linker (hydroquinone) and by adding ligands to the system. Following the first scheme we considered two possible H substitutions in the hydroquinone; an electron donating group (NH₂) and an electron withdrawing group (CN). For the second scheme, we considered structures with H₂O and NH₃ ligands. Out of our study we conclude that the NH₂ substitution in the hydroquinone is the most effective in order to enhance the intrachain Cu–Cu interaction in CuCCP while the CN substitution induces and enhances the interchain interactions in the system which were either absent or very weak in the original CuCCP compound. In contrast, the inclusion of H₂O or NH₃ ligands has the effect of isolating the Cu ions.

The effects observed in this study are small, mainly due to the fact that the coupling constants in these metalorganic materials are weak. On the other hand, these systems

are, due to the smallness of the coupling constants, of special interest since application of moderate magnetic fields or pressure can drive the system to a phase transition. These systems can be described as Mott-Hubbard insulators and possibly under application of pressure a metal-insulator transition could be induced. This will form the basis of our future studies.

Finally, we believe that the combination of methods presented in this work is efficient for studying the properties of complex systems *per se*, and that the computer-designing procedure that we have employed in the present study provides a plausible route for manipulating properties related to low-dimensional quantum spin systems in general.

6.5 Appendix

Table 6.5: Fractional atomic coordinates of non-equivalent atoms in the CuCCP relaxed structure. For the lattice parameters, see Table 6.2.

Atom	x	y	z
Cu	0.5000	0.5000	0.5000
O2	0.4581	0.3495	0.6187
C3	0.4745	0.4243	0.7998
C4	0.6696	0.5869	0.9293
C5	0.0331	0.7729	0.6797
C6	0.2206	0.8455	0.8363
C7	0.1024	0.7795	0.9497
C8	0.6971	0.6615	0.1203
N9	0.8576	0.6739	0.8610
N10	0.8109	0.6692	0.6956
H11	0.1732	0.7923	0.0815
H12	0.4193	0.9317	0.8607
H13	0.0456	0.7875	0.5549
H14	0.8471	0.7919	0.2121

We present here the AIMD relaxed structural data of the various Cu(II) polymers. Other than CuCCP, the rest are computer designed.

In Table 6.5 we show the fractional atomic positions of the CuCCP polymer obtained after the relaxation of the system. The resulting distances between the atoms after the optimization are closer to the standard values found in the literature [30] but differs from the values for the distances in the experimental compound [4].

In Table 6.6 we present the relative atomic positions obtained after relaxation for Cu(II)-CN. The cell parameters were fixed during relaxation, and the only change observed was the tilting of the hydroquinone ring as a consequence of the movement upward of the pyrazolyl rings.

In Table 6.7 we show the same, but for Cu(II)-NH₃.

The structural data for the Cu(II)-NH₂ and Cu(II)-H₂O systems were already presented in Ref. [3].

Table 6.6: Fractional atomic positions of non-equivalent atoms in Cu(II)-CN obtained with the PAW method. For the lattice parameters, see Table 6.2 (same as CuCCP).

Atom	x	y	z
Cu	0.5000	0.5000	0.5000
O2	0.4559	0.3460	0.6195
C3	0.4823	0.4252	0.7998
C4	0.6795	0.5881	0.9253
C5	0.0384	0.7593	0.6620
C6	0.2349	0.8314	0.8139
C7	0.1239	0.7694	0.9310
C8	0.6944	0.6601	0.1182
C9	0.1030	0.1811	0.7598
N10	0.8687	0.6739	0.8553
N11	0.8152	0.6676	0.6880
N12	0.9162	0.0575	0.6788
H13	0.2104	0.7793	0.0570
H14	0.4353	0.9135	0.8323
H15	0.0493	0.7681	0.5346

Table 6.7: Fractional atomic positions of non-equivalent atoms in Cu(II)-NH₃ obtained with the PAW method. For the lattice parameters, see Table 6.2.

Atom	x	y	z
Cu	0.5000	0.5000	0.5000
O2	0.4679	0.3798	0.6285
C3	0.4786	0.4444	0.8064
C4	0.6761	0.6148	0.9103
C5	0.0881	0.8540	0.6283
C6	0.2867	0.9709	0.7753
C7	0.1520	0.8949	0.9023
C8	0.6932	0.6630	0.0956
N9	0.8861	0.7410	0.8310
N10	0.8489	0.7159	0.6631
H11	0.2228	0.9402	0.0374
H12	0.4977	0.0958	0.7892
H13	0.0972	0.8601	0.4997
H14	0.8313	0.7917	0.1793
N15	0.8587	0.4701	0.3123
H16	0.7612	0.3507	0.2812
H17	0.0789	0.5407	0.3673
H18	0.9088	0.4872	0.1907

References

- [1] O. Kahn and C. J. Martinez, *Science*, **279**, 44 (1998).
- [2] A. V. Postnikov, J. Kortus and M. R. Pederson, *Psi-k Newsletter* no. **61**, 127 (2004).
- [3] H. O. Jeschke, L. A. Salguero, R. Valentí, C. Buchsbaum, M. U. Schmidt and M. Wagner, *C. R. Chim.* **10**, 82 (2007).
- [4] R. Dinnebier, H. W. Lerner, L. Ding, K. Shankland, W. I. F. David, P. W. Stephens and M. Wagner, *Z. Anorg. Allg. Chem.* **628**, 310 (2002).
- [5] B. Wolf *et al*, *Phys. Rev. B* **69**, 092403 (2004).
- [6] R. R. P. Singh, P. A. Fleury, K. B. Lyons and P. E. Sulewski, *Phys. Rev. Lett.* **62**, 2736 (1989).
- [7] M. U. Schmidt and U. Englert, *J. Chem. Soc. Dalton Trans.* **1996**, 2077 (1996).
- [8] P. Verwer and F. J. J. Leusen, *Rev. Comput. Chem.* **12**, 327 (1998).
- [9] W. T. M. Mooij, B. P. van Eijck, S. L. Price, P. Verwer and J. Kroon, *J. Comput. Chem.* **19**, 459 (1998).
- [10] J. P. M. Lommerse *et al*, *Acta Cryst. B* **56**, 697 (2000).
- [11] W. D. S. Motherwell *et al*, *Acta Cryst. B* **58**, 647 (2002).
- [12] G. M. Day *et al*, *Acta Cryst. B* **61**, 511 (2005).
- [13] J. C. Schön and M. Jansen, *Z. Krist.* **216**, 307 (2001).
- [14] J. C. Schön and M. Jansen, *Z. Krist.* **216**, 361 (2001).
- [15] B. P. van Eijck, W. T. M. Mooij and J. Kroon, *J. Comput. Chem.* **22**, 805 (2001).
- [16] W. T. M. Mooij, F. B. van Duijnefeldt, J. G. C. M. van de Rijdt and B. P. van Eijck, *J. Phys. Chem. A* **103**, 9872 (1999).
- [17] W. T. M. Mooij, B. P. van Eijck and J. Kroon, *J. Phys. Chem. A* **103**, 9883 (1999).

- [18] *Cambridge Structural Database*, (Cambridge, England: Cambridge Crystallographic Data Centre) (2005).
- [19] R. Car and M. Parrinello, *Phys. Rev. Lett.* **55**, 2471 (1985).
- [20] *Cerius2, Version 4.9*, (Cambridge, UK: Accelrys) (2003).
- [21] S. L. Mayo, B. D. Olafson and W. A. III Goddard, *J. Phys. Chem.* **94**, 8897, (1990).
- [22] J. Gasteiger and M. Marsili, *Tetrahedron* **36**, 3219 (1980).
- [23] P. E. Blöchl, *Phys. Rev. B* **50**, 17953 (1994).
- [24] P. Blaha, K. Schwartz, G. K. H. Madsen, D. Kvasnicka and J. Luitz, *WIEN2K, An Augmented Plane Wave + Local Orbitals Program for Calculating Crystal Properties* ed K. Schwarz (Wien, Austria: Techn. University), ISBN 3-9501031-1-2 (2001).
- [25] J. P. Perdew, S. Burke and M. Ernzerhof, *Phys. Rev. Lett.* **77**, 3865 (1996).
- [26] V. I. Anisimov, J. Zaanen and O. K. Andersen, *Phys. Rev. B* **44**, 943 (1991).
- [27] A. G. Petukhov, I. I. Mazin, L. Chioncel and A. I. Lichtenstein, *Phys. Rev. B* **67**, 153106 (2003).
- [28] E. Pavarini, A. Yamasaki, J. Nuss and O. K. Andersen, *New J. Phys.* **7**, 188 (2005).
- [29] C. J. Bradley and A. P. Cracknell, *The Mathematical Theory of Symmetry in Solids: Representation Theory for Point Groups and Space Groups*, (Oxford: Oxford University Press), (1972).
- [30] F. H. Allen, O. Kennard, D. G. Watson, L. Brammer, A. G. Orpen and R. Taylor, *J. Chem. Soc. Perkin Trans. II* **1987** 1 (1987).

7 Microscopic modeling of a spin crossover transition*

7.1 Introduction

An intensively debated class of materials with potential applications as optical switches, sensors or memory devices [1–4], are spin-crossover polymer (SCP) systems involving transition metal ions linked with organic ligands [5]. These systems show a sharp transition triggered by variation of temperature, pressure or by light irradiation between a low-spin (LS) ground state and a high-spin (HS) excited state with a thermal hysteresis loop [6]. Specially important in these materials is the large cooperativity shown at the HS–LS transition in contrast to molecular spin crossover systems. The origin of this transition and its cooperativity has been mainly discussed in the frame of elastic models [6–10], and only recently a possible role of magnetic exchange was suggested [11, 12]. Still, a conclusive *ab initio* microscopic study where all important interactions are considered is missing and the origin of the large cooperativity has not been completely settled. It is our purpose to investigate this issue in what follows. *Ab initio* theoretical studies for SCP systems are faced with major difficulties due to the nonexistence of well-determined crystal structures. To our knowledge, electronic structure calculations have only been performed at the level of semiempirical extended Hückel approximation for an idealized triazole-bridged Fe(II) chain [13]. In the present work, we overcome the unavailability of structural data by predicting a crystallographic structure for a Fe(II) spin-crossover polymeric crystal using known experimental constraints and a combination of classical force field and quantum mechanical molecular dynamical methods. We analyze with Density Functional Theory (DFT) calculations the LS–HS phase transition and show that there exists an interplay between magnetic exchange and elastic properties that is responsible for the large cooperativity in these systems. We also corroborate the quality of our designed structure by comparing with magnetic experiments done on a real sample. Our methodology and results provide a new perspective on the parameters underlying the traditional theoretical approaches.

*This work has been published in *New Journal of Physics* **9**, 448 (2007)

There have been a number of attempts to theoretically account for the features of the HS–LS transition in spin crossover materials. Most of the theoretical work is based on elastic considerations. Two types of elastic models that focus on the faithful reproduction of macroscopic quantities like the HS fraction, are the following: In the first approach, the cooperativity in the HS–LS transition is defined in terms of local distortions which interact with one another elastically causing a long range effective interaction between spin states. This leads to an Ising-type Hamiltonian [14–16] $H = \sum_{i,j} J_{ij} \sigma_i \sigma_j$ which describes the elastic interaction between spin states (LS and HS) in terms of fictitious spin operators ($\sigma = -1$ (1) for LS (HS)) coupled via a nearest neighbor interaction J_{ij} . The coupling constants J_{ij} are parameters of the theory and have not yet been determined from a microscopic model. In an alternative approach, the free energy of spin crossover systems is calculated based on an anisotropic sphere model that describes volume and shape changes of the lattice at the transition [7–9]. One of the few attempts to include magnetic interactions is the recent proposal done in Ref. [12] where the author considers a one-dimensional model for HS–LS systems which contains elastic and magnetic Ising exchange interactions. The ground-state phase diagram is then obtained by the transfer matrix technique for different relative elastic to magnetic coupling strengths.

In the present study we concentrate on the electronic and magnetic degrees of freedom in a spin crossover polymer, and investigate their influence on the microscopic origin of the cooperativity in the HS–LS transition. While it has been assumed in the past that the Fe(II) center nearest neighbor interaction is entirely of phononic origin, our study indicates that a significant part of this interaction arises from magnetic exchange.

7.2 Crystal structure

For this investigation it is indispensable to obtain a reliable crystal structure suitable for DFT analysis. We aim at describing the complex $\text{Fe}[(\text{hyetrz})_3](4\text{-chlorophenylsulfonate})_2 \cdot 3\text{H}_2\text{O}$ [17] (*hyetrz* stands for 4-(2'-hydroxyethyl)-1,2,4-triazole) (see compound **1** in Fig. 7.1), which was synthesized from 2-hydroxyethyltriazole and iron(II)-p-chlorobenzenesulfonate as described in [18].

This compound precipitates as a fine, polymeric powder and single crystals cannot be grown because the polymer is insoluble in water and organic solvents [19]. Melting or sublimation attempts result in decomposition. Hence, X-ray structure analysis is not possible and even the X-ray powder diagram consists of a few broad peaks only which prevent the structure to be determined from X-ray powder data. Other polymeric Fe-triazole compounds have similar properties and no single crystal structure for these systems is known. In the literature only single crystal structures for trimeric Fe compounds (e.g. Ref. [20]),

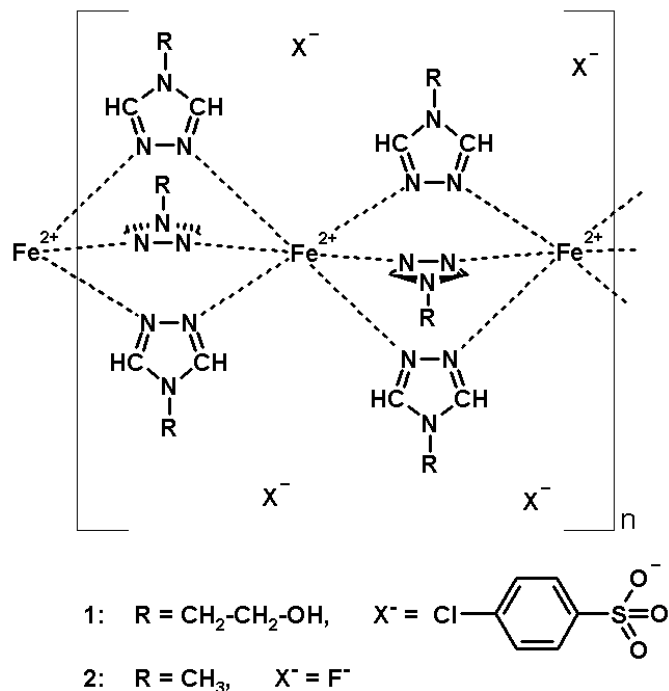


FIGURE 7.1: Chemical diagram of polymeric Fe(II)-triazole. The synthesized compound 1 differs from the model compound 2 in the simplified R and X^- groups.

and polymeric Cu-triazoles [21, 22] were found. In these compounds, the metal ion is coordinated by six nitrogen atoms and neighboring metal ions are connected by three pyrazole bridges. For the polymeric Fe triazoles a similar structure is assumed, see Fig. 7.1. This structure is also supported by spectroscopic methods [22] including solid state NMR.

In view of the above and the requirement of having reliable crystal structures for microscopic studies, we design on the computer a model system of polymeric Fe triazole, as a basis for calculating the electronic and magnetic properties. We consider all experimental information available and construct a crystal structure as close as possible to the actual structure. We employ a method that has been developed and tested on the previous organic polymer Cu(II)-2,5-bis(pyrazole-1-yl)-1,4-dihydroxybenzene which has a simpler structure and less atoms per unit cell than polymeric Fe-triazole [23, 24].

Since we aim at understanding the HS–LS transition with accurate all-electron DFT calculations, which are computer intensive, we keep the essential features of the material and simplify those elements that are secondary to the transition, like the nature of the substituents R and X^- (spin transitions are observed for a wide range of different substituents R and X^-). We consider compound 2 in Fig. 7.1 with $R = \text{CH}_3$ and $X^- = \text{F}^-$.

This model structure has the short range environment of the Fe(II) centers exactly as in structure 1 in Fig. 7.1, while the longer range environment ($\geq 5 \text{ \AA}$) of the Fe^{2+} centers is significantly simplified. The molecular geometry of compound 2 was constructed according to data from single crystal analysis of dimeric and trimeric Fe-triazole compounds [25]. A hypothetical, but sensible crystal structure of compound 2 was built up with the minimum number of atoms per unit cell (72 atoms). The iron-triazole chain itself has $6_3/m2/m2/c$ symmetry. A crystal structure with hexagonal symmetry is in principle possible, e.g. in space group $P 6_3/m$, but we chose a structure with $P 2_1/m$ symmetry with two formula units per unit cell. A similar arrangement of chains is also found in a corresponding Cu polymer, $[\text{Cu}(\text{hyetrz})_3](\text{CF}_3\text{SO}_3)_2 \cdot \text{H}_2\text{O}$ [21]. (This structure is triclinic, with space group $P\bar{1}$ and $Z=2$, but the deviations from monoclinic symmetry are probably caused only by the symmetrybreaking hydroxyethyl ligands and CF_3SO_3^- counterions. Otherwise the symmetry would be $P 2_1/m$.) In our structure, the Fe^{2+} ions are located on crystallographic inversion centers, whereas all triazole units contain a crystallographic mirror plane between the neighboring nitrogen atoms. All Fe^{2+} ions are crystallographically equivalent and we enforce, for simplicity, a perfectly octahedral environment of the Fe^{2+} ions.

In the design and analysis of the model structures we employ four distinct classical and *ab initio* methods. For preoptimization of the model structures we consider a classical modified Dreiding force field with atomic charges calculated by the Gasteiger method as implemented in the Cerius² package. We then perform quantum mechanical first principles calculations within Density Functional Theory (DFT) with three different basis sets, each for a distinct purpose: The plane wave *ab initio* molecular dynamics (AIMD) method is used for determination of precise equilibrium structures. The linearized augmented plane wave (LAPW) method is used to determine accurate electronic and magnetic properties and the linearized / Nth order muffin tin orbital (LMTO/NMTO) methods are used to calculate effective Fe Wannier functions and to understand the low energy excitations of the system.

For the AIMD calculation we considered a plane wave cutoff of 30 Ryd for the plane wave part of the wave function and we used the following sets of (s,p,d) projector functions per angular momentum: Fe(2,2,2), F(2,2,1), N(2,2,1), C(2,2,1) and H(2,0,0). We employed a $(4 \times 4 \times 4)$ k mesh and the $P21/m$ symmetry was preserved during the relaxation with the help of 131 constraints.

For the LAPW calculations, we employed a $(6 \times 6 \times 9)$ k mesh and a value of $R_{MT}K_{max} = 4.2$ that is sufficiently large due to the small radii R_{MT} of the hydrogen atoms.

The NMTO-downfolding calculations, which rely on the self-consistent potentials derived out of LMTO calculations, were carried out with 40 different empty spheres in addition to atomic spheres to space fill. The convergence of LMTO calculations in each case was cross-checked with full potential LAPW calculations.

All DFT calculations were performed within the Generalized Gradient Approximation.

We first proceed with the relaxation of the model structure with the classical force field within the $P 1 1 2_1/m$ space group (non-standard setting of $P 2_1/m$), keeping fixed the Fe–N distances of the FeN_6 octahedra to the values $d_{\text{Fe-N}} \in \{2.00 \text{ \AA}, 2.05 \text{ \AA}, 2.08 \text{ \AA}, 2.09 \text{ \AA}, 2.10 \text{ \AA}, 2.12 \text{ \AA}, 2.15 \text{ \AA}, 2.20 \text{ \AA}\}$. This constraint determines the value of crystal field splitting from the onset and constitutes our control parameter as shown below. As the N–N bond of the triazole (see Fig. 7.1) has a well defined bond length of $d_{\text{N-N}} = 1.38 \text{ \AA}$, the choice of a Fe–N distance leads automatically to lattice parameters linear in $d_{\text{Fe-N}}$. The relative change of the lattice parameter c (the chain direction) is larger than that for a and b . This means that the volume of the unit cell also increases linearly from $V = 6508 \text{ \AA}^3$ at $d_{\text{Fe-N}} = 2.00 \text{ \AA}$ to $V = 7317 \text{ \AA}^3$ at $d_{\text{Fe-N}} = 2.20 \text{ \AA}$. It should be noted that the force field we use is not suitable for relaxing the F^- anion into an equilibrium position due to the lack of appropriate parameters for F^- anions. Therefore, the F^- counterion is put into a likely position and the optimization is left to the next step where we perform a precise relaxation of the structure with the help of *ab initio* molecular dynamics. This AIMD step is essential as we find that the force field relaxed structures still show no or very bad convergence in LAPW, indicating inappropriate positions of at least some atoms. We cross check the final AIMD relaxed structures by calculating the LAPW forces and making sure that they are very small. In Fig. 7.2 a representative of the resulting structures is shown. The top panel shows the chain of FeN_6 octahedra with alternating orientations, and in the bottom panel we demonstrate the arrangement of the Fe(II) chains in the crystal.

7.3 Energy scales

At the atomic level, two sets of energy scales are responsible for the LS and HS state of the Fe(II) centers, namely the crystal-field splitting and the Hund's exchange and coulomb interactions.

The crystal-field splitting, as mentioned above, is being fixed beforehand in the construction of the structures with given $d_{\text{Fe-N}}$ distances. In Fig. 7.3 we show the dependence of the crystal field splitting on the size of the FeN_6 octahedra calculated with LAPW (magenta symbols) and NMTO (green symbols). Note the good agreement between the two calculations. The crystal field splitting values are obtained by determining the first moment of both t_{2g} and e_g densities of states from non-spin polarized LAPW calculations and through construction of an Fe d only Hamiltonian in case of NMTO calculations. The atomic state diagrams for Fe $3d$ schematically demonstrate the relationship between crystal field splitting Δ and the spin state ($S = 0$ or $S = 2$). The Hund's exchange is taken into account to some extent within the spin polarized-GGA approach.

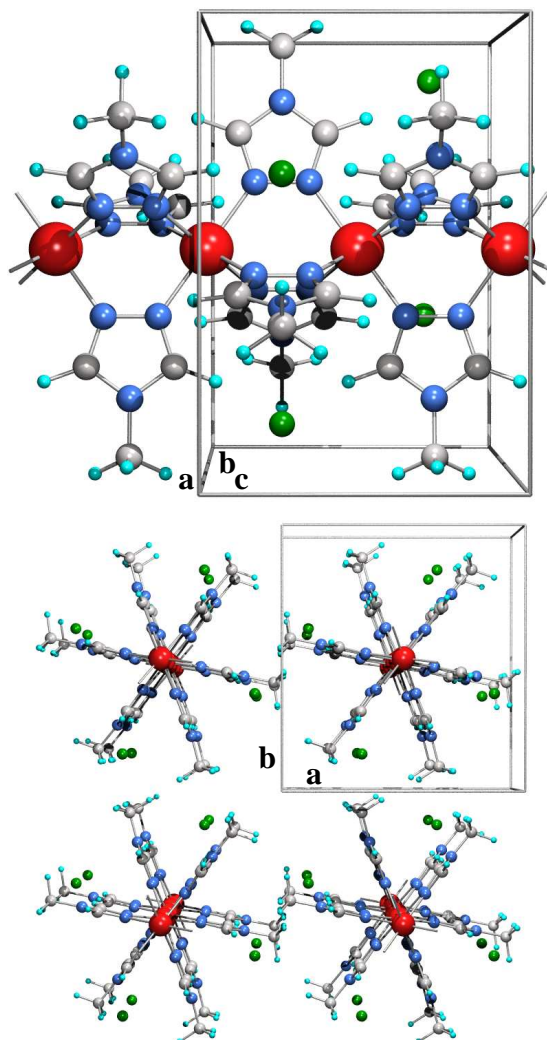


FIGURE 7.2: Simplified Fe(II) triazole structure. Top: Individual chain of octahedrally coordinated Fe^{2+} ions. Note the strong linkage between Fe(II) centers via triple N–N bridges. The orientation of the FeN_6 octahedra is alternating along the chain. Bottom: Arrangement of polymeric Fe(II) chains in the crystal. Red, gray, blue, cyan and green atoms stand for Fe, C, N, H and F respectively.

In the extended system, two type of interactions contribute to the phase transition; the phononic excitations and the exchange interaction J , due to nearest neighbor superexchange between Fe(II) centers which is typically antiferromagnetic.

The competition between all these energy scales determines the nature of the phase transition and its cooperativity. The role played by the phonons in driving the LS–HS transition in the spin-crossover systems has been discussed at length in terms of elastic models [7, 8, 10, 14, 15]. In our model calculations, the phononic degrees of freedom are

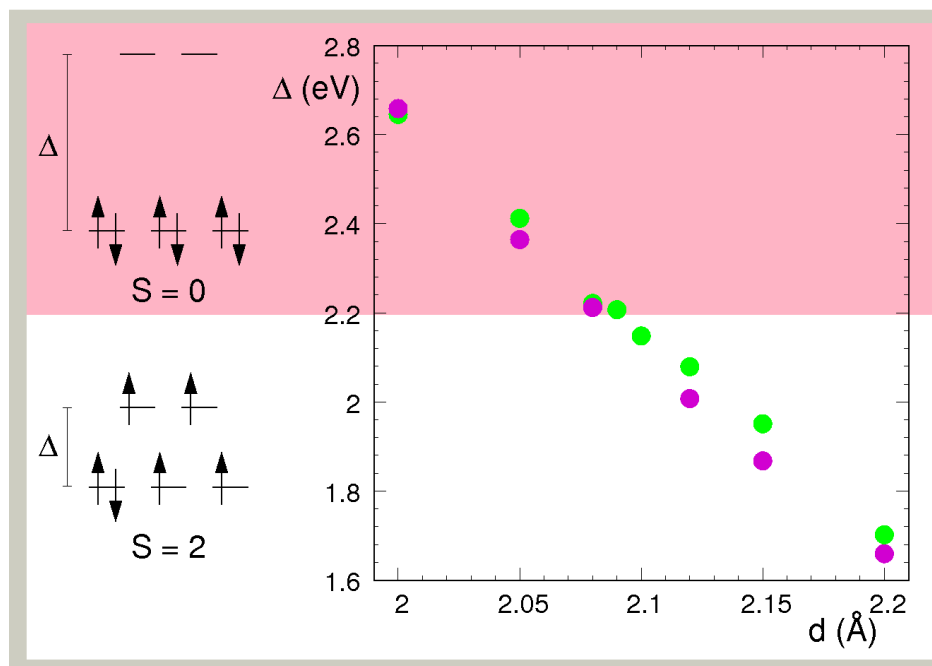


FIGURE 7.3: Crystal field splitting Δ as function of Fe–N distances. The results obtained with LAPW (magenta) and LMTO (green) agree very well. The pink (white) background symbolizes the respective colors of the LS (HS) compounds and indicates the Δ value region that leads to LS (HS). The atomic Fe 3d state diagrams visualize the relationship between crystal field splitting and spin state.

frozen and we investigate the role of the electronic and magnetic degrees of freedom.

7.4 Electronic structure

In Fig. 7.4 we present for four of the designed structures the projection of the total density of states (DOS) on the Fe 3d orbitals, which are responsible for the magnetism of the material. The first and second panels correspond to the structures with $d_{Fe-N} = 2.00$ Å and $d_{Fe-N} = 2.08$ Å respectively and show a perfect symmetry between spin up (red) and spin down (blue) density of states and therefore define a LS state ($S = 0$). The occupied states can be identified as the six t_{2g} states, while the empty states are the four e_g states. The splitting Δ between t_{2g} and e_g states diminishes with increasing d_{Fe-N} from $\Delta = 2.66$ eV to $\Delta = 2.22$ eV, respectively (see also Fig. 7.3). The DOS behavior completely changes as the Fe–N distance increases to $d_{Fe-N} = 2.10$ Å (see the third panel of Fig. 7.4). Now spin up (red) t_{2g} and e_g states are completely filled, and spin down (blue) t_{2g} states show only a partial filling with one electron. The imbalance between up and down electron numbers is $n_{\uparrow} - n_{\downarrow} = 4$ which corresponds to the HS state ($S = 2$). This situation remains

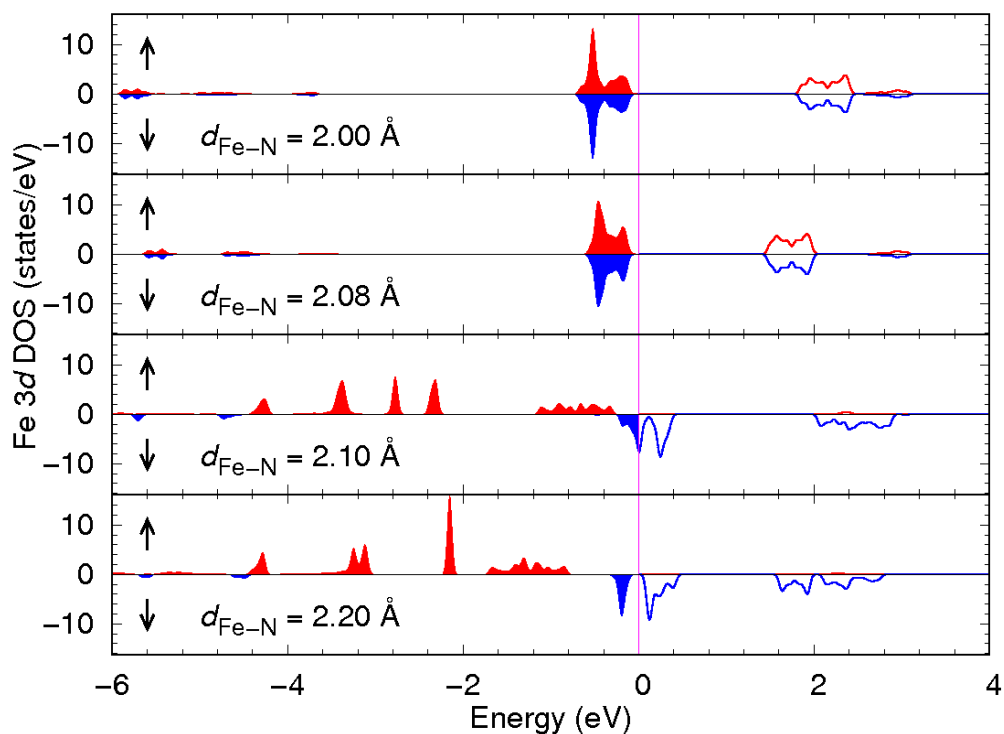


FIGURE 7.4: Spin resolved density of states for selected Fe(II) triazole structures. Red and blue colors denote spin up and down species, respectively. The two upper panels for low Fe–N distances show symmetric density of states corresponding to a low spin ($S = 0$) state. The two lower panels for high Fe–N distances with strong spin up spin down asymmetry correspond to a high spin ($S = 2$) state.

if we further increase the Fe–N distance to $d_{Fe-N} = 2.20 \text{ \AA}$, only the splitting Δ between t_{2g} and e_g diminishes.

Thus, by carefully preparing a series of model structures that correspond to the LS and HS sides of the spin crossover transition we manage to microscopically describe the LS–HS transition which occurs between the structures with $d_{Fe-N} = 2.08 \text{ \AA}$ ($S = 0$) and $d_{Fe-N} = 2.10 \text{ \AA}$ ($S = 2$).

In order to quantify energetically the HS–LS spin transition, we show in Fig. 7.5 the total LAPW electronic energies obtained within the spin-polarized GGA (sp -GGA) approach. We note that there is a discontinuous jump between the LS ($S=0$) energies and the HS ($S=2$) energies. The relative electronic energy differences between the HS and LS systems $\frac{E_{el}^{HS} - E_{el}^{LS}}{E_{el}^{HS}}$ is about 10^{-5} which agrees with the relative energy estimates for spin crossover molecular systems [26]. Since the LS–HS phase transition occurs between structures $d_{Fe-N} = 2.08 \text{ \AA}$ and $d_{Fe-N} = 2.10 \text{ \AA}$, we designed one more structure with $d_{Fe-N} = 2.09 \text{ \AA}$ in order to probe the sharpness of the transition. While there are indications that this

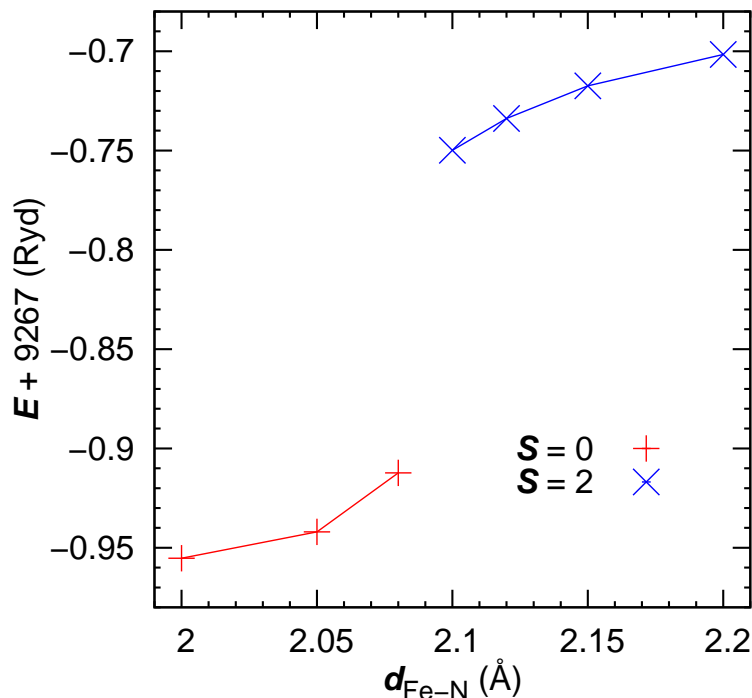


FIGURE 7.5: Groundstate energies for the set of model structures obtained within sp-GGA with the LAPW basis.

structure might represent an intermediate magnetic state with $S \approx 1.5$ per Fe(II) center, we do not include it in Fig. 7.5 as it is very hard to converge. This result indicates that the spin crossover transition in polymer systems occurs in a very narrow range of crystal field splittings, i.e. is very sharp, as observed experimentally [5].

7.5 Exchange interaction and magnetic properties

For the magnetic behavior of this system, we derive first from the DFT electronic calculations a Hamiltonian which describes the effective interaction between Fe(II) centers. The NMTO-based downfolding method, designed to pick up selectively the low-energy bands from the whole group of LDA/GGA bands of a compound, has been used to construct the Fe $3d$ only Hamiltonian of the Fe-triazole compounds. The tight-binding basis in which these Hamiltonians are constructed form the set of “effective” functions, which span the Hilbert space of the Wannier functions corresponding to the low-energy bands. Fig. 7.6 shows the plot of one member of such a set, namely the downfolded Wannier function corresponding to Fe $3d_{xy}$. In the figure, two such Fe $3d_{xy}$ Wannier functions have been placed at two neighboring Fe sites. While the central part of such an effective function

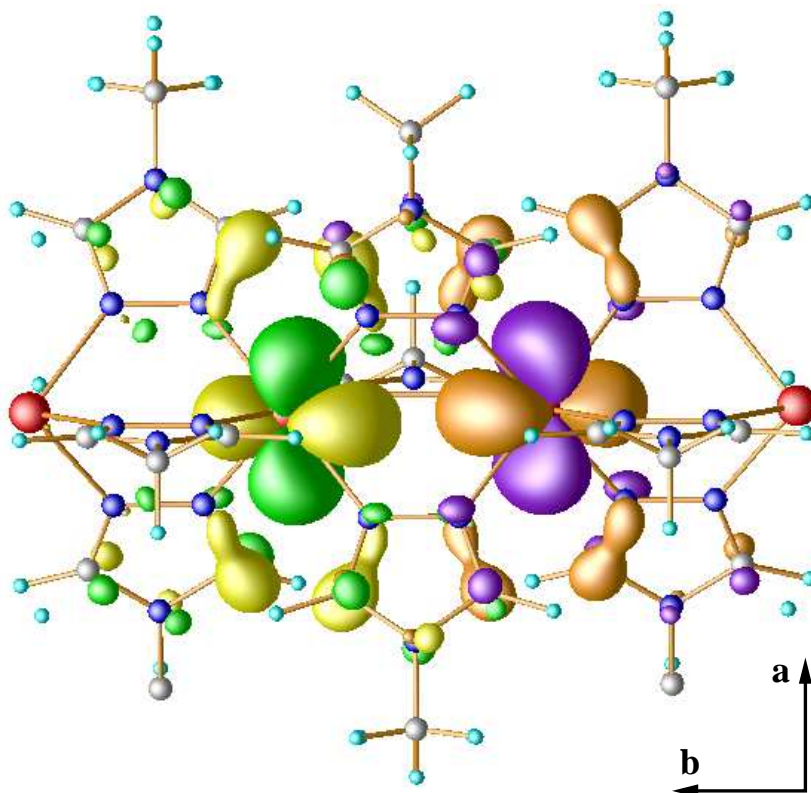


FIGURE 7.6: Wannier functions for the Fe–Fe interactions. The chosen example shows two Wannier functions with $3d_{xy}$ symmetry on two neighboring Fe(II) centers. The effective interaction (superexchange coupling) between Fe(II) centers depends on the degree and relative sign of the overlap of the Wannier function tails on the pyrazole ring. The color scheme of the atoms is the same as in Fig. 7.2

has the Fe $3d_{xy}$ symmetry, the tails of the function are shaped according to integrated out degrees of freedom in the system, like C sp , N sp , F sp and H s . As is evident from the plot, substantial weight of these tails resides on neighboring triazole rings. The presence of these tails hints to an enhanced communication between the adjacent Fe^{2+} ions, contributing to the cooperative nature of the HS–LS transition. Out of these calculations we can estimate the various hopping matrix elements, t , between the d orbitals of adjacent Fe(II) centers. The values of these hopping parameters range between 1 meV to 80 meV quantifying the strength of the interaction paths between neighboring d Fe(II) orbitals.

In order to get estimates of the magnetic superexchange coupling constants J between neighboring Fe(II) centers for the HS Fe-triazole structures, we considered two approaches: i) Perturbation theory [27] where J can be obtained in terms of the hopping parameters t between Fe(II) centers and the onsite Coulomb repulsion U as $J \approx 4t^2/U$. For the HS

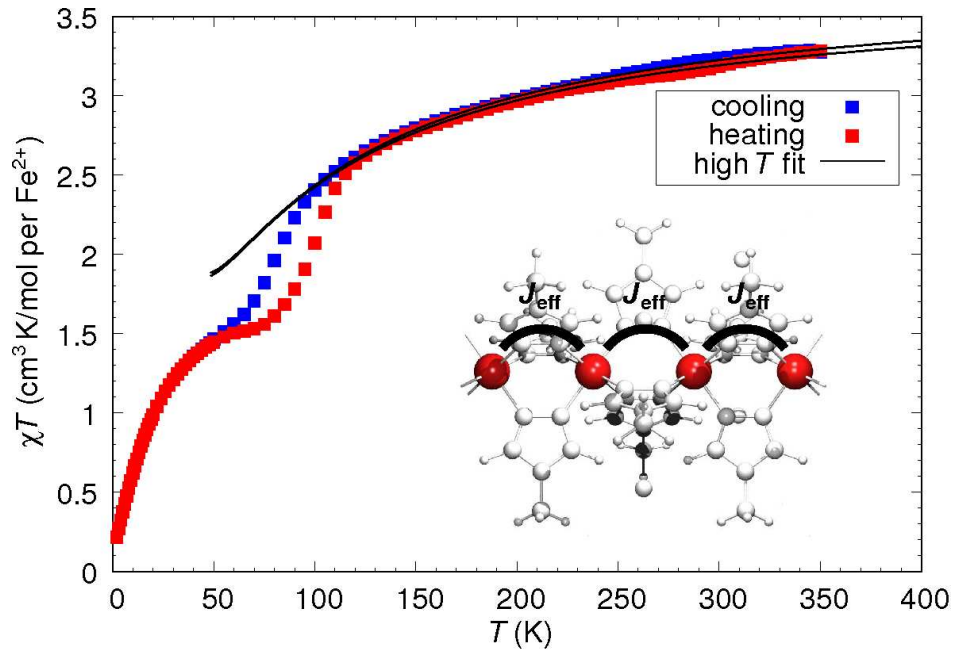


FIGURE 7.7: Measured susceptibility. The solid line corresponds to a high-T fit as explained in the text. The susceptibility measured while lowering (increasing) the temperature shows a hysteresis of 20 K at the transition temperature of 80 K.

$d_{Fe-N} = 2.20 \text{ \AA}$ structure, the significant t obtained within the downfolding method is 48 meV, and for $U = 4-5 \text{ eV}$ this gives $J \approx 22 \text{ K}$. ii) Total energies. We calculated within sp -GGA total energies of ferromagnetic and antiferromagnetic Fe^{2+} spin configurations. Considering a spin-Hamiltonian $H = JS_iS_{i+1}$ between nearest neighbors Fe^{2+} spins S_i , the ferromagnetic and antiferromagnetic energies for two Fe^{2+} ions in the unit cell of the Fe-triazole are given by $E_{FM} = 8J$ and $E_{AFM} = -8J$. Within sp -GGA $E_{FM} - E_{AFM} = 33 \text{ meV}$ for the $d_{Fe-N} = 2.20 \text{ \AA}$ structure and therefore $J \approx 2.1 \text{ meV} = 24 \text{ K}$ which is very similar to the value obtained within perturbation theory.

The results of our model calculations can be now compared with the magnetic properties obtained from the real samples of polymeric $Fe[(\text{hyetrz})_3](4\text{-chlorophenylsulfonate})_2 \cdot 3H_2O$. Variable-temperature magnetic susceptibility measurements in the temperature range 2–350 K and magnetic field 0.02–0.2 T were carried out on powder samples of Fe(II) triazole using a Quantum Design SQUID magnetometer MPMS-XL. In Fig. 7.7 we show the susceptibility χ measurements where χT has been plotted versus T . Our sample shows hysteresis at $T = 80 \text{ K}$ with a width of 20 K. Since this system consists of spin $S=2$ Fe(II) chains with weak interchain interactions, we have analyzed the magnetic susceptibility in the frame of a spin $S=2$ Heisenberg chain model.

Note that the Fe(II) triazole SCP systems are Haldane $S=2$ chains. A Haldane gap

is expected to exist between the groundstate and first excited states. The reason for not observing this gap, is that the transition temperature at which the HS–LS transition happens is higher in energy than the Haldane gap energy and therefore, the system goes into the non-magnetic $S=0$ phase before the gap in the $S=2$ chain can be observed.

The susceptibility of an L -site chain is given by:

$$\chi_L = \frac{g^2 \mu_B^2}{k_B T} \frac{\text{Tr} \left[\left(\sum_{i=1}^L S_i^Z \right)^2 e^{-\beta H} \right]}{\text{Tr} \left[e^{-\beta H} \right]}. \quad (7.1)$$

where H is the Heisenberg Hamiltonian $H = JS_i S_{i+1}$, J is the Heisenberg exchange coupling constant, μ_B is the Bohr magneton, g is the gyromagnetic factor, k_B is the Boltzmann constant, T is temperature and spin S_i^Z is the z -component of the spin on site i . In the thermodynamic limit, the bulk susceptibility at high temperatures can be obtained as a series expansion in $1/T$:

$$\frac{\chi J}{g^2 \mu_B^2} = \frac{1}{3} \left[\frac{S(S+1)J}{k_B T} \right] - 8 \left[\frac{J}{k_B T} \right]^2 + 16 \left[\frac{J}{k_B T} \right]^3 + O \left(\left[\frac{J}{k_B T} \right]^4 \right) \quad (7.2)$$

For $k_B T/J > S(S+1)$ Eq. 7.2 compares very well to QMC data for spin $S = 2$ chains [28].

The fit of Eq. (7.2) to the measured susceptibility of Fig. 7.7 is best for $g = 2.2$ and $J = 11$ K.

The J values obtained from our *ab initio* calculations ($J \approx 24$ K) are slightly larger than the J extracted from the susceptibility data ($J = 11$ K) on the real sample, but remain in the same order of magnitude. Considering that i) we performed the calculations in a model structure and ii) the experimental measurements are affected by the quality of the samples, we can conclude that the comparison is quite good and the designed structures are reliable.

7.6 Discussion

One of the central issues of this work is the analysis of the various energy scales that contribute to the cooperativity of the HS–LS transition in SCP systems. In our calculations we froze the elastic degrees of freedom and concentrated on the electronic and magnetic properties for which we have quantified the corresponding parameters. We have theoretically and experimentally found that the magnetic exchange coupling constants are of the same order of magnitude as the elastic coupling constants J_{ij} that are required in Ising-like models proposed for the spin crossover transition [15]. In such an approach, a material with a transition temperature of $T = 80$ K would be described by elastic interactions of $J_{elastic} \approx 20\text{--}30$ K [15]. This means that in one-dimensional Fe(II) triazole, the elastic

coupling constants $J_{elastic}$ are of equal importance as the magnetic exchange for explaining the spin crossover transition, and the cooperativity should be understood as an interplay between elastic properties and magnetic exchange. When we cool the system from the HS state towards the HS–LS transition temperature, the elastic coupling tends to drive the system to the LS state, while the magnetic exchange tends to keep up the magnetic state for a larger temperature range (see Fig. 7.7). In comparison, in the heating process, the magnetic exchange is initially absent (LS) and therefore the elastic interaction (vibrational phonons) initially drives the transition which has its on-set at a higher temperature than in the cooling process. The width of the transition between cooling and heating (hysteresis) is therefore enhanced by the magnetic interaction.

A fundamental difference between the polymeric systems we are dealing with in this work, and molecular bi- (tri-, tetra-, ...) nuclear Fe systems is the connectivity between the Fe(II) centers. While the molecular systems [29] form isolated clusters of Fe(II) centers and therefore there is no strong connectivity between clusters, the polymers have important nearest neighbor interactions in the thermodynamic limit. This implies that for the polymers, the magnetic superexchange is not restricted to the cluster as in the molecular systems, but rather becomes important for the nature of the HS–LS phase transition. In Ref. [30] various estimates of the magnetic J for molecular systems have been given. The values range between 4–6 K. The values we estimated for the present polymers are larger, between 11–24 K and in the energy range of the elastic constants, which indicates that the cooperativity in these SCP systems is most likely significantly enhanced by the exchange interactions.

In conclusion, this work presents an efficient route to prepare reliable model structures for microscopic investigations and provides a new interpretation about the origin of the parameters underlying traditional theoretical approaches for the polymeric spin-crossover materials.

References

- [1] S. Cobo, G. Molnar, J. A. Real and A. Bousseksou, *Angew. Chem.* **45**, 5786 (2006).
- [2] E. Freysz, S. Montant, S. Létard and J. F. Létard, *Chem. Phys. Lett.* **394**, 318 (2005).
- [3] J. F. Létard, P. Guionneau and L. Goux-Capes, *Top. Curr. Chem.* **235**, 221 (2004).
- [4] Y. Garcia, V. Ksenofontov and P. Gülich, *Hyperfine Interact.* **139-140** 543 (2002).
- [5] O. Kahn and C. J. Martinez, *Science* **279**, 44 (1998).
- [6] P. Gülich, A. Hauser and H. Spiering, *Angew. Chem. Int. Ed. Engl.* **33**, 2024 (1994).
- [7] N. Willenbacher and H. Spiering, *J. Phys. C: Solid State Phys.* **21**, 1423 (1988).
- [8] H. Spiering and N. Willenbacher, *J. Phys.: Condens. Matter* **1**, 10089 (1989).
- [9] H. Spiering, K. Boukheddaden, J. Linares and F. Varret, *Phys. Rev. B* **70**, 184106 (2004).
- [10] M. Nishino, K. Boukheddaden, Y. Konishi and S. Miyashita, *Phys. Rev. Lett.* **98**, 247203 (2007).
- [11] C. Timm and U. Schollwöck, *Phys. Rev. B* **71**, 224414 (2005).
- [12] C. Timm *Phys. Rev. B* **73**, 014423 (2006).
- [13] K. Yoshizawa, H. Miyajima and T. Yamabe, *J. Phys. Chem. B* **101**, 4383 (1997).
- [14] J. Wajnfłasz and R. Pick, *J. Physique IV* **32**, C1 (1971).
- [15] K. Boukheddaden, S. Miyashita and M. Nishino, *Phys. Rev. B* **75**, 094112 (2007).
- [16] K. Boukheddaden, J. Linares, R. Tanasa and C. Chong, *J. Phys.: Condens. Matter* **19**, 106201 (2007).
- [17] Y. Garcia, V. Niel, M. C. Muñoz and J. A. Real, *Top. Curr. Chem.* **233**, 229 (2004).

- [18] Y. Garcia, P. J. van Koningsbruggen, E. Codjovi, R. Lapouyade, O. Kahn and L. Rabardel, *J. Mater. Chem.* **7**, 857 (1997).
- [19] P. Gütlich, P. J. van Koningsbruggen and F. Renz, *Struct. Bond.* **107**, 27 (2004).
- [20] Y. Garcia, P. Guionneau, G. Bravic, D. Chasseau, J. A. K. Howard, O. Kahn, V. Ksenofontov, S. Reiman and P. Gütlich, *Eur. J. Inorg. Chem.*, **2000**, 1531 (2000).
- [21] Y. Garcia, P. J. van Koningsbruggen, G. Bravic, D. Chasseau and O. Kahn, *Eur. J. Inorg. Chem.*, **2003**, 356 (2003).
- [22] Y. Garcia, P. J. van Koningsbruggen, G. Bravic, P. Guionneau, D. Chasseau, G. L. Cascarano, J. Moscovici, K. Lambert, A. Michalowicz and O. Kahn, *Inorg. Chem.* **36**, 6357 (1997).
- [23] H. O. Jeschke, L. A. Salguero, R. Valentí, C. Buchsbaum, M. U. Schmidt and M. Wagner, *C. R. Chim.* **10**, 82 (2007).
- [24] L. A. Salguero, H. O. Jeschke, B. Rahaman, T. Saha-Dasgupta, C. Buchsbaum, M. U. Schmidt and R. Valentí, *New J. Phys.* **9**, 26 (2007).
- [25] *Cambridge Structural Database*, (Cambridge, UK: Cambridge Crystallographic Data Centre) (2005).
- [26] H. Paulsen and A. X. Trautwein, *Top. Curr. Chem.* **235**, 197 (2004).
- [27] P. W. Anderson, *Rev. Mod. Phys.* **50**, 191 (1978).
- [28] S. Yamamoto *Phys. Rev. B* **53**, 3364 (1996).
- [29] A. V. Postnikov, J. Kortus and M. R. Pederson, *Phys. Status Solidi b* **243**, 2533 (2006).
- [30] C. Desroches, G. Pilet, P. A. Szilágyi, G. Molnár, S. A. Borshch, A. Bousseksou, S. Parola and D. Luneau, *Eur. J. Inorg. Chem.* **2006**, 357 (2006).